
Unterschrift Betreuer



TECHNISCHE
UNIVERSITÄT
WIEN
Vienna | Austria

DIPLOMARBEIT

*q*BOUNCE: Systematic analysis of the Ramsey setup

zur Erlangung des akademischen Grades

Diplom-Ingenieur

im Rahmen des Studiums

Technische Physik

ausgeführt am Atominstitut
der Technischen Universität Wien

unter der Anleitung von

Univ. Prof. Dipl.-Phys. Dr. rer. nat. Hartmut Abele
Dipl.-Phys. Dr. rer. nat. Tobias Jenke

durch

Carina Killian B.Sc.

Mariahilfergürtel 14/20
1060 Wien

10. Februar 2020

Unterschrift Studentin

Zusammenfassung

Alle in der Natur vorkommenden Prozesse lassen sich auf vier fundamentale Wechselwirkungen zurückführen: die elektromagnetische, die gravitative, die schwache und die starke Wechselwirkung. Im Rahmen des Standard Modells der Teilchenphysik werden drei der vier fundamentalen Wechselwirkungen erfolgreich als Quantenfeldtheorien beschrieben, einzig die Gravitation entzieht sich der quantenmechanischen Beschreibung. Für dieses fundamentale Problem der Physik gibt es eine Vielzahl theoretischer Lösungsansätze. Deren Überprüfung motiviert experimentelle Tests der Gravitation bei kleinen Abständen, was aufgrund von der, im Vergleich zu den anderen drei Grundkräften sehr geringen Kopplungsstärke der Gravitation, eine große Herausforderung darstellt.

Das q BOUNCE-Experiment realisiert eine solche Überprüfung mit der Vermessung von gravitativ gebundenen Quantenzuständen von *ultrakalten Neutronen* (UCNs). Diese eignen sich, aufgrund von ihrer elektrischen Neutralität und ihrer geringen elektrischen Polarisierbarkeit, hervorragend als Testmassen für Gravitationsexperimente. UCNs haben eine so geringe kinetische Energie, dass sie von Oberflächen unter jedem Einfallswinkel total reflektiert werden. Daher bilden UCNs über einer horizontalen Oberfläche im Gravitationsfeld der Erde gebundene Zustände die quantenmechanischer Natur sind. Die assoziierten Eigenenergien sind nicht äquidistant und können daher mit spektroskopischen Methoden gemessen werden.

Um ausreichend Statistik zu sammeln, ist q BOUNCE aktuell an der UCN-Quelle mit dem weltweit stärksten Fluss, dem Instrument PF2 des Instituts Laue-Langevin (ILL), stationiert. Derzeit erweitert q BOUNCE den Versuchsaufbau auf Ramsey-Spektroskopie um die gravitativ gebundenen Zustände mit erhöhter Messgenauigkeit zu untersuchen. Ein solcher Versuchsaufbau ist sehr komplex, daher werden momentan viele Bereiche optimiert.

Im Rahmen dieser Diplomarbeit wurde das Ramsey-Spektrometer von der q BOUNCE-Kollaboration vor Ort in Betrieb genommen. Diese Arbeit fasst wichtige theoretische Aspekte zusammen und fokussiert auf die Optimierung des Experiments hinsichtlich der Einstellung des Geschwindigkeitsspektrums. Zur Bestimmung des Geschwindigkeitsspektrums wurden drei unterschiedliche Messungen durchgeführt. Die Beschreibung, Auswertung und Analyse dieser Messungen bilden den Hauptteil dieser Arbeit.

Die resultierende mittlere UCN Geschwindigkeit ist etwas größer als die Geschwindigkeit auf die das Setup optimiert ist. Eine entsprechende Adaption könnte die Messgenauigkeit weiter erhöhen.

Abstract

All processes that occur in nature can be explained by four fundamental interactions: the electromagnetic, the gravitational, the weak and the strong interaction. Within the Standard Model of particle physics, three of the four fundamental interactions are successfully described as quantum field theories. Only gravitation eludes quantum mechanical description. There are many theoretical approaches to solve this fundamental problem of physics. Their verification motivates experimental tests of gravity at small distances, which is a great challenge, since gravity is very weak compared to the other three fundamental forces.

The *q*BOUNCE experiment realizes such tests with the measurement of gravitationally bound quantum states of *ultra cold neutrons* (UCNs). Due to their electrical neutrality and their low electrical polarizability, neutrons are excellent test masses for gravitational experiments. UCNs have such a low kinetic energy that they are totally reflected from surfaces at any angle of incidence. Therefore, UCNs form bound states above a horizontal surface in the gravitational field of the Earth, which are of quantum mechanical nature. The associated eigenenergies are not equidistant and can therefore be measured by spectroscopic methods.

To collect sufficient statistics, *q*BOUNCE is currently stationed at the UCN source with the world's strongest flux, the instrument PF2 of the Institut Laue-Langevin (ILL). At present *q*BOUNCE implements a Ramsey-like setup to investigate the gravitationally bound states with increased measurement accuracy. Such a setup is very complex, therefore many areas are currently being optimized.

In the frame of this diploma thesis the Ramsey spectrometer was implemented on site by the *q*BOUNCE- collaboration. This thesis summarizes important theoretical aspects and focuses on the optimization of the experiment regarding the adjustment of the velocity spectrum. Three different measurements were performed to determine the velocity spectrum. The description, evaluation and analysis of these measurements form the main part of this thesis.

The resulting mean UCN velocity is slightly higher than the velocity the setup is optimized for. A corresponding adaptation could further increase the measurement accuracy.

Contents

1	Introduction	1
2	Setup	5
2.1	UCN beam site	5
2.2	The q BOUNCE Ramsey setup	7
3	Theory	10
3.1	UCNs in the gravity potential	10
3.1.1	Eigenenergies	10
3.1.2	Oscillating boundary conditions	12
3.1.3	Two level system	14
3.2	Resonance Spectroscopy	15
3.2.1	The Rabi method	15
3.2.2	Ramsey's method of separated oscillating fields	20
4	Properties of the incoming UCNs	25
4.1	Velocity spectrum	25
4.1.1	Time of flight measurement	25
4.1.2	Aperture measurements	27
4.1.3	Comparison of the two spectra	29
4.2	Monitor detector	29
5	Pressure dependency of the neutron count rate	32
5.1	The effects of pressure on the count rate	32
5.1.1	Experimental setup	32
5.1.2	Neutron count rate	33
5.1.3	Pressure	37
5.1.4	Rate over pressure	40
5.2	Interpretation of the measurements	42
5.2.1	The mean velocity of UCNs	43
5.2.2	The cross section of air for UCNs	50
6	Conclusio	54
A	Calculation steps	56
A.1	56
A.2	57

B Fits	60
B.1 Fit of the near-maximum TOF datapoints to a normaldistribution	60
B.2 Fit of the aperture-spectrum to a normaldistribution	61
B.3 Fit results $R(p)$	61
B.4 Fit results \bar{v}	62
B.5 Fit results Σ	63
C Further elaborations	64
C.1 Time offset	64

Chapter 1

Introduction

The *Standard Model* of particle physics summarizes the essential findings of particle physics in the last century. The discovery of the Higgs boson in 2012, which was predicted 1964 by Peter Higgs et al. [1], was undoubtedly a great triumph for the Standard Model.

The Standard Model is a *quantum field theory*. It describes all known elementary particles and three of the four fundamental interactions: the electromagnetic, the weak and the strong interaction. The only exception is gravity.

Gravity is very weak compared to the other three fundamental interactions: the coupling constants differ by $\approx 34 - 36$ orders of magnitude. However, since it is exclusively attractive and has infinite range, it dominates over large distances and is responsible for the structure of the universe.

As an omnipresent force, gravity was a subject of research very early on. 1687 Isaac Newton was the first to formulate its description mathematically:

$$\vec{F}_G = G \frac{m_i \cdot m_j}{r^2} \hat{r} \quad (1.1)$$

where \vec{F}_G is the gravitational force, G is the gravitational constant, r is the distance between two bodies with masses m_i and m_j and \hat{r} is the unit vector pointing from one mass to the other.

Newton's law of universal gravitation was, for over two centuries, regarded as the complete formulation of gravity. In 1915, Albert Einstein revolutionized the understanding of gravity with his *General Theory of Relativity* (GR): it was no longer understood as a force but as a geometric property of spacetime. The GR describes gravity on large scales very precisely and its predictions, for example the existence of black holes, apply.

It has not yet been possible to quantize the GR and integrate it into the Standard Model.

Neither the Standard Model nor the GR are complete theories. Although the Standard Model is very successful, some pieces of the puzzle are still missing. For example the explanation of the baryon asymmetry, the accelerated expansion of the universe or the rotation curves of galaxies. A major task of modern physics is the unification of all four fundamental forces into one Grand Unified Theory. The incompatibility of gravity and quantum mechanics makes gravity to the subject of many experiments in current research.

Especially tests of gravity on small scales ($\approx \mu\text{m}$) are very interesting. At this scale, gravity, which is otherwise so present, escapes observation with the naked eye and therefore everyday perception. Gravity on μm scales has been tested very little so far and permits predictions that

are strongly related to the open questions of modern physics.

A close examination of gravity on the μm scale looks for deviations from Newton's law of gravity. In general, a *fifth force* acting on small scales in addition to gravity is represented by a Yukawa term in the newtonian potential $V_{\text{Newton}}(r) := -G \frac{m_i \cdot m_j}{r}$:

$$V(r) = -G \frac{m_i \cdot m_j}{r} \left(1 + \alpha e^{-\frac{\lambda}{r}}\right) = -G(r) \frac{m_i \cdot m_j}{r} \quad (1.2)$$

where α is the strength of the non-newtonian interaction and λ is its range. The Yukawa term produces an effective gravitational constant $G(r)$ that depends on the distance r .

To measure the variation of $G(r)$, different scales must be considered [2]. The measurement of $G(r \ll \lambda)$ is part of current research. So far, the best limits for $\lambda \in [1, 10] \mu\text{m}$ were set by [3].

A deviation from Newton's law of gravity is also sensitive to various dark energy and dark matter candidates. Some examples, which have been tested by gravitational experiments, are given in the following paragraphs.

The accelerated expansion of the universe can be explained by light scalar fields - often referred to as *dark energy*. Such scalar fields must be subject to a screening mechanism in order to prevent detection in all past experiments and observations [4].

Chameleon fields are one theoretical candidate for dark energy [5]. The idea is that the combination of the potential of a scalar field and a coupling to matter leads to the existence of an effective potential, which depends on the local mass density of the environment. In high-density environments, such as on Earth, the mass of the field can be large enough to not contradict previous observations and set limits. On cosmological scales, where the density of matter is 10^{30} times smaller, the mass of the field can be in the order of H_0 , the present Hubble parameter [5]. The chameleon-matter interaction was directly tested in [6] and [7]. The chameleon field was excluded for extensive regions in parameter space.

Another dark energy candidate, the *symmetron*, has been proposed by [8] in 2010. Like the chameleon, its coupling to matter depends on the local density of the environment. But in contrast to the chameleon field, the coupling becomes stronger with decreasing density and vice versa. The screening mechanism is based on spontaneous symmetry breaking. In regions of high matter density, the field is drawn towards 0. Its coupling to matter vanishes and the symmetry is restored. In regions of low density, quantum fluctuations of the scalar field lift the potential and symmetry breaking occurs. This allows the field to mediate a long-range force of gravitational strength on cosmological scales while satisfying local tests of gravity [4, 8]. In [4] symmetrons were excluded from a large volume of the parameter region.

The rotation curves of galaxies and the large-scale structure of the universe is described by *dark matter*. A dark matter candidate is the *axion*. The existence of the axion was postulated to solve the strong CP problem of the Standard Model of particle physics in 1982 by [9]. An axion couples spin to mass and would shift the energy levels of a gravitationally bound particle dependent on the spin of the particle [9]. It was excluded for $\alpha > (3.7 \pm 5.3) \times 10^{-16}$ at a range of $\lambda = 20 \mu\text{m}$ by [6].

Also tests of the Weak Equivalence Principle in the quantum range [10] and further tests of the GR (e.g. Torsion [11, 12]) are promising subjects of μm gravity experiments.

Such predictions motivate gravitational experiments at small distances. *Neutrons* turn out

to be the optimal test masses for such experiments. They are, as massive, neutral hadrons affected by all four fundamental interactions.

The electromagnetic interaction: Although neutrons are electrically neutral they have a magnetic dipole moment $\mu_n = (-1.913\,042\,73 \pm 0.000\,000\,45) \mu_N$ [13] and a spin $\frac{1}{2}\hbar$. This means that they do not interact electrically, but magnetically. Therefore, one of the biggest challenges in precision measurements with neutrons is to shield unwanted external magnetic fields, as they can falsify measurement results. Due to their electrical neutrality (current limit: $q_n = (-0.4 \pm 1.1) \times 10^{-21} e_0$ [14]) and extremely low electrical polarizability ($\alpha_n = (11.8 \pm 1.1) \times 10^{-4} \text{fm}^3$ [15]) systematic effects can be reduced extremely in comparison to atoms. This property makes neutrons very well suited test masses for gravitational experiments.

The weak interaction: The free neutron is not stable. The weak interaction causes the neutron beta decay according to the reaction:

$$n \rightarrow p + e^- + \bar{\nu}, \quad (1.3)$$

with n being the neutron, p the proton, e^- the electron and $\bar{\nu}$ the electron antineutrino. The neutron lifetime is an open field of research. The results of two different measurement methods differ by several standard deviations. For storage experiments the current, most accurate value is $\tau_{\beta,s} = 878.5 \pm 0.7_{\text{sys}} \pm 0.3_{\text{stat}} \text{s}$ [16], for beam experiments it is $\tau_{\beta,b} = 887.7 \pm 1.2(\text{sys}) \pm 1.9(\text{stat}) \text{s}$ [17]. Despite the yet unresolved discrepancy, the neutron lifetime is long enough to qualify them as test masses for gravitational experiments.

The strong interaction: In atomic nuclei, neutrons and protons are tightly bound by the strong nuclear force. The force between a proton and a neutron can be approximated as a spherical square-well potential with a depth of $V \approx 40 \text{MeV}$ and a range of $R \approx 2 \text{fm}$. The force between a free neutron and an atomic nucleus has approximately the same form: Within a range of $R \propto A^{1/3}$, with A being the mass number of the nucleus, the potential is constant, for $r > R$ the potential is drawn towards 0 [18].

Neutrons can be scattered and absorbed by other nuclei. Enrico Fermi was the first to postulate that neutrons can, under certain conditions, also be totally reflected from a surface [19].

When neutrons are slowed down to $v \lesssim 10 \text{m s}^{-1}$, their wavelengths are macroscopic: $\lambda \approx 100 \text{nm}$. Therefore they are exposed to an averaged effective potential V_0 (neutron optical potential) instead of the individual potentials of the nuclei. For total reflection independent of the incident angle, the kinetic energy of the neutrons must be smaller than V_0 of the surface.

The total reflexion from surfaces independent of the incident angle is the defining property of *ultra cold neutrons* (UCNs). V_0 is material specific, some examples can be found in table 1.1 [18].

Table 1.1: Some examples of V_0 and the according UCN-velocity limit, taken from [18].

Element	V_0 [neV]	v_{UCN} limit [m s^{-1}]
Ni ⁵⁸	335	8.01
Fe	210	6.34
C	180	5.87
Cu	168	5.67
Pb	83	3.89
Al	54	3.21

The existence of UCNS was postulated by [20] in 1959, the production and proof were achieved independently in 1969 by [21] and [22].

The gravitational interaction: Like any massive particle, neutrons are subject to gravity. This is the condition for a test mass of a gravitational experiment.

After the implementation of neutron interferometry by [23] in 1974, the first measurement of a quantum phase shift in the gravity potential with neutrons was performed in 1975 by [24]. With the availability of UCNS other types of gravitational experiments were enabled. Due to their defining property, the total reflection from surfaces, UCNS form quantum mechanical bound states above a horizontal surface in the gravity potential. The first experiments for the investigation of those gravitationally bound states of UCNS were proposed in 1978 by [25]. The experimental evidence of such bound states was provided by [26] in 2002.

Gravity experiments with UCNS are promising. The quantum mechanical nature of their bound states in the gravitational field builds a bridge between quantum mechanics and gravity.

The instrument PF2 at the Institut Laue Langevin (ILL) in Grenoble provides the highest flux of UCNS worldwide. For this reason *q*BOUNCE is situated there.

*q*BOUNCE is a collaboration of the TU Wien and the ILL. The collaboration exists since 2007 and is permanently installed at the UCN beam site on PF2 since 2016. The UCN source of PF2 and the UCN beam site are described in more detail in chapter 2 of this thesis.

Numerous experiments have been carried out within *q*BOUNCE since 2007. To measure the dynamics of quantum mechanical wave packets of UCNS, their time evolution after falling down a defined vertical step has been investigated in the past. Spatially resolved measurements of the quantum mechanical probability density for different propagation times were performed [27]. Furthermore methods of resonance spectroscopy are used to measure the bound states and the associated energies of UCNS in the gravity field. The *Rabi method*, was applied to UCNS within the *q*BOUNCE Rabi setup [4]. In 2017 the setup was extended to a *Ramsey-type setup* [28, 29]. A detailed description and theoretical calculation is given in chapter 3. Furthermore, the gravitationally bound states of UCNS and the according energies are derived in this chapter.

In the course of this thesis, four months (June - October 2019) were spent at the experiment in Grenoble. During this time two beamtimes took place in which the Ramsey spectrometer was implemented and optimized.

For the execution of the above mentioned resonance spectroscopy methods, the determination of the velocity spectrum of the UCNS is of great interest.

Two different measurements were carried out to determine the velocity spectrum: an aperture measurement and a measurement of the pressure-rate dependence. The data of those two measurements and an additional data set of the time of flight measurement performed by Tobias Jenke and Stephanie Rocca were used in the analysis. In chapter 4 the results of the time of flight measurement and the aperture measurement are presented, interpreted and compared. Furthermore, the course of the rate of the beam monitor during the first beam time is evaluated and analyzed. In chapter 5 the evaluation of the "main measurement" of this thesis is described step by step. The measurement of the rate-pressure dependence allows several interpretations. This thesis deals with the calculation of the mean neutron velocity and the calculation of the mean cross section for neutrons of air.

Chapter 2

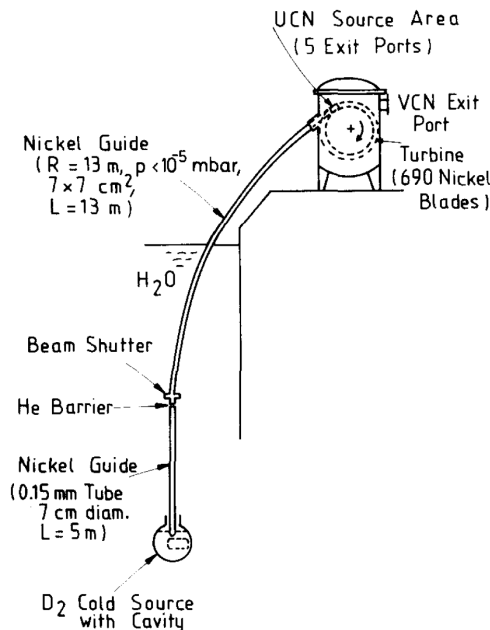
Setup

2.1 UCN beam site

The Institut Laue-Langevin (ILL) in Grenoble is the most powerful neutron source in the world. The reactor operates with up to 58 MW thermal power. With only one fuel element, a constantly high neutron flux is achieved over the length of a full cycle (40-60 days) [30].

Nuclear fission produces hot neutrons in the reactor core. These are moderated with heavy water (D_2O). Once the neutrons are in thermal equilibrium with the moderator, they pass through the cold source, a tank of liquid deuterium. Here they are slowed down further, to about 50 m/s. They transit a vertical guide that decelerates the neutrons further, and enter a total-reflection neutron turbine that is situated at the instrument PF2. In the turbine the neutrons are transformed into the UCN regime. The UCN source at the ILL is the world's strongest UCN source, both in terms of current density and neutron flux [18, 31].

Figure 2.1: Scheme of the UCN source. A vertical guide tube conducts slow neutrons from the cold source to the turbine where the neutrons are decelerated to the UCN regime. The figure was taken from [31]



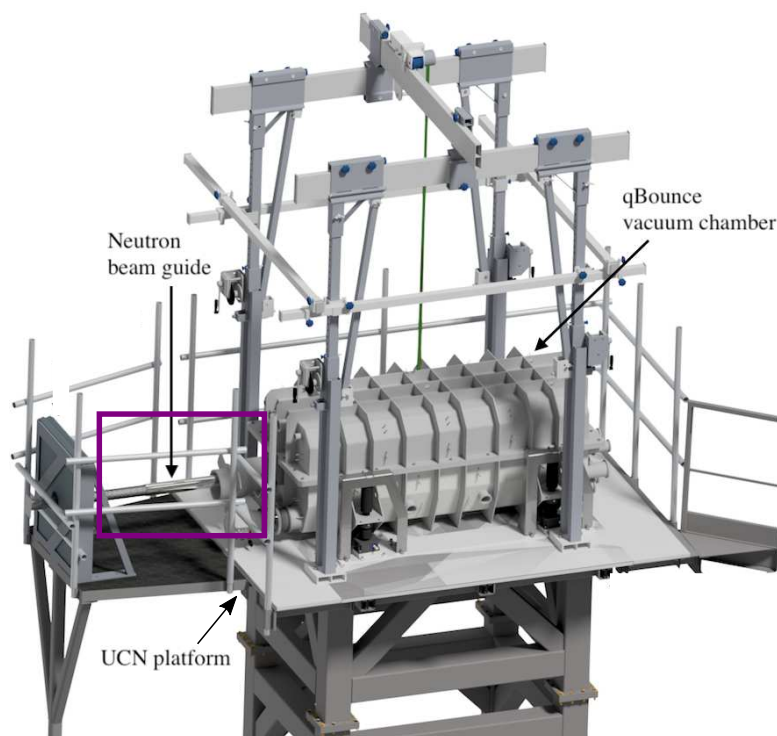
The turbine supplies four beam sites with UCNs: MAM, UCN, EDM and TEST. Another beam site is designed for VCNs (very cold neutrons). These neutrons are guided past the turbine. Together with the turbine, these five beam sites form the instrument PF2. Of the four UCN-supplied beam sites, only TEST has a continuous beam, but with low intensity. The other three are alternately supplied with UCNs.

There is a main shutter for the whole PF2 instrument. In addition there is an experiment shutter for each of the beam sites.

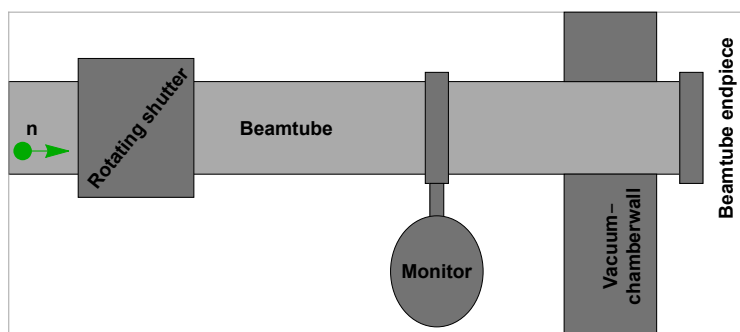
The experiment q BOUNCE is set up on the UCN beam site (see figure 2.2) which is located on a platform. A horizontal neutron guide leads from the turbine to the experiment [30].

Figure 2.2: q BOUNCE setup

(a) Schematic setup of the q BOUNCE experiment on the UCN platform at PF2. The purple framed section can be seen in more detail in (b). This 3D rendering was designed by [28]



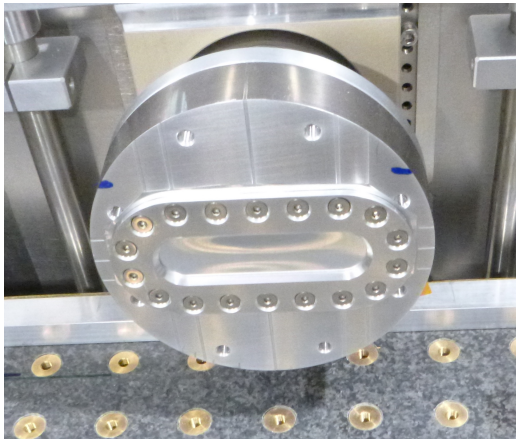
(b) Sketch of the beamline setup of the q BOUNCE experiment



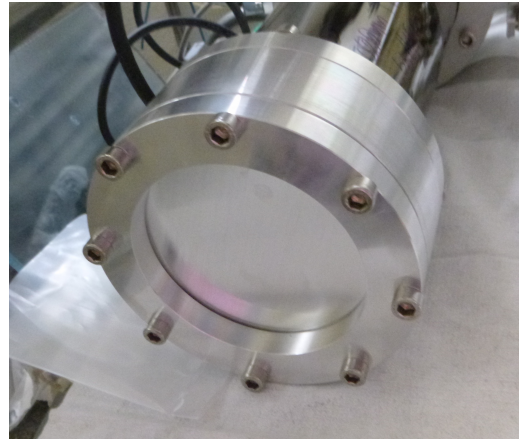
Behind the experiment shutter, a rotating shutter is installed. It can be operated pneumatically and is used to block the beamtube during background measurements. After the rotating shutter, a beam monitor is mounted on a joint between two neutron guides. The neutron guide leads into the vacuum chamber. It is closed by a beamtube endpiece, which consists of a steel-framed, $\approx 100\ \mu\text{m}$ thick aluminium-magnesium (AlMg) foil. This allows separated vacua in the beamtube and in the vacuum chamber, while neutrons still pass through (Al has a very low effective neutron optical potential, the velocity-limit for total reflection is $\approx 3.21\ \text{m s}^{-1}$, see table 1.1, while only neutrons in the velocity range of $[5, 13]\ \text{m s}^{-1}$ are used in the experiment). The beamtube endpiece was replaced at the beginning of cycle 185/19-1 (see figure 2.3).

Figure 2.3: Beamtube endpiece

(a) Old beamtube endpiece: Coated steel with outlet slit. The slit is covered with AlMg foil. All neutrons not passing through the slit are reflected back into the beamtube.



(b) New beamtube endpiece: the whole surface is covered with AlMg foil. The neutrons can exit the beamtube over the whole cross-section.

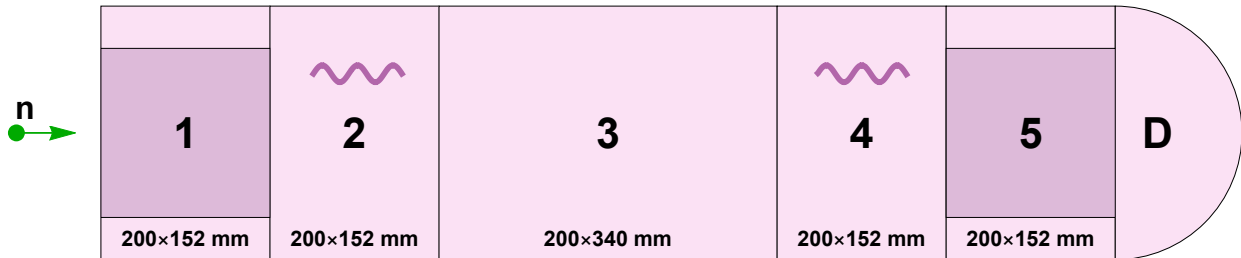


Directly behind the end of the beamtube there is a boron steel aperture which is used to select the neutron velocity interval in flight direction: $[5, 13]\ \text{m s}^{-1}$ (see also section 4.1.2). The beamtube endpiece and the aperture are surrounded by a construction of boron containing mats. This construction has an outlet slit in flight direction. It absorbs all neutrons that do not pass through this slit and collimates and focuses the neutron beam [32]. In the vacuum chamber, behind the construction of boron containing mats, the *q*BOUNCE Ramsey setup is installed.

2.2 The *q*BOUNCE Ramsey setup

The experimental setup consists of seven neutron mirrors: five polished neutron mirrors (section 1-5) that are aligned sequentially and two roughened neutron mirrors above section 1 and 5 that act as state selectors. The dimensions of the individual regions can be taken from figure 2.4.

Figure 2.4: Sketch of a Ramsey-type setup. Section 1-5 with dimensions (width×length) and neutron detector D. The state selectors above section 1 and 5 are indicated in dark. Section 2 and 4 are oscillated (indicated by the waves), in section 3, the longest section, the neutrons propagate freely.



The neutron mirrors¹ are made of optical crown glass and have an optically reflective aluminium coating on top. The coating is used to monitor the mirrors via laser interferometer and capacitive sensors.

The mirrors are mounted on a nanopositioning² stage. Adapter plates with clamps for mounting the mirrors are implemented between the neutron mirrors and the nanopositioning stages. The stages can be adjusted in height within a certain range. For the different types of stages, the ranges are 50 μm , 100 μm and 200 μm . Their horizontal axes can be adjusted within $\pm 500 \mu\text{rad}$. The stages can be operated in closed-loop mode, meaning that they actively readjust the positions with an accuracy of $< 0.1 \mu\text{m}$ and $< 1 \mu\text{rad}$. Furthermore the stages are used to oscillate the mirrors. Their control units have analog inputs where signals from a frequency generator can be fed in [28].

The Ramsey setup consists of five sections. Section one and five are state selector systems. The roughened neutron mirrors are positioned on top of the polished neutron mirrors, with brass spacers in between. They are held by four fine threaded screws which press them onto the brass spacers. The spacers allow the adjustment of a defined distance between polished and roughened neutron mirror. The system is used for state preparation: the state selector scatters the higher states out of the system, a more detailed description follows in section 3.2.1. Section 2 and 4 are the oscillating regions of perturbation and section 3, the only longer mirror, is the region where the neutrons propagate. These are described in detail in section 3.2.2. A neutron detector is placed behind the five sections. It is described in more detail in section 5.1.2.1.

In addition to the five mirrors which constitute the essential setup for Ramsey's resonance method, there is a supplementary mirror that acts as a reference for the step control system described below. It is mounted on an aluminum block without a nanopositioning stage.

For a Ramsey setup it is very important that the mirrors are aligned without steps. A system of capacitive sensors has been developed for this purpose: Above the mirrors a high-precision linear stage (miCos³) is mounted. It can travel a distance of 12" ($\approx 300 \text{ mm}$) with an accuracy of some μm . The miCos is fixed to an aluminium gantry and holds capacitive sensors with a distance of approximately 150 μm to the surfaces of the mirrors. By moving the miCos, all mirrors can be mapped by the capacitive sensors. Any steps or gradients in the setup are thus detected and corrected with the nanopositioning stages.

¹POG Präzisionsoptik Gera GmbH

²Physik Instrumente, Type: P-518.TCD, P-528.TCD and P-558.TCD.

³Physik Instrumente, Type: HPS-170.

For the measurements in the vacuum chamber described in this thesis the Ramsey setup was not installed. For the aperture measurement (see section 4.1.2) only section 1 was placed between the aperture and the detector. For the measurements of the dependency of the neutron rate on the pressure (see chapter 5), there were no neutron mirrors involved. Only the distance between the detector and the beamtube endpiece was varied.

Chapter 3

Theory

3.1 UCNs in the gravity potential

3.1.1 Eigenenergies

A massive particle, in this case a UCN, over a horizontal surface at $z = 0$ exposed to the gravity potential can be described by the Schrödinger equation in position space with

$$i\hbar \frac{d}{dt} \psi(\vec{r}, t) = \underbrace{\left(-\frac{\hbar^2}{2m} \Delta + mgz + V_0 \Theta(-z) \right)}_{\hat{H}} \psi(\vec{r}, t), \quad (3.1)$$

where $\hbar = \frac{h}{2\pi} = \frac{1}{2\pi} 6.626\,070\,15 \times 10^{-34}$ J s is the reduced Planck constant (with h being the Planck constant) [13], $\psi(\vec{r}, t)$ the neutron's wave function, $\Delta = \partial_x^2 + \partial_y^2 + \partial_z^2$ the Laplace operator, Θ the Heaviside step function and \hat{H} the Hamilton operator.

$m \approx (1.674\,927\,498\,04 \pm 0.000\,000\,000\,95) \times 10^{-27}$ kg is the mass of the neutron [13], g is the gravitational acceleration with $g = (9.805\,07 \pm 0.000\,02)$ m/s² being the local value at Grenoble and the default value of the *q*BOUNCE experiment [4]. V_0 is the neutron optical potential of the surface (see chapter 1).

The eigenstates $\psi_n(\vec{r})$ of the time independent Hamilton operator and the corresponding energy eigenvalues E are described with the time independent Schrödinger equation:

$$E\psi_n(\vec{r}) = \hat{H}\psi_n(\vec{r}). \quad (3.2)$$

If the potential term depends only on z , equation 3.1 can be decoupled: $\psi_n(\vec{r}) = \psi_n(x)\psi_n(y)\psi_n(z)$. The solutions for $\psi(x)$ and $\psi(y)$ describe a free particle and are given by $\psi(x) = e^{-ik_x x}$ and $\psi(y) = e^{-ik_y y}$, with k_x and k_y being the x - and y -component of the wavevector \vec{k} .

In the following only the z -component is considered and $\psi_n(\vec{r}) \rightarrow \psi_n(z)$.

The Fermi potential $V_0 \approx 100$ neV is associated with the substance of the mirror. It is repulsive and much larger than the UCN eigenenergies in the gravity field (as will be shown below) [33].

Therefore the UCNS' wavefunction $\psi_n(z) \approx 0$ for $z \leq 0$ and the $V_0\Theta(-z)$ -term can be replaced by corresponding boundary conditions, leading to discrete energy eigenvalues $E \rightarrow E_n$ and

$$E_n \psi_n(z) = \begin{cases} \left(\frac{-\hbar^2}{2m} \frac{d^2}{dz^2} + mgz \right) \psi_n(z) & , z > 0 \\ 0 & , z \leq 0. \end{cases} \quad (3.3)$$

With the substitution $z = \tilde{z}z_0$ where $z_0 = \sqrt[3]{\frac{\hbar^2}{2m^2g}} \approx 5.87 \mu\text{m}$, equation 3.3 can be written as

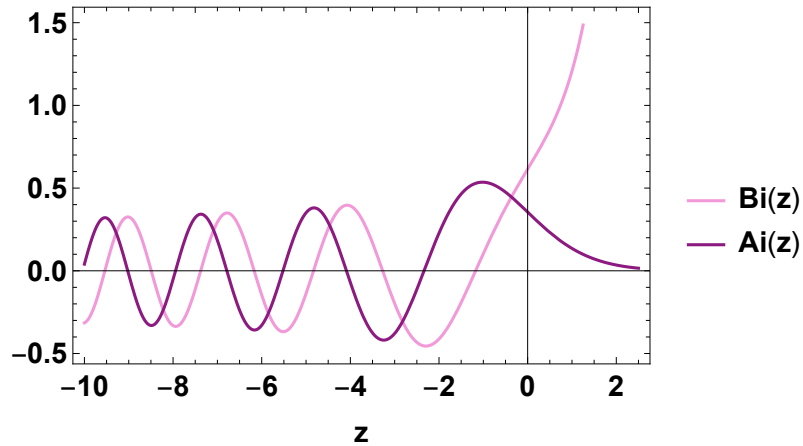
$$\left(-\frac{d^2}{d\tilde{z}^2} - \left(\tilde{z} - \frac{E_n}{mgz_0} \right) \right) \psi_n(\tilde{z}) \leq 0 . \quad (3.4)$$

The shift of $\tilde{z} = z' + \frac{E_n}{mgz_0}$ leads to the Airy differential equation

$$\left(\frac{d^2}{dz'^2} - z' \right) \psi_n(z') = 0 . \quad (3.5)$$

The Airy differential equation has two linearly independent solutions, known as the Airy functions Ai and Bi, shown in figure 3.1.

Figure 3.1: Solutions of the Airy equation Ai(x) and Bi(x).



As $\lim_{z \rightarrow \infty} \text{Ai}(z) = 0$ and $\lim_{z \rightarrow \infty} \text{Bi}(z) = \infty$, only Ai(z) will be considered as the physically relevant solution for the case of the only boundary condition being $\psi(0) \approx 0$.

Resubstituting z in equation 3.5 leads to the final solution of the time independent Schrödinger equation describing a neutron in the gravity potential:

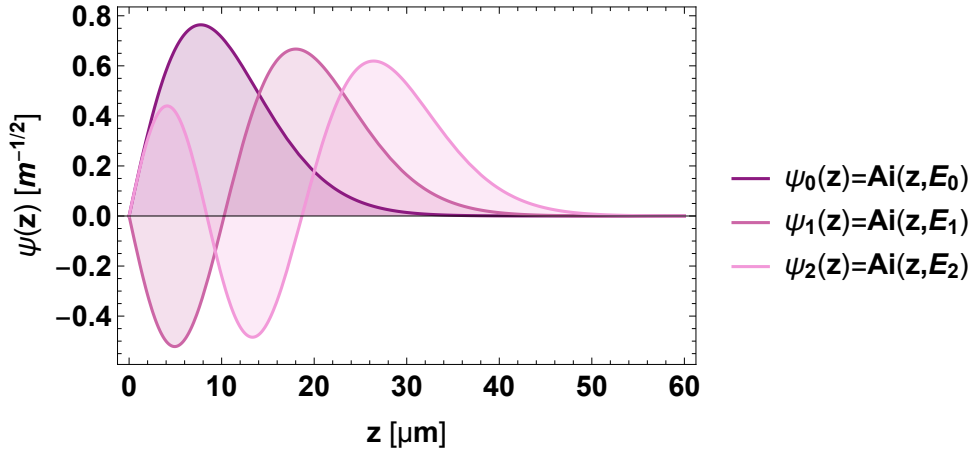
$$\psi_n(z) = \frac{1}{N_n} \text{Ai} \left(\frac{z}{z_0} - \frac{E_n}{mgz_0} \right) , \quad (3.6)$$

with

$$N_n = \int_0^{\infty} \text{Ai} \left(\frac{z}{z_0} - \frac{E_n}{mgz_0} \right)^2 dz = z_0 \frac{d\text{Ai}(z)}{dz} \Big|_{-\frac{E_n}{mgz_0}} \quad (3.7)$$

being the normalisation factor [34]. The first three eigenfunctions $\psi_n(z)$ are shown in in figure 3.2.

Figure 3.2: First three eigenfunctions for neutrons in a gravitational potential.



The boundary condition $\psi_n(z < 0) = 0$ determines the eigenenergies:

$$\psi_n(0) = \text{Ai}\left(-\frac{E_n}{mgz_0}\right) = 0 \Rightarrow E_n = -mgz_0 \text{Ai}_n^0, \quad (3.8)$$

with Ai_n^0 being the n -th zero crossing of $\text{Ai}(x)$. The eigenenergies of the first three states are 1.407 peV, 2.459 peV, 3.321 peV, respectively.

With the relation between energy E and frequency ν

$$E = h\nu, \quad (3.9)$$

the transition frequencies between two states with energies m and n are given by $\nu_{mn} = \frac{E_m - E_n}{h}$. The first few can be taken from table 3.1.

Table 3.1: First few transition frequencies ν_{mn} [Hz]

n/m	0	1	2	3	4
0	0.	254.535	462.925	647.101	815.462
1	-254.535	0.	208.39	392.566	560.927
2	-462.925	-208.39	0.	184.176	352.537
3	-647.101	-392.566	-184.176	0.	168.361
4	-815.462	-560.927	-352.537	-168.361	0.

For convenience, from now on the angular frequency $\omega = 2\pi\nu$ will be considered instead of the frequency ν . This transforms equation 3.9 into $E = \hbar\omega$.

3.1.2 Oscillating boundary conditions

Transitions between two energy eigenstates of a neutron in the gravity potential are induced by the application of a periodic perturbation. This perturbation can be realized in several ways. In [35] the transitions are driven by an oscillating magnetic gradient. *qBOUNCE* realizes the perturbation in the form of mechanically oscillating neutron mirrors. The frequency and the

amplitude of the oscillation determine the likeliness of the transition.

A general oscillation term $f(t)$ leads to

$$i\hbar \frac{d}{dt} \psi(z, t) = \underbrace{\left(-\frac{\hbar^2}{2m} \frac{d^2}{dz^2} + mgz + V_0 \Theta(-z + f(t)) \right)}_{\hat{H}(t)} \psi(z, t), \quad (3.10)$$

where the Hamiltonian is no longer time independent.

In time-dependent perturbation theory, the wave function $\psi(z, t)$ of the particle can be expressed as a linear combination of the eigenstates of the unperturbed system $\psi_n(z)$

$$\psi(z, t) = \sum_n C_n(t) e^{-iE_n t/\hbar} \psi_n(z), \quad (3.11)$$

where $C_n(t)$ with $|C_n|^2 \in [0, 1]$ are time dependent amplitude coefficients.

After some calculation steps (see appendix A.1) and with the substitutions

$$\begin{aligned} \tilde{z} &= z - f(t), \quad \tilde{t} = t, \\ C(\tilde{t}) &= u(\tilde{t}) \tilde{C}(\tilde{t}), \quad u(\tilde{t}) = T e^{-i \frac{amg}{\hbar} \int_0^{\tilde{t}} f(\tau) d\tau}, \end{aligned} \quad (3.12)$$

with T being the time-ordering operator, a system of differential equations results for the description of $\tilde{C}(\tilde{t})$:

$$\dot{\tilde{C}}_m(\tilde{t}) = f(\tilde{t}) \sum_{n=0}^{\infty} e^{i\omega_{mn}\tilde{t}} V_{mn} \tilde{C}_n(\tilde{t}), \quad (3.13)$$

with V_{mn} being the interaction potential of state m and n . The values of the first few V_{mn} can be taken from table 3.2, the calculation of V_{mn} can be found in equation A.5 in appendix A.1.

Table 3.2: First few interaction potentials V_{mn}

n/m	0	1	2	3	4
0	0	97373.5	-53539.9	38301.5	-30393.8
1	-97373.5	0	118935.	-63135.8	44185.7
2	53539.9	-118935.	0	134572.	-70304.5
3	-38301.5	63135.8	-134572.	0	147213.
4	30393.8	-44185.7	70304.5	-147213.	0

The interaction potentials V_{mn} are real and antisymmetric: $V_{mn} = -V_{nm}$ and $V_{nn} = 0$. This means that the transition probabilities are symmetrical. A transition $\psi_m \rightarrow \psi_n$ is as likely as the reverse process $\psi_n \rightarrow \psi_m$ [36].

To avoid cumbersome expressions, from this point \tilde{z} , \tilde{t} and $\tilde{C}(\tilde{t})$ will be referred to as z , t and $C(t)$.

Equation 3.13 is the system of differential equations describing the occupation C_m of a state m in a system of infinitely many states. The oscillation term realized in *qBOUNCE* is sinusoidal with $f(t) = a \sin(\omega t + \phi)$, with a being the amplitude, ω the driving frequency and ϕ a phase. Inserting $\dot{f}(t) = a\omega \cos(\omega t + \phi)$ in equation 3.13 gives

$$\dot{\tilde{C}}_m(t) = a\omega \cos(\omega t + \phi) \sum_{n=0}^{\infty} e^{i\omega_{mn}t} V_{mn} \tilde{C}_n(t). \quad (3.14)$$

Since, in the case of UCNs in the gravitational field, the eigenenergies are not equidistant and therefore the transition frequencies between two states are unique, two arbitrarily selected states can be regarded as a two level system in good approximation.

The consideration of a two level system simplifies the analytical calculation immensely.

3.1.3 Two level system

For a two level system (the two levels being $|i\rangle$ and $|j\rangle$), equation 3.14 can be written as

$$\begin{pmatrix} \dot{C}_i(t) \\ \dot{C}_j(t) \end{pmatrix} = a\omega \cos(\omega t + \phi) \begin{pmatrix} 0 & -V_{ji}e^{-i\omega_{ji}t} \\ V_{ji}e^{i\omega_{ji}t} & 0 \end{pmatrix} \begin{pmatrix} C_i(t) \\ C_j(t) \end{pmatrix}. \quad (3.15)$$

For the sake of clarity, the time dependency of C will no longer be explicitly addressed in the following sections.

All terms oscillating faster than ω will be neglected [36]:

$$\cos(\omega t + \phi)e^{\pm i\omega_{ji}t} = \frac{1}{2} \left(e^{i((\omega \pm \omega_{ji})t + \phi)} + e^{-i((\omega \mp \omega_{ji})t + \phi)} \right) \quad (3.16)$$

and

$$e^{\pm i((\omega + \omega_{ji})t)} \rightarrow 0 \quad (3.17)$$

lead to

$$\begin{pmatrix} \dot{C}_i \\ \dot{C}_j \end{pmatrix} = \frac{1}{2} \begin{pmatrix} 0 & -a\omega V_{ji}e^{i((\omega - \omega_{ji})t + \phi)} \\ a\omega V_{ji}e^{-i((\omega - \omega_{ji})t + \phi)} & 0 \end{pmatrix} \begin{pmatrix} C_i \\ C_j \end{pmatrix}. \quad (3.18)$$

After some calculation (see appendix A.2) the solution of the differential equation 3.18 is obtained. It describes the time evolution of the state occupation of a two level system which is exposed to an oscillating disturbance $a \sin(\omega t + \phi)$:

$$\begin{pmatrix} C_i(t + t_0) \\ C_j(t + t_0) \end{pmatrix} = \underbrace{\begin{pmatrix} e^{\frac{1}{2}i(t-t_0)(\omega - \omega_{ji})} \left(\cos(\frac{1}{2}(t-t_0)R) - i \cos(\theta) \sin(\frac{1}{2}(t-t_0)R) \right) & e^{\frac{1}{2}i((t+t_0)(\omega - \omega_{ji}) + 2\phi)} \left(\sin(\frac{1}{2}(t-t_0)R) \sin(\theta) \right) \\ e^{-\frac{1}{2}i((t+t_0)(\omega - \omega_{ji}) + 2\phi)} \left(-\sin(\frac{1}{2}(t-t_0)R) \sin(\theta) \right) & e^{-\frac{1}{2}i(t-t_0)(\omega - \omega_{ji})} \left(\cos(\frac{1}{2}(t-t_0)R) + i \cos(\theta) \sin(\frac{1}{2}(t-t_0)R) \right) \end{pmatrix}}_{M(t, t_0, \omega, \omega_{ji}, a\omega)} \begin{pmatrix} C_i(t_0) \\ C_j(t_0) \end{pmatrix}, \quad (3.19)$$

with the substitutions given in A.18, A.19, A.20 and A.21 in appendix A.2.

3.2 Resonance Spectroscopy

Resonance spectroscopy is a technique to determine the transition frequency between two states in a quantum system.

It was shown in the previous section, that gravitational eigenstates of UCNs can be treated as two level systems. These are suitable for resonance spectroscopy.

In the following sections two realizations of resonance spectroscopy, the Rabi- and the Ramsey-Method, and its application to UCNs in the gravity field are described.

3.2.1 The Rabi method

The Rabi Method was developed by I. I. Rabi. The original purpose was the measurement of nuclear magnetic moments [37].

The basic idea is to drive a transition between two states $|i\rangle$ and $|j\rangle$ (in the case of magnetic moments spin-up and -down, in the case of UCNs in the gravity potential two gravitational eigenstates) with an oscillating perturbation that couples to the states. In order to determine the transition frequency ω_{ji} , the frequency ω and the amplitude a of the perturbation are varied and the state occupation of $|i\rangle$ and $|j\rangle$ after the perturbation is measured [38].

It is essential that the transition frequency between two eigenstates is distinguishable, i.e. the transition frequencies are unique.

For the following example, an n -level-system (n possible states: $|0\rangle, |1\rangle \dots |n\rangle$) is considered. The example is kept general. However, any special features of the application to gravitational eigenstates of UCNs are discussed.

The setup to implement Rabi's resonance method consists of three sections (see figure 3.4a):

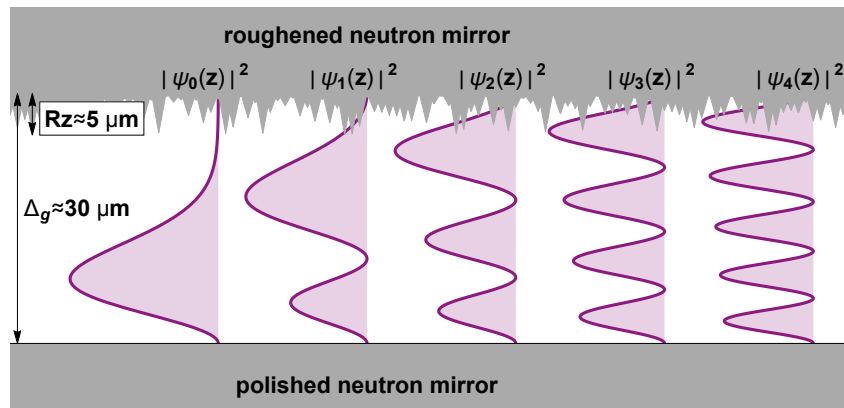
1. **Selector:** One of the n possible states $|i\rangle$, $i \in [0, n]$ is selected. The selection technique depends on the properties of the system.

In the case of UCNs, the ground state $|0\rangle$ is selected. The selector used for this is a system consisting of a lower, flat neutron mirror and an upper roughened one. These are clamped together and separated by a set gap width $\Delta_g \approx 30 \mu\text{m}$. The roughened surface causes neutrons that collide with it to be scattered out of the system.

The roughened neutron mirror acts as a second boundary condition: $\psi(z = 30 \mu\text{m}) = 0$. Due to the second boundary condition the wave function of the UCNs is no longer a pure Airy-Ai(z) function but a linear combination of Ai(z) and Bi(z).

The roughness of the used state selectors was characterized. The arithmetical mean deviation of the profile $Ra \approx 0.5 - 0.6 \mu\text{m}$ and the maximum height of the profile $Rz \approx 5 - 6 \mu\text{m}$, meaning that the largest spikes are up to $5 - 6 \mu\text{m}$, were determined with a roughness meter. The selection of the ground state is due to the probability density $|\psi_n(z)|^2$ of the neutrons in the different gravitational eigenstates: while the $|\psi(z)|^2$ of neutrons in the ground state is negligible at a height of $z \gtrsim 25 \mu\text{m}$: $|\psi_0(z \gtrsim 25 \mu\text{m})|^2 \approx 0$, it is not negligible at higher states (see figure 3.3). As a result, higher states are very likely to be scattered out of the system by colliding with the spikes of the roughened neutron mirror on top, when passing through the state selector system [36].

Figure 3.3: Sketch of a state selector system and probability density of the first 5 wave functions: The higher the state, the higher the probability density for larger distances from the mirror. All neutrons that collide with one of the spikes of the roughened neutron mirror on top are scattered of the system. The longer the neutrons are in the state selector system (i.e. the longer the state selector system is) the more likely it is that the higher states are scattered out.



2. **Perturbation:** A perturbation $a \sin(\omega t + \phi)$, with oscillation frequency ω , amplitude a and phase ϕ between the arrival of the particle and the zero position of the oscillation, interacts with the system for a time τ .

For the gravitational eigenstates of UCNs, this perturbation is realized as an oscillating mirror. The mirror at $z = 0$ represents the boundary condition: $\psi(z = 0) = 0$. When it oscillates, the boundary condition oscillates and transitions are driven (see section 3.1.2). In the q BOUNCE experiment the arrival of the neutron in the perturbation region is random (poisson distributed). This means that ϕ cannot be determined exactly and can only be considered via a convolution.

It can be shown, that the closer ω is to a transition frequency of the system, ω_{ji} , $j \in [0, n]$, the more likely the transition $|i\rangle \rightarrow |j\rangle$ is driven (see section 3.2.1.1).

If $\omega = \omega_{ji}$ and $a\omega V_{ji}\tau = \pi$, with V_{ji} being the interaction potential between the two states $|i\rangle$ and $|j\rangle$ (see section 3.1.2 and appendix A.1), the oscillation will cause a complete reversal of the state occupation (" π -flip").

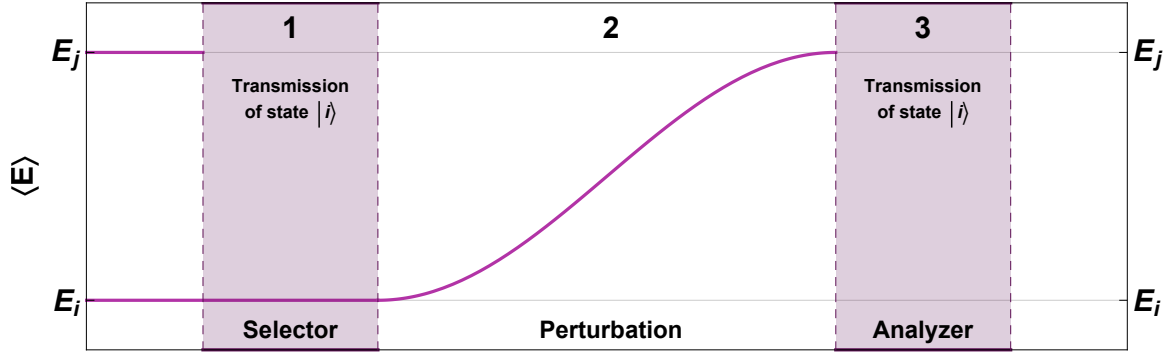
3. **Analyzer:** The state occupations of $|i\rangle$ and/or $|j\rangle$ are observed. When the frequency and the amplitude of the perturbation are varied, the state occupations vary. The case of a π -flip leads to a maximum in the state occupation of $|j\rangle$ i.e. shows a clear resonance [38, 39].

For UCNs, a second state selector system acts as the analyzer. The ground state is selected again, which in case of a π -flip should no longer be occupied, i.e. no neutron should be detected.

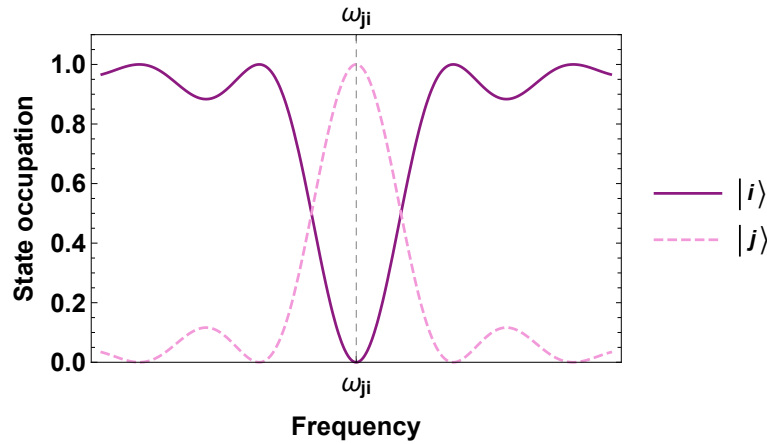
In figure 3.4 the course of the mean energy while passing a Rabi setup is shown. This example shows a π -flip, a complete reversal of the state occupation takes place. Furthermore a typical Rabi curve is shown: state occupation plotted against perturbation frequency. The case of $\omega = \omega_{ij}$ shows a clear resonance.

Figure 3.4: Rabi setup and typical Rabi curve

(a) Rabi setup and course of the mean energy of the system during a Rabi measurement: First an energy E_i is selected. In the perturbation-section, the mean energy moves from E_i to E_j . In this example a π -flip is shown, therefore the mean energy of the system is exactly E_j after section 2. The analyzer selects E_i i.e. no neutron passes the analyzer.



(b) Typical Rabi curve: state occupations of $|i\rangle$ (solid line) and $|j\rangle$ (dashed line) over ω , with the main minimum (solid)/maximum (dashed) at ω_{ji} .



3.2.1.1 The application of Rabi spectroscopy to gravitational eigenstates of UCNS

In section 3.1.2 and 3.1.3 the formalism for the mathematical treatment of an oscillating perturbation is derived.

With equation 3.19 the time evolution of the state occupation of a UCN in the gravity potential is calculated. It can be applied to the Rabi Method.

A UCN is exposed to a perturbation in the form of an oscillating mirror for a certain time τ . Using specific parameters for t_0 , ω , ω_{ji} and $R = \sqrt{a^2 V_{30}^2 \omega^2 + (\omega - \omega_{30})^2}$ (see A.18 and A.19) in M , the state occupation after a time t can be calculated.

In the following, the example $|i\rangle = |0\rangle$ and $|j\rangle = |3\rangle$ will be considered. The initial state is given by

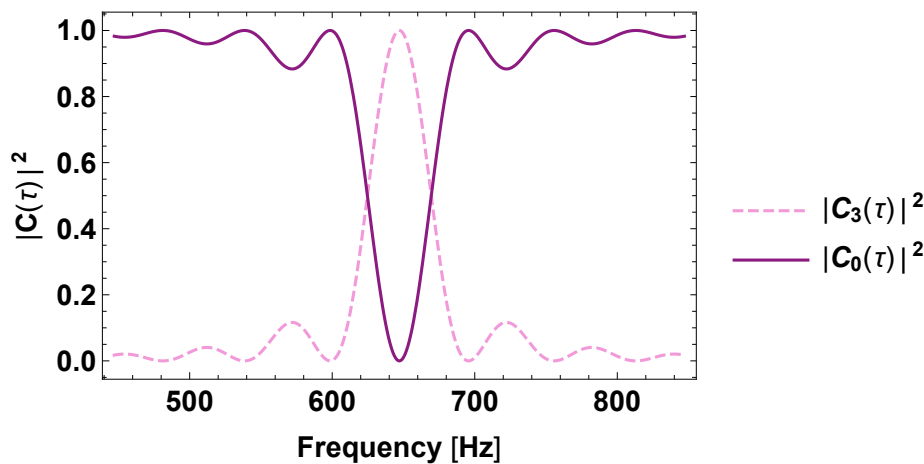
$$\begin{pmatrix} C_0(t_0) \\ C_3(t_0) \end{pmatrix} = \begin{pmatrix} 1 \\ 0 \end{pmatrix}. \quad (3.20)$$

The starting time will be set to zero: $t_0 = 0$ and the interaction time τ calculates from the length of the oscillating region $l = 152$ mm and the velocity of the neutrons, corresponding roughly to the most probable velocity of the neutron beam $v_{opt} \approx 8.525$ m s⁻¹: $\tau = \frac{l}{v_{opt}} = 17.83$ ms. ω_{31} and V_{31} and can be taken from table 3.1 and 3.2 respectively and $a = \frac{\pi}{V_{30}\tau\omega_{30}}$.

For $\omega = \omega_{30}$, this configuration leads to a complete reversal of the state occupation after the oscillation-time τ (see figure 3.5):

$$\begin{pmatrix} C_0(\tau) \\ C_3(\tau) \end{pmatrix} = \begin{pmatrix} 0 \\ 1 \end{pmatrix}. \quad (3.21)$$

Figure 3.5: Rabi spectroscopy: state occupations $|C_0(\tau)|^2$ (solid) and $|C_3(\tau)|^2$ (dashed) after $\tau = 17.83$ ms vs. the oscillation frequency $\omega \in [\omega_{30} - 200, \omega_{30} + 200]$. The narrowness of the peak determines the accuracy of the results.



3.2.1.2 Limitations of the Rabi method

The sensitivity of the Rabi method depends on the interaction time τ . τ is determined by the length of the perturbation and the velocity (distribution) of the particles.

The longer the perturbation, the sharper the peak. This can be controlled over the length L of section 2, as the length of the section of perturbation determines the length of the interaction time.

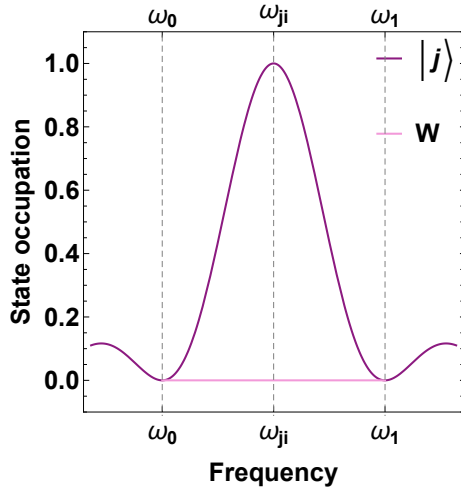
Let the width of the main maximum W be the distance between the next zero points ω_0 and ω_1 (see figure 3.6a). Then W is given by

$$W = 2 \frac{\sqrt{3}\pi v}{L}. \quad (3.22)$$

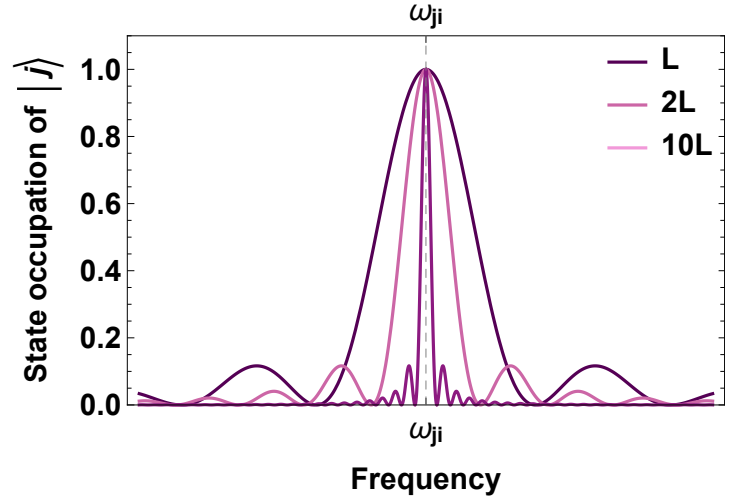
Figure 3.6b illustrates the indirectly proportional relationship between W and L .

Figure 3.6: Width of a Rabi curve

(a) Definition of the width of the main maximum: $W = \omega_1 - \omega_0$.



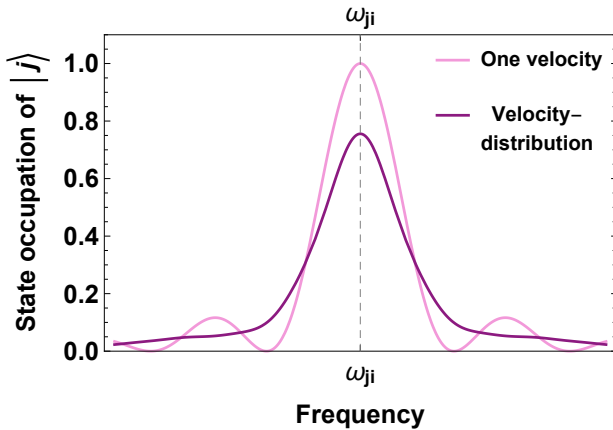
(b) Rabi curve for different lengths of the perturbation section for one velocity ($v = 8.525 \text{ m s}^{-1}$)



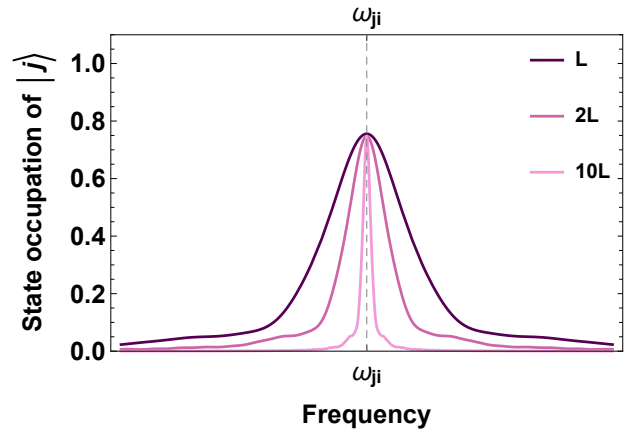
This is limited by the velocity distribution of the particles (see figure 3.7b). As the particles do not have a uniform velocity, the interaction time varies for each particle. The longer section 2, the greater the deviation. Furthermore, an extension of section 2 hits its limits as the quality requirements for the oscillating potentials can no longer be met technically and lead to systematic effects [36].

Figure 3.7: Rabi curve for a velocity-normaldistribution ($\mu = 8.525 \text{ m s}^{-1}$ and $\sigma = 6 \text{ m s}^{-1}$) with $v \in]0, 20] \text{ m s}^{-1}$. A broad distribution was deliberately chosen in order to make the associated effects as visible as possible.

(a) One velocity ($v = 8.525 \text{ m s}^{-1}$) compared to a velocity-normaldistribution (length of the perturbation section = L). The side maxima are washed out and the main maximum is broadened significantly.



(b) Velocity-normaldistribution for different lengths of the perturbation section.



The length of the longest mirror of the q BOUNCE experiment is 340 mm. Longer mirrors

are theoretically possible, but the price increases disproportionately. Furthermore such long and thus heavy mirrors are not suitable for mechanical oscillations. The longest mirror ever oscillated within *qBOUNCE* has a length of 200 mm (setup 2012). It was too heavy for proper oscillations and no improvement in measurement accuracy could be achieved.

The Ramsey method offers a way of improving the sensitivity beyond this limit [40].

3.2.2 Ramsey's method of separated oscillating fields

With the Rabi method, the perturbation, which drives the transition, is extended uniformly throughout one section. The Ramsey method improves this approach. The perturbation is separated into two sections divided by a section in which no perturbation exists and the states evolve. This leads to sharper resonance peaks, as will be shown in section 3.2.2.1.

In accordance with the previous section, an n level system is considered for the following example.

A setup implementing a Ramsey method consists of five sections, section 1 and 5 correspond to section 1 and 3 in the Rabi setup (see figure 3.8a):

1. Selector: selection of state $|i\rangle$, $i \in [0, n]$
2. First perturbation: A perturbation $a_1 \sin(\omega_1 t + \phi_1)$, oscillating with frequency ω_1 , amplitude a_1 and relative phase between particle and oscillation ϕ_1 for a time τ_1 , drives the system into a coherent superposition of the states $|i\rangle$ and $|j\rangle$, $j \in [0, n]$.

If $\omega_1 = \omega_{ji}$, $a_1 \omega_1$ and $V_{ji} \tau_1 = \pi/2$, the oscillation will cause an exact division of the state occupation $|i\rangle \rightarrow \frac{1}{\sqrt{2}} (|i\rangle + e^{i(\omega_{ji}t + \phi_1)} |j\rangle)$ (" $\pi/2$ -flip").

3. Evolution: The state vectors precess with ω_{ji} over a time T .
4. Second perturbation: A perturbation, $a_2 \sin(\omega_2 t + \phi_2)$ is applied.

If $\phi_2 = \phi_1$ and $\omega_2 = \omega_1 = \omega_{ji}$, there is no relative phase shift between the evolved state vector and the second perturbation.

In this case, if also $\tau_2 = \tau_1$ and $a_2 \omega_2 V_{ji} \tau_2 = a_1 \omega_1 V_{ji} \tau_1 = \pi/2$, the second perturbation will apply another $\pi/2$ -flip, i.e. drive the superposition of $|i\rangle$ and $|j\rangle$ into the state $|j\rangle$: $\frac{1}{\sqrt{2}} (|i\rangle + e^{i(\omega_{ji}t + \phi_1)} |j\rangle) \rightarrow |j\rangle$.

If, on the other hand, ω_2 and ω_{ji} differ in that way, that the relative phase shift between the evolved state vector and the perturbation is π , then the second perturbation will drive the superposition of $|i\rangle$ and $|j\rangle$ back into the original state $|i\rangle$: $\frac{1}{\sqrt{2}} (|i\rangle + e^{i(\omega_{ji}t + \phi_1)} |j\rangle) \rightarrow |i\rangle$.

If ω_2 and ω_{ji} are different in the way, that the relative phase shift is an integer multiple of 2π , then the second perturbation will again drive the superposition into the state $|j\rangle$, if it is an odd integer multiple of π , then the second perturbation will drive it back into the original state $|i\rangle$.

One can distinguish between exact resonance and the other cases of $\pi/2$ -flips, as only in the case of exact resonance, the relative phase shift between the first and the second perturbation is velocity independent, i.e. the other cases will not show peaks as high and

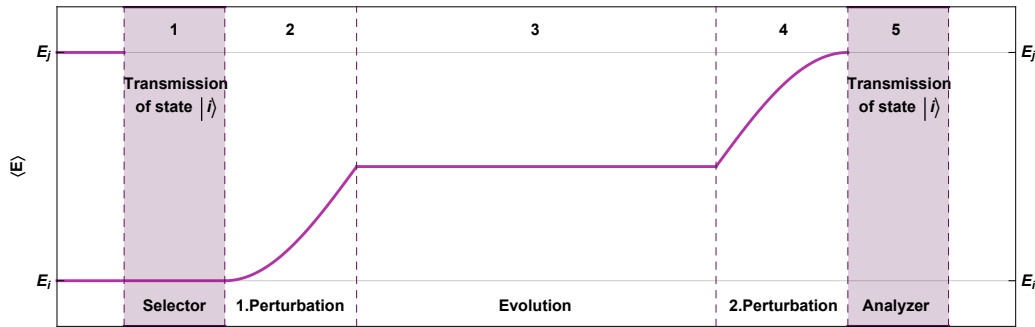
as sharp as the exact resonance and will be referred to as side-maxima (see figure 3.9). This also means, that the shape of the main maximum is less sensitive to a broad velocity distribution than the main maximum in a Rabi measurement (see figure 3.10).

5. Analyzer: The state occupations of $|i\rangle$ and $|j\rangle$ are observed [40].

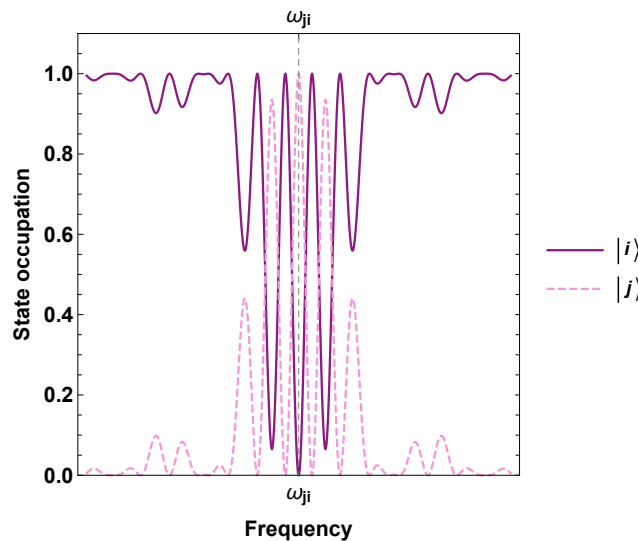
In figure 3.8a the course of the mean energy of the system during a Ramsey measurement is shown. This example shows two $\pi/2$ flips with $\omega_{p1,2} = \omega_{ji}$ and $\phi_2 = \phi_1$. Figure 3.8b shows the state occupation of $|i\rangle$ and $|j\rangle$ over $\omega_{p1} = \omega_{p2}$. The curve is also referred to as Ramsey fringes.

Figure 3.8: Ramsey setup and Ramsey fringes

(a) Ramsey setup and course of the mean energy of the system during a Ramsey measurement: An energy E_i is selected. In the first perturbation-section, the system is driven into a coherent superposition and the mean energy moves from E_i to $\frac{1}{2}(E_j + E_i)$. After the state evolves in the third region, the second perturbation drives the system into state $|j\rangle$ with mean energy E_j (as this example shows two $\pi/2$ flips). The analyzer selects E_i , so that no neutron passes the analyzer.



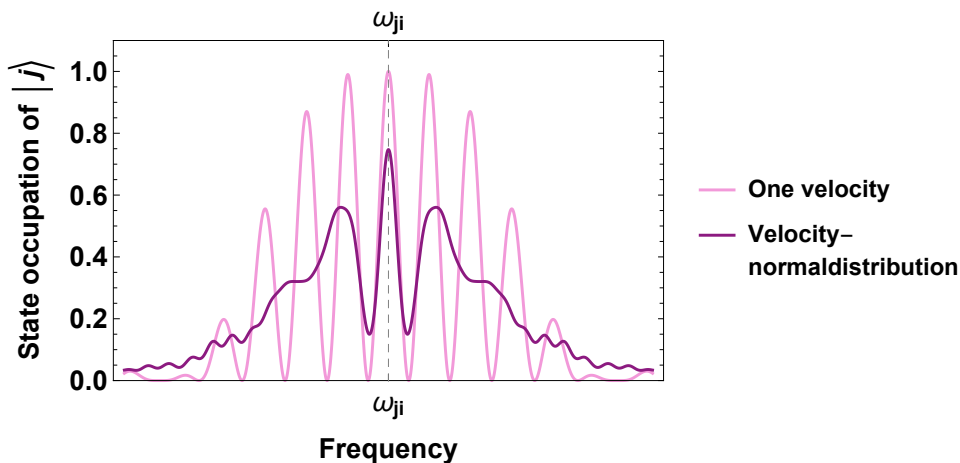
(b) Typical Ramsey fringes: state occupations of $|i\rangle$ (solid line) and $|j\rangle$ (dashed line) over ω , with the main minimum (solid)/maximum (dashed) at ω_{ji} . The side maxima/minima are referred to as Ramsey fringes.



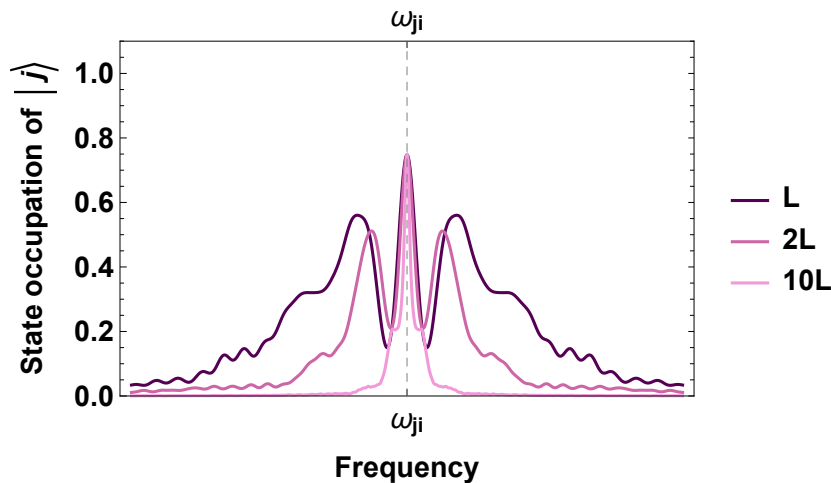
In figure 3.9a the effect of a velocity distribution compared to one single velocity can be seen. While the side maxima are washed out, the sharpness of the main maximum is independent of the velocity spectrum. With increasing the lengths of the perturbation regions, the side maxima get sharper, but the main maximum is not affected (see figure 3.9b).

Figure 3.9: Ramsey curve for a velocity distribution (normaldistribution with $\mu = 8.525 \text{ m s}^{-1}$ and $\sigma = 6 \text{ m s}^{-1}$, $v \in]0, 20] \text{ m s}^{-1}$). While the side maxima are widened to the point of unrecognizability, the main maximum remains sharp.

- (a) One velocity ($v=8.525 \text{ m s}^{-1}$ compared to the velocity-normaldistribution. The length of the first and second perturbation section is L

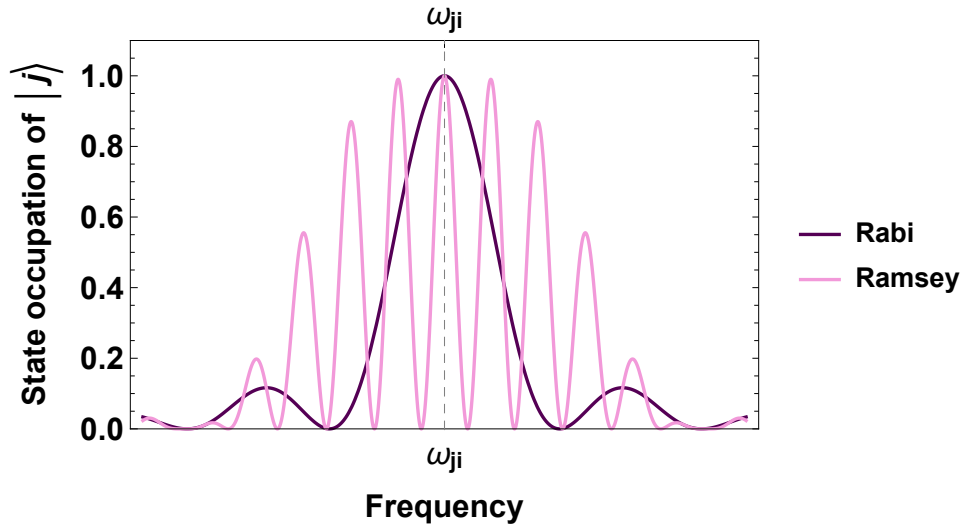
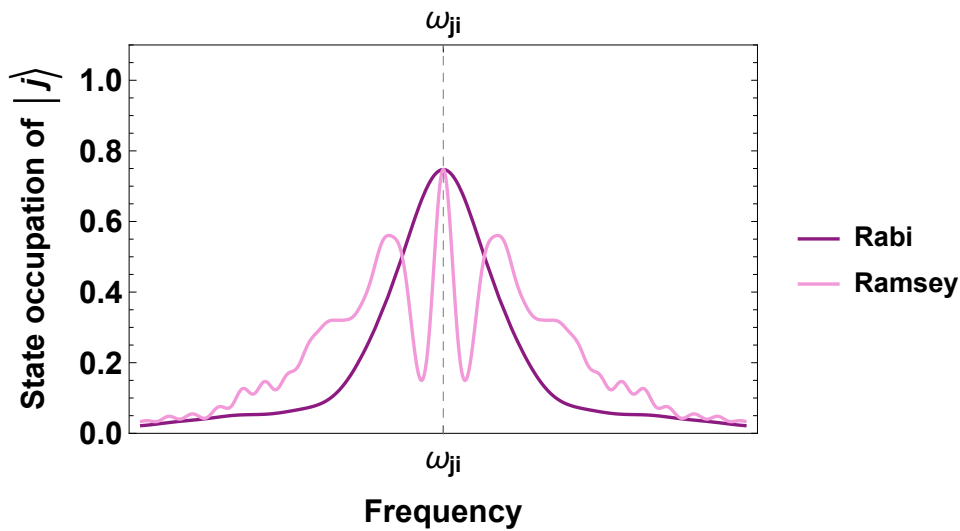


- (b) Velocity-normaldistribution for different lengths of the perturbation sections



In figure 3.10, a Rabi curve is compared to a Ramsey curve. For the Ramsey configuration the length of the two perturbation sections was chosen as half of the length of the perturbation section of the Rabi configuration. Followingly, in this example, the total length of the perturbation section is the same for Rabi and Ramsey. The length of the propagation section of the Ramsey configuration is set to $l_{prop} = 340 \text{ mm}$, the same as in the q BOUNCE Ramsey setup (see figure 2.4 in chapter 2). It can be seen that for both cases, one single velocity (a), and a velocity distribution (b), the Ramsey method leads to a sharper peak at resonance.

Figure 3.10: Rabi vs. Ramsey

 (a) One velocity ($v=8.525 \text{ m s}^{-1}$)

 (b) Velocity-normaldistribution (normaldistribution with $\mu = 8.525 \text{ m s}^{-1}$ and $\sigma = 6 \text{ m s}^{-1}, v \in]0, 20] \text{ m s}^{-1}$)


3.2.2.1 The application of Ramsey spectroscopy to gravitational eigenstates of UCNS

In order to improve the accuracy of the results, the q BOUNCE-collaboration migrated it's experiments from Rabi- to Ramsey spectroscopy [39].

This is realized by using two oscillating mirrors, each of them applying a $\pi/2$ -flip. They are separated by a non-oscillating mirror, above which the UCNS propagate freely.

In the following example, in analogy to the example given in the previous section, $|i\rangle = |0\rangle$ and $|j\rangle = |3\rangle$ will be considered.

Again, the initial state is

$$\begin{pmatrix} C_0(t_0) \\ C_3(t_0) \end{pmatrix} = \begin{pmatrix} 1 \\ 0 \end{pmatrix}. \quad (3.23)$$

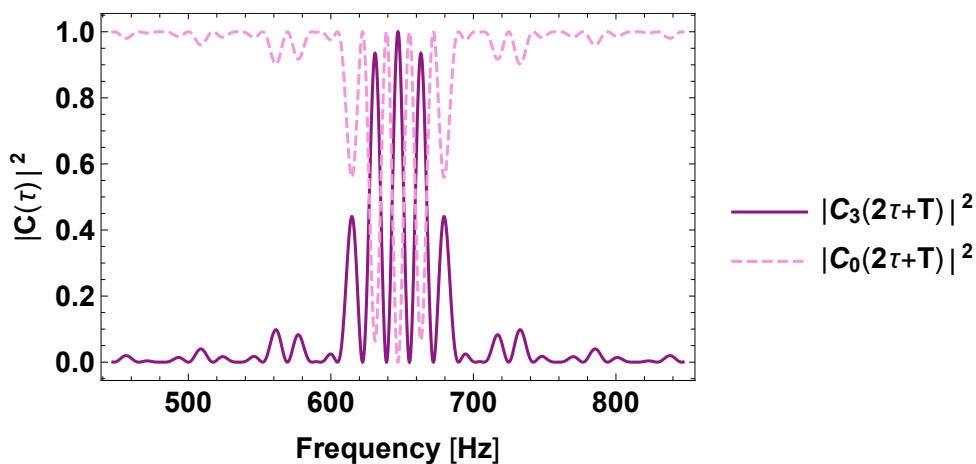
For the calculation of the state occupation after the Ramsey setup, the matrix M from equation 3.19 is applied to the initial state three times:

1. First perturbation: $t \in [t_0 = 0, \tau]$, $\tau = 17.83$ ms (see previous section), $\omega \in [\omega_{30} - 200, \omega_{30} + 200]$, $\omega_{ji} = \omega_{30}$, $a = \frac{\pi}{2V_{30}\tau\omega_{30}}$ (a is determined so that in case of resonance a $\pi/2$ -flip occurs)
2. Free propagation: $t \in [t_0 = \tau, \tau + T]$, T calculates from the length of the propagation region $l_p = 340$ mm and the the approximate most probable UCN velocity $v_{opt} = 8.525$ m s $^{-1}$: $T = \frac{l_p}{v_{opt}} = 39.88$ ms, $\omega = 0 \rightarrow a = 0$
3. Second perturbation: $t \in [t_0 = \tau + T, 2\tau + T]$, ω and a have the same values as in the first perturbation section

$$\begin{aligned} \Rightarrow \begin{pmatrix} C_0(2\tau + T) \\ C_3(2\tau + T) \end{pmatrix} &= M \left(2\tau + T, t_0 = \tau + T, \omega, \omega_{30}, a\omega = \frac{\pi}{2V_{30}\tau} \right) \\ &\quad M \left(\tau + T, t_0 = \tau, \omega = 0, \omega_{30}, a\omega = 0 \right) \\ &\quad M \left(\tau, t_0 = 0, \omega, \omega_{30}, a\omega = \frac{\pi}{2V_{30}\tau} \right) \begin{pmatrix} 1 \\ 0 \end{pmatrix}. \end{aligned} \quad (3.24)$$

In figure 3.11 the state occupation after a Ramsey-type setup is shown.

Figure 3.11: Ramsey spectroscopy: state occupations $|C_0(2\tau + T)|^2$ and $|C_3(2\tau + T)|^2$ vs. the oscillation frequency



Chapter 4

Properties of the incoming UCNs

4.1 Velocity spectrum

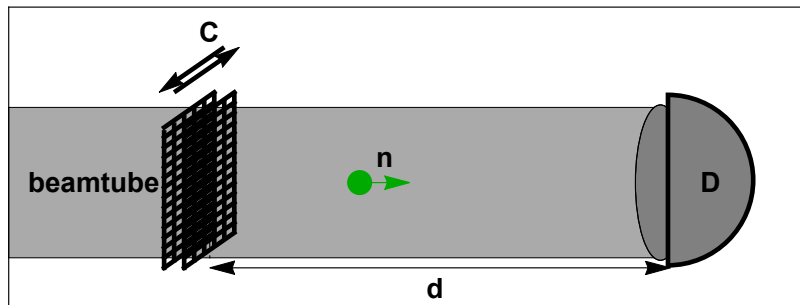
4.1.1 Time of flight measurement

The measurement of the neutron velocity in flight direction can be done with a standard time of flight (TOF) measurement:

The incident neutron beam is divided into neutron bunches by a UCN chopper¹. These bunches smear out over the flight path (of a defined length d) due to the different neutron velocities. At the end of the flight path there is a cascade neutron detector² that measures the time-resolved neutron count rate.

As soon as the chopper window opens, the detector receives a trigger signal from the chopper. The trigger signal defines the start time t_s . An offset between the trigger signal and the actual opening of the chopper $t_{off} \approx 20.25$ ms has to be taken into account. Together with the time of detection t_d the time of flight can be calculated: $t_{TOF} = t_d - t_s - t_{off}$. Subsequently the neutron velocity in flight direction (henceforth v) i.e. the velocity spectrum can be evaluated: $v = \frac{d}{t_{TOF}}$ [28].

Figure 4.1: TOF setup: The chopper C interrupts the neutron beam. When the chopper window is open, neutrons get through and are, after a certain time t_{TOF} , detected in the detector D.



The TOF measurement was carried out at the beginning of cycle 185/19-1 by Tobias Jenke and Stephanie Roccia. It took place on the UCN beam at PF2.

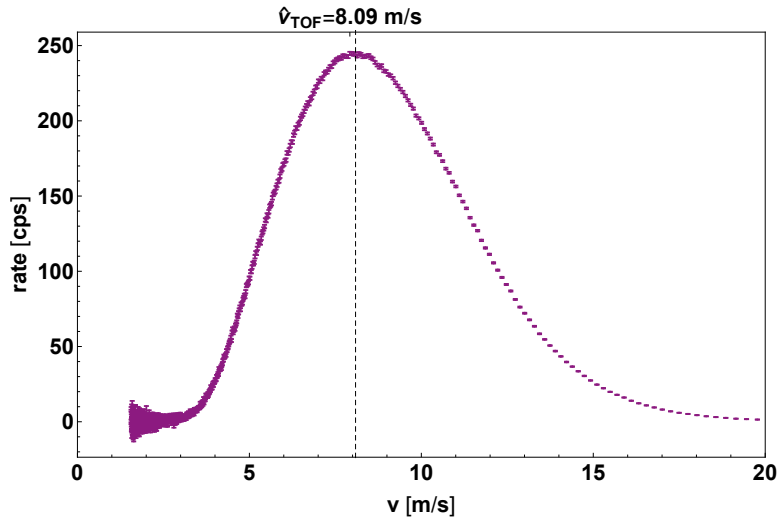
In this experiment, the distance between the chopper and the detector is $d = 608$ mm. The

¹Movatec

²Cascade U, CDT GmbH, Hans-Bunte-Strasse 8-10, D-69123 Heidelberg.

recorded spectrum can be taken from Figure 4.2. It represents the UCN velocity distribution in the beamtube.

Figure 4.2: TOF spectrum: count rate during a TOF-measurement vs. the velocity. It's maximum represents the most probable velocity $\hat{v}_{\text{TOF}} = (8.09 \pm 0.01) \text{ m s}^{-1}$. \hat{v} was determined by fitting the data points near the maximum to a normal distribution (see appendix B.1).



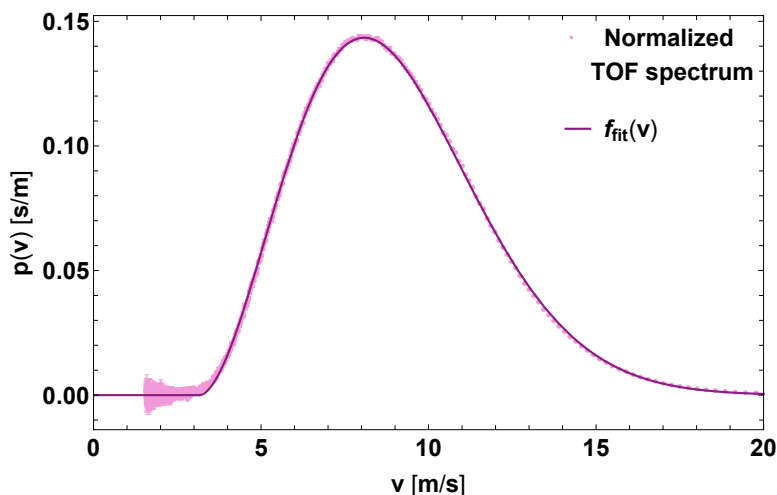
Now the question arises which distribution the spectrum corresponds to. The normalized TOF spectrum was fitted to a Maxwell-Boltzmann-like distribution:

$$f_{fit}(v) = n \sqrt{\frac{2}{\pi}} \frac{(v - v_0)^a}{b^3} e^{-\frac{(v-v_0)^a}{2b^2}} \Theta(v - v_0) . \quad (4.1)$$

Table 4.1: Fit results for the TOF spectrum fit to a Maxwell-Boltzmann-like distribution

	n	v_0	a	b
Estimate	0.71	3.16	1.77	2.90
Standard Error	0.001	0.003	0.001	0.006

Figure 4.3: Normalized TOF-spectrum compared to the fit-function.



In order to estimate the velocity distribution for further calculations, the central moments of the normalized TOF spectrum are calculated.

The central moment μ_n of a univariate continuous distribution $\rho(v)$ taken about the mean $\bar{v} = \int_{-\infty}^{\infty} v\rho(v)dv$ is

$$\mu_n = \int_{-\infty}^{\infty} (v - \bar{v})^n \rho(v) dv . \quad (4.2)$$

The μ_n are characteristic quantities describing the distribution. The first central moments are intuitively understandable: $\mu_0 = 1$ comes with the normalization of the distribution, $\mu_1 = 0$ follows from the definition of \bar{v} . μ_2 is the variance of the distribution and μ_3 and μ_4 are the skewness and the kurtosis respectively.

For a list of N datapoints, the n th central moment about the mean $\bar{v} = \frac{1}{N} \sum_1^N v_i$ is given by

$$\mu_n = \frac{1}{N} \sum_1^N (v_i - \bar{v})^n \quad (4.3)$$

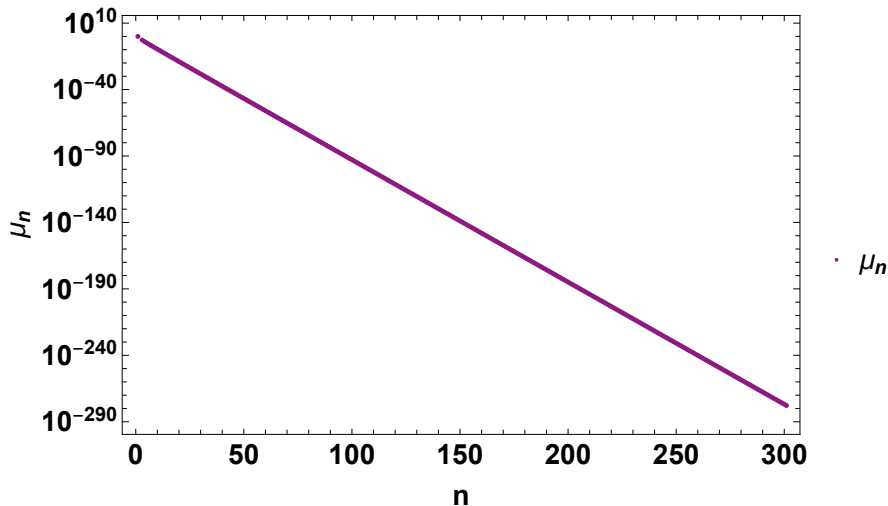
[41]. The first few central moments of the normalized TOF spectrum were calculated in *Mathematica*:

Table 4.2: First 10 central moments of the normalized TOF spectrum.

μ_0	μ_1	μ_2	μ_3	μ_4	μ_5	μ_6	μ_7	μ_8	μ_9
1	0	0.0054	0.0007	0.0001	$2.2 \cdot 10^{-5}$	$4.1 \cdot 10^{-6}$	$7.6 \cdot 10^{-7}$	$1.4 \cdot 10^{-7}$	$2.7 \cdot 10^{-8}$

There first μ_n show a clear convergence towards zero. In order to estimate a high- n behavior of the μ_n , the first 300 were calculated. The result is shown in figure 4.4.

Figure 4.4: First 300 central moments μ_n of the TOF spectrum.



4.1.2 Aperture measurements

A TOF measurement is difficult within the q BOUNCE experiment. Reduced neutron count rates and technical difficulties (space, vacuum) prevent the realization of such a measurement.

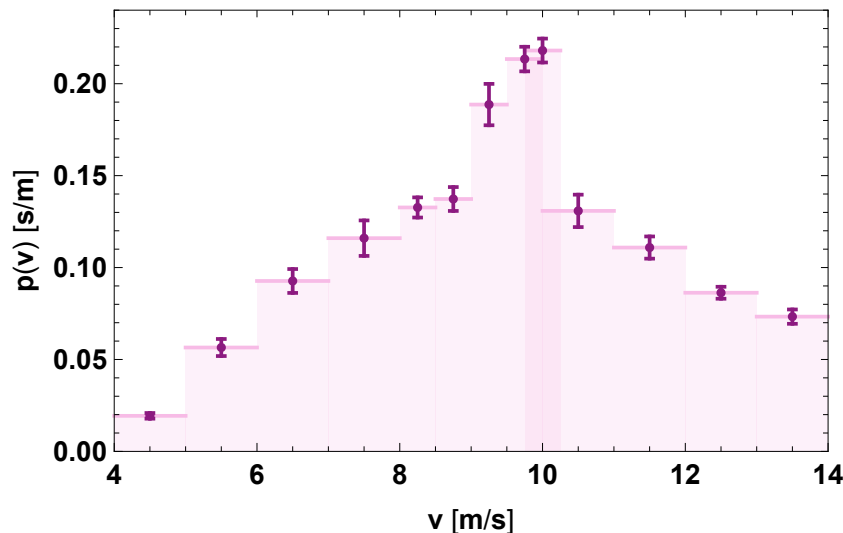
The velocity spectrum in the q BOUNCE vacuum chamber is recorded with a different measurement method.

An aperture is placed directly behind the beamtube endpiece in the vacuum chamber. It contains two height-adjustable blades. Depending on the adjusted height, the blades cut out a part of the velocity spectrum. Thus a velocity interval, in which the velocity of the transmitted neutrons is, can be adjusted.

With repeated adjustment and rate measurement with the respective setting, a correlation between the set height, i.e. velocity interval, and count rate is obtained [28].

The results of the aperture measurement are shown in figure 4.5 [42].

Figure 4.5: Normalized aperture spectrum: measured distribution of neutron velocity in flight direction. The error bars indicate the statistical error of the measurement. The steps in light rose indicate the velocity interval of the respective measurement. An interval-width of $\Delta v = 1 \text{ m s}^{-1}$ was examined. With the exception of the area of the peak at $8.5 - 10 \text{ m s}^{-1}$. Here intervals of $\Delta v = 0.5 \text{ m s}^{-1}$ width and an additional interval $[9.75, 10.25]$ (the overlap of the integrals is dark) were investigated.



There is a clear peak at $8.5-10 \text{ m s}^{-1}$ in the aperture spectrum. This does not meet the expectations, as the maximum of the TOF measurement (see section 4.1.1) is well below. A detailed evaluation and interpretation can be found in [42].

The first 10 central moments of the distribution were calculated according to equation 4.3 and can be found in table 4.3.

Table 4.3: First 10 central moments of the normalized aperture spectrum.

μ_0	μ_1	μ_2	μ_3	μ_4	μ_5	μ_6	μ_7	μ_8	μ_9
1	0	0.0032	0.0004	0.0002	$3.17 \cdot 10^{-7}$	$2.11 \cdot 10^{-7}$	$1.79 \cdot 10^{-9}$	$1.95 \cdot 10^{-9}$	$4.08 \cdot 10^{-12}$

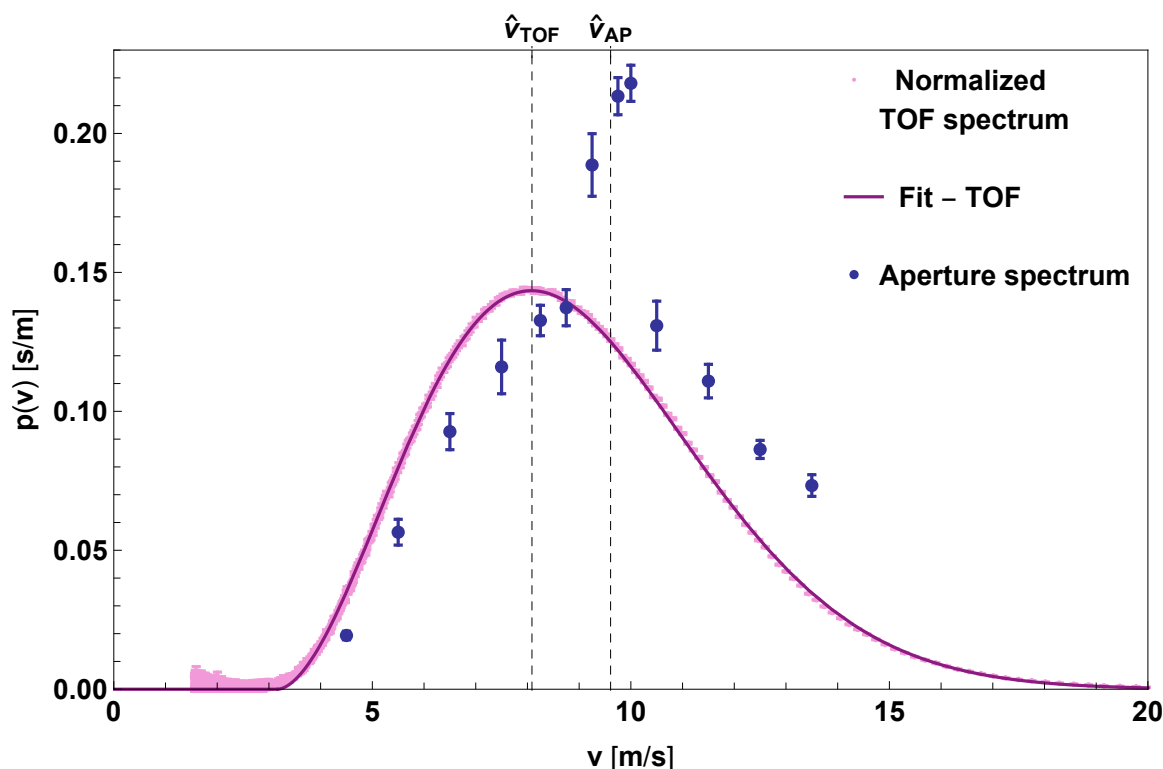
Although the central moments do not go strictly monotonously towards zero, they lose an order of magnitude every two n .

4.1.3 Comparison of the two spectra

It is obvious that the aperture spectrum does not match the TOF spectrum.

The peak at $8.5\text{--}10\text{ m s}^{-1}$ in the aperture spectrum is a deviation from a smooth distribution. This could be caused by geometrical effects. But even if the peak did not occur, the spectrum is shifted compared to the TOF spectrum (see figure 4.6). The most probable velocity of the aperture spectrum is $\hat{v}_{AP} = 9.76\text{ m s}^{-1}$ (see appendix B.2) whereas it is $\hat{v}_{TOF} = 8.09\text{ m s}^{-1}$ in the TOF spectrum.

Figure 4.6: Comparison of the TOF- and aperture spectra. While the maximum of the TOF spectrum is as $\hat{v}_{TOF} = 8.09\text{ m s}^{-1}$, the maximum of the aperture spectrum is shifted to $\hat{v}_{AP} = 9.76\text{ m s}^{-1}$.



In principle, a TOF-like measurement is more reliable than our aperture measurement. Some uncertainties and systematics are included in the aperture measurement. The main reason for the additional uncertainty is the low count rate. The neutrons must pass through section 1 after the aperture. A lot of neutrons are scattered out or absorbed, and the count rate decreases from about $\approx 1000\text{ cps}$ (*counts per second*) to $\approx 250\text{ mcps}$ (*millicounts per second*).

On the other hand, the TOF spectrum was not recorded within the experiment. It is only valid for the velocity distribution in the beamtube on the UCN beamport.

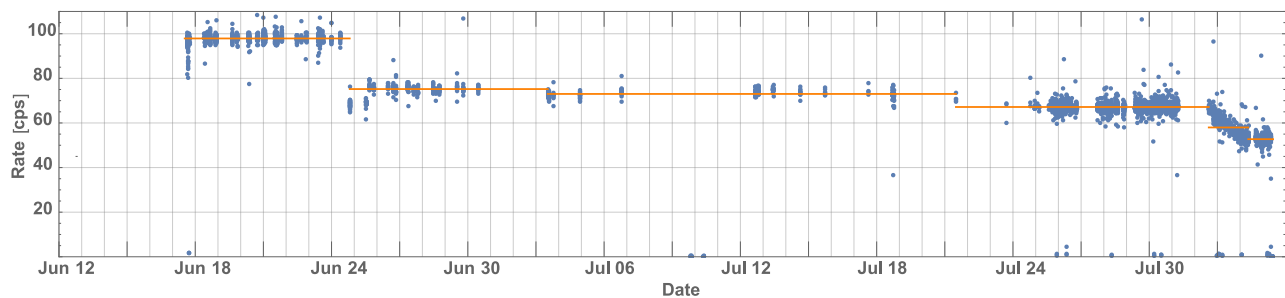
4.2 Monitor detector

The neutron flux of a reactor is statistical in nature and fluctuates. In the q BOUNCE experiment the neutron count rate is the measured quantity. Thus it is sensitive to the stability of the neutron source. A beam monitor is used to monitor the stability of the neutron flux and to

normalize the experiment-rate. It is flanged to a joint between two beamtubes. The neutrons fall through the flange, which is a hole in the bottom of the joint, into the beam monitor. A ^3He detector serves as a monitor detector. It is shielded from the neutron background by a cover made of B_4C -containing blocks and mats.

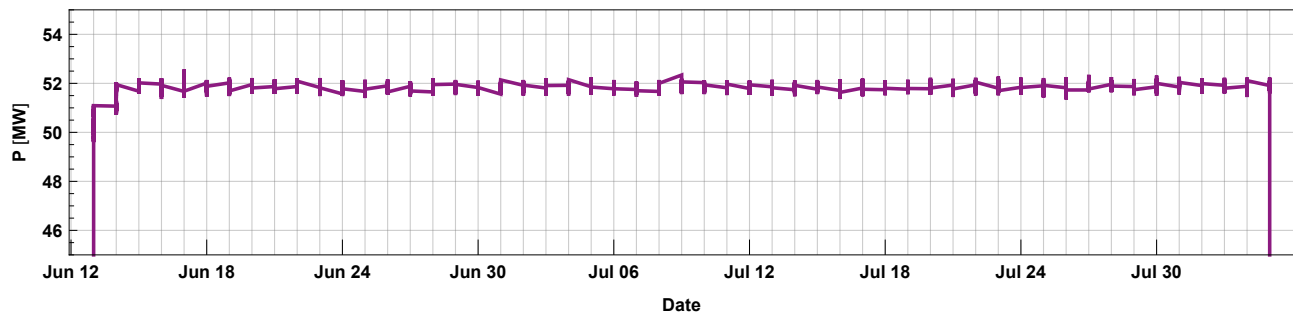
The monitor rate in cycle 185/19-1 was not constant (see figure 4.7).

Figure 4.7: Monitor rate vs. time. In the first few days of the cycle, the monitor detector was dismantled, i.e. no data could be recorded. It was reinstalled on June 17. The rate was constant at about ≈ 98 cps until a sudden drop to about ≈ 75 cps occurred on June 25. On July 20, another jump to ≈ 68 cps occurred. On August 1 the rate gradually dropped to ≈ 53 cps.



A non-constant monitor rate can be caused by fluctuating reactor power. However, since these are clearly downward steps (see figure 4.8), and the reactor power has not decreased in steps, this temporal course of the monitoring rate has another reason.

Figure 4.8: Reactor power over the course of the cycle 185/19-1. It was more or less constant at ≈ 51.8 MW [43].



Probably the unstable positioning of the monitor was responsible for the drops in the monitor rate. The gap between the beamtubes, at whose joint the monitor is mounted, has varied. This is probably due to the ungentle settling of the vacuum chamber lid when closing the vacuum chamber or other mechanical stress affecting the monitor positioning.

An additional rotating shutter is mounted between the experiment shutter and the monitor detector. This closes the beamtube during background measurements.

The rotating shutter became defective during cycle 185/19-1. It no longer opened completely and therefore blocked a part of the neutrons. The continuous decline in the time course of the monitor rate in the end of the cycle probably shows the gradual reduction of the opening of

the rotating shutter.

The rotating shutter was replaced in the following cycle. The measurements analyzed in the following chapter all took place at the beginning of the cycle (17th and 16th of June 2019). Therefore the defect of the rotating shutter and the resulting reduction of the neutron flux did not influence the measurements.

Chapter 5

Pressure dependency of the neutron count rate

The neutron count rate has a strong dependency on pressure. As the pressure decreases, the number of particles decreases, and thus the number of scattering centres in the chamber. The fewer particles in the chamber, the lower the probability that a UCN is absorbed or scattered out on the way from the beamtube endpiece to the detector. This means that the rate increases with decreasing pressure.

During the measurement, the pressure was varied by either pumping vacuum or venting the vacuum chamber. There were six measurements in total, one for pumping vacuum and one for venting the chamber, for each distance.

The goal was to establish a connection between the pressure p and the neutron count rate R and subsequently interpret the results. Especially the measurements while evacuating are interesting for provoking systematics.

In the following sections, the measurements of pumping vacuum and venting the chamber for one distance between detector and beamtube endpiece will be referred to as a measurement row. Quantities that are assigned to a measurement row (e.g. distance, recorded temperature,...) are given with three values. The first refers to the first measurement row with the first distance etcetera.

Quantities that are assigned to a single measurement, have six values. The first corresponds to the pumping-vacuum-measurement with the first distance, the second to the venting-measurement with the first distance etcetera.

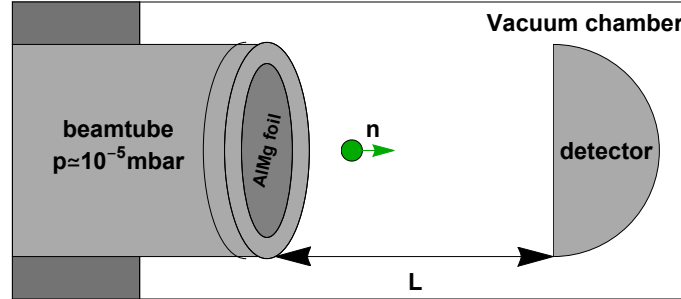
5.1 The effects of pressure on the count rate

5.1.1 Experimental setup

The detector was placed in front of the beamtube.

In the course of the experiment, the distance between detector and beamtube endpiece was varied: $L_1 = (21.8 \pm 0.3)$ cm, $L_2 = (36.8 \pm 0.3)$ cm and $L_3 = (67.9 \pm 0.3)$ cm (see figure 5.1).

Figure 5.1: Measurement setup: The distance L between beamtube endpiece and detector was varied. The pressure inside the beamtube is approximately constant, with $p_{bt} \approx 10^{-5}$ mbar. The pressure in the vacuum chamber is varied (pumping and venting). The two vacua are separated by a thin AlMg foil mounted on the beamtube endpiece.



5.1.2 Neutron count rate

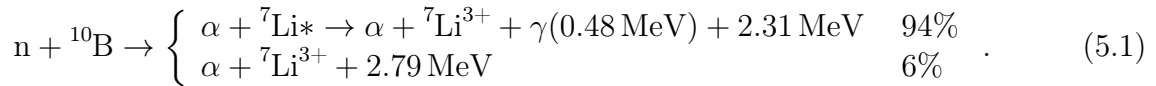
5.1.2.1 Detector

The neutron detector consists of a proportional counter tube with a converter foil attached to its entrance window ($110 \times 3 \text{ mm}^2$). The foil serves as a neutron converter. It is made of aluminium with a thickness of $48 \mu\text{m}$, with a thin ($\approx 200 \text{ nm}$) boron-10 (^{10}B) layer on top.

^{10}B has a high neutron capture cross section (3835.0 b [44]). When a neutron enters the detector foil, a capture is very likely.

After neutron capture, the boron particle decays into an alpha particle ($\alpha = {}^4\text{He}^{2+}$) and a lithium-7 particle (${}^7\text{Li}$).

There are two differently probable decay channels:



The decay products move in opposite directions, whereby one of them enters the proportional counter tube [45].

In the proportional counter tube, a pulse, proportional to the energy of the incoming particle, is generated. It is amplified and digitized using a commercially available analog-to-digital-converter, a quadADC¹. The software *InterWinner* interprets the output of the quadADC. It generates the *list-file*. LabVIEW reads the list-file and creates the *hist-file*. The data format is well-adapted to the needs of the *q*BOUNCE experiment [30]: For each detected signal, its timestamp, its peak energy, and two gate informations are recorded.

5.1.2.2 Hist-File

The hist-file contains the information how many impacts per channel were counted during a measurement.

The quadADC has a 16 bit resolution, so there are $2^{16} = 65536$ channels. The channel number ch corresponds to the energy of the detected particle. To improve the visualization of the spectrum, 2^6 channels are combined to one bin. So there are 1024 bins in total which will, from

¹Itech Instruments

now on be referred to as channels.

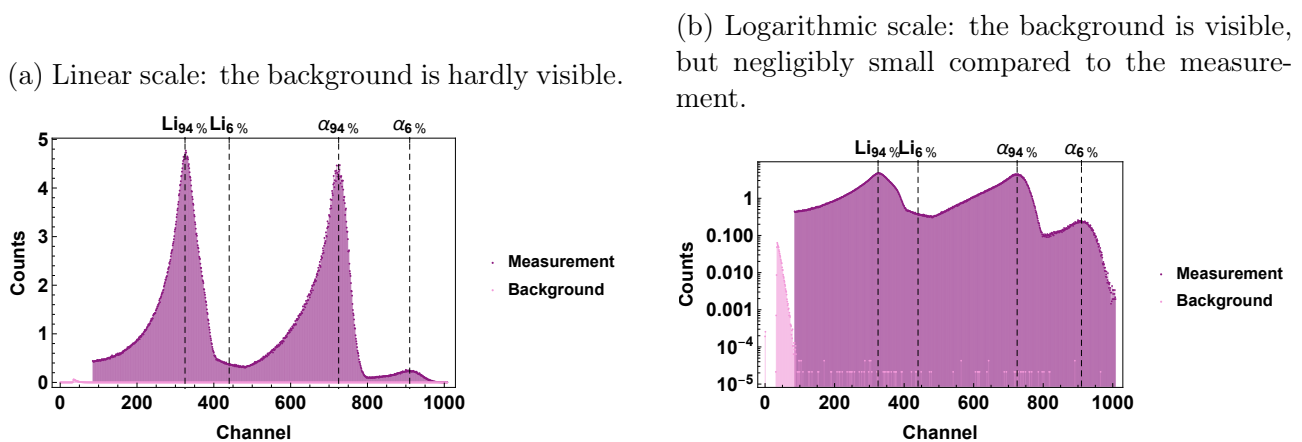
The detected particle is either a lithium or an alpha particle. These have different kinetic energies because of their different masses.

Due to the two possible decay channels (see equation 5.1) with different energies of the decay products, the typical neutron spectrum shows four peaks (where one is barely visible, see figure 5.2a):

The two peaks from the 94% decay channel for the ${}^7\text{Li}$ - and α -particle are approximately at $ch = 325$ and $ch = 725$ respectively. The peaks from the 6% decay channel are approximately at $ch = 440$ for ${}^7\text{Li}$ and $ch = 910$ for α .

The probability of one decay is much more likely than the other (94% vs. 6%). Therefore the intensity of the channel that results in particles from the 6%-decay is considerably lower. In fact the ${}^7\text{Li}$ -6% peak is totally hidden by the wings of the two 94% peaks.

Figure 5.2: Hist-file: Number of counts during a measurement (dark) / background measurement (light) vs. channel number. The measurements were normalized to a measurement time of 1 s.



Electronic background noise is mainly in the low-energy range of the spectrum (see figure 5.2b). It can be minimized by a suitable selection of the energy interval being considered - the 'region of interest' (ROI). In our case $\text{ROI} \in [100, 1023]$ applies [46].

5.1.2.3 List-File and rate over time

The list-file is a time-resolved record of the measurement. It contains the time t in $[\mu\text{s}]$, gate signals (Gate 1 and Gate 2), channel and time difference to the previous count Δt in $[\mu\text{s}]$ for each count.

The UCN beam from the turbine is shared between 3 experiments. This allows neutron measurements only in time share mode. In the time between the neutron measuring intervals the background is measured: A rotating shutter blocks the beamtube so that no neutron enters

the experiment. All counts in the detector, measured during that period, are considered as background (see also figure 5.2b).

In the transition period (time between neutron and background measurement and vice versa) the beamtube of the turbine is aligned to the selected experimental site. As soon as the beamtube is aligned, the experiment shutter opens. The transition period is chosen in a way that the measurement starts when the rate is stable.

Gate S2 is active during a neutron measurement. A measurement usually lasts 190 s. Gate S3 is active during a neutron measurement and in the transition periods. The transition period between background and neutron measurement is set to 12 s, the transition period between neutron and background measurement is 10 s.

Gate 1 in the list-file is the logically inverted Gate S2 signal. Gate 2 in the list file is Gate S3.

The list-file is generated in a specific binary format. 'Decode', a program written by Martin Thalhammer, is used to convert it into a comma-separated-values-file [30].

It has the form of a list with entries:

$$(t, \text{Gate 1}, \text{Gate 2}, \text{channel}, \Delta t) \quad (5.2)$$

To calculate the neutron count rate over time, the following steps are done:

1. **Selection of the measuring time:** During neutron measurement time, the gate signals are $(\text{Gate 1}, \text{Gate 2}) = (0, 1)$.
For the evaluation of the neutron count rate, only the measurement periods are of interest. Only rows, with gate signals $(0, 1)$ are selected.
2. **Binning:** A count rate R is defined by:

$$R = \frac{\#\text{counts}}{T}, \quad (5.3)$$

with $\#\text{counts}$ being the number of counts in a certain time intervall T .

In order to calculate the neutron count rate, the list 5.2 is binned, i.e. divided into sublists of length T . The binnings have a size of $T = 5$ s.

The timestamp of a bin is chosen to be the mean of the timestamp of the first count in the bin and the last:

$$\begin{aligned} \text{Bin}_i &= \{\text{count}(t_i), \dots, \text{count}(t_i + T)\}, \\ t(\text{Bin}_i) &= \frac{(2t_i + T)}{2}. \end{aligned} \quad (5.4)$$

It is assumed that $\#\text{counts}$ are approximately Poisson distributed. Therefore the error of the bin-count rate is calculated with:

$$\sigma_R = \sqrt{\frac{R}{T}}. \quad (5.5)$$

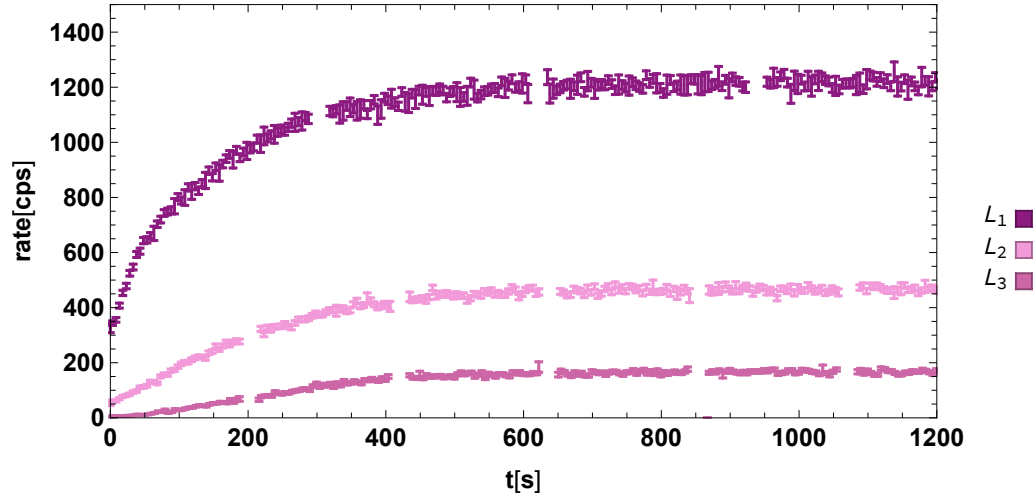
The result of this step is a list in the form of

$$(t, R, \sigma_R). \quad (5.6)$$

Figure 5.3 shows the rate over time values of the pumping (a) and venting (b) measurements for the three distances.

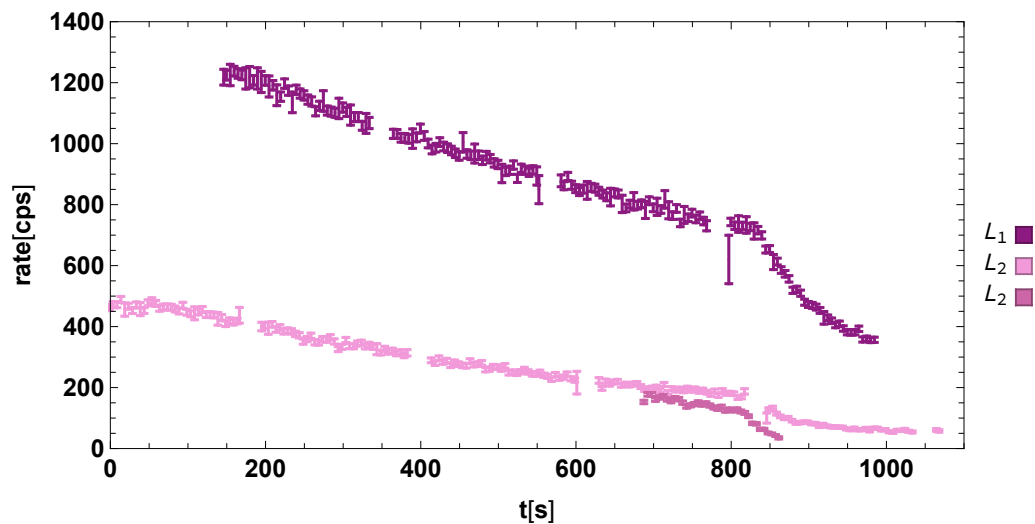
Figure 5.3: Neutron count rates for L_1 , L_2 and L_3 vs. time

(a) Pumping vacuum: the count rate increases while the pressure decreases. After some time, saturation occurs. The slope of the rate depends on the distance between the detector and the beamtube endpiece.



(b) Venting: the count rate decreases while the vacuum chamber is vented and the pressure increases. The edge indicates the time at which the large valve was opened (see also section 5.1.3.1).

Note that the measurement of L_3 was interrupted. The main shutter closed during that measurement. Consequently there are fewer data points, so the results of this measurement are less reliable. This measurement will not be considered for further calculations.



5.1.3 Pressure

5.1.3.1 Pumping and venting processes

The hardware of the *q*BOUNCE vacuum setup contains two pumps: a prevacuum pump² serving as backing pump for a turbomolecular pump³. The hardware components are industry-standard components and conform to ISO standards.

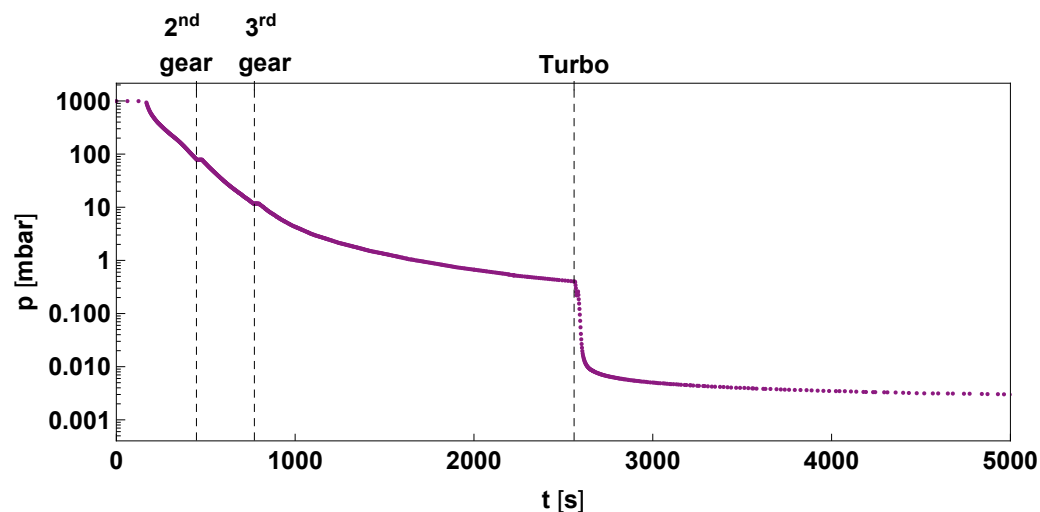
When evacuating the chamber ("pumping") the turbomolecular pump can be bypassed, as a turbomolecular pump is only suitable for very low pressures. In the pressure range $p > 0.5$ mbar the prevacuum pump evacuates. It has three gears and shifts up at $p \approx 100$ mbar and $p \approx 10$ mbar. At $p \approx 0.5$ mbar the bypass is closed and the main turbomolecular pump valve opens. This causes the pressure to drop abruptly. At $p \approx 0.001$ mbar the process saturates and the pressure remains more or less constant (see figure 5.4a) [47].

When venting, a needle valve is opened first. Air slowly enters the chamber and the pressure rises. At $p \approx 100$ mbar the big valve is opened (see figure 5.4b).

Figure 5.4: Pumping and venting vs. time

(a) Pumping vacuum: When the vacuum pump starts pumping, the pressure begins to drop approximately exponential.

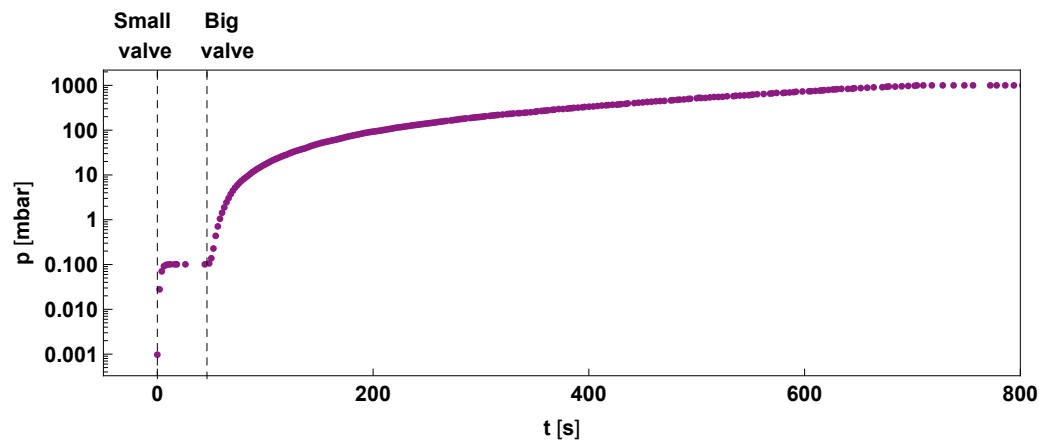
The small steps (at ≈ 450 s and ≈ 770 s) indicate that the vacuum pump switches to the second and third gear. The big step at ≈ 2560 s is due to the turbomolecular pump switching on.



²Edwards iXL 120

³Pfeiffer Vacuum TMU 521 P

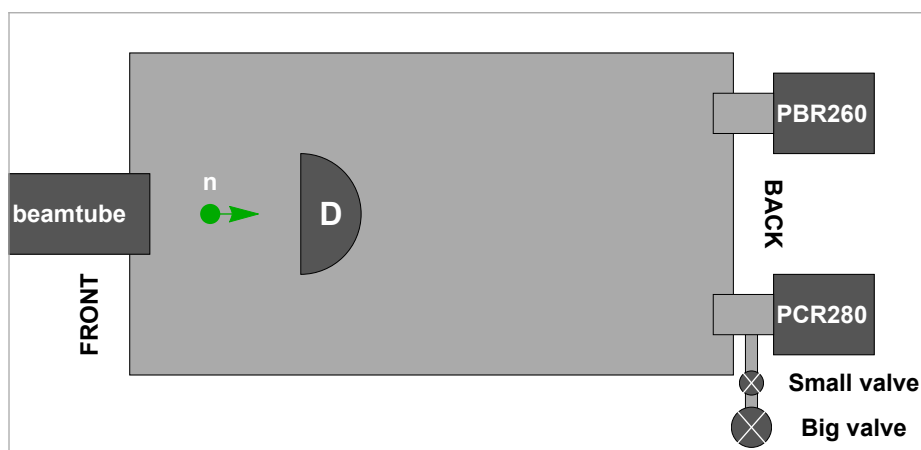
(b) Venting the vacuum chamber: When the small valve is opened, the pressure increases approximately linearly and saturates eventually. The edge (at ≈ 46 s) indicates the opening of the big valve.



5.1.3.2 Vacuum sensors

There are two vacuum sensors, PCR280 and PBR260⁴, placed on the backside of the vacuum chamber. PCR280 is placed on the same side as the valves, PBR260 is placed on the opposite side (see figure 5.5).

Figure 5.5: Schematic sketch of the vacuum chamber, the valves and the placement of the vacuum sensors.



The accuracies of PCR280 and PBR260 can be taken from table 5.1.

⁴Pfeiffer

Table 5.1: Accuracies of the vacuum sensors PCR280 and PBR260 for different pressure ranges [48, 49]

Sensor	pressure range	Accuracy
PCR280	[100, 950] mbar	$\pm 5\%$
	$[10^{-3}, 100]$ mbar	$\pm 15\%$
	$[5 \times 10^{-4}, 10^{-3}]$ mbar	$\pm 50\%$
PBR260	$[10^{-8}, 10^{-2}]$ mbar	$\pm 15\%$

The file, created during a pressure-measurement, is a list in the form of

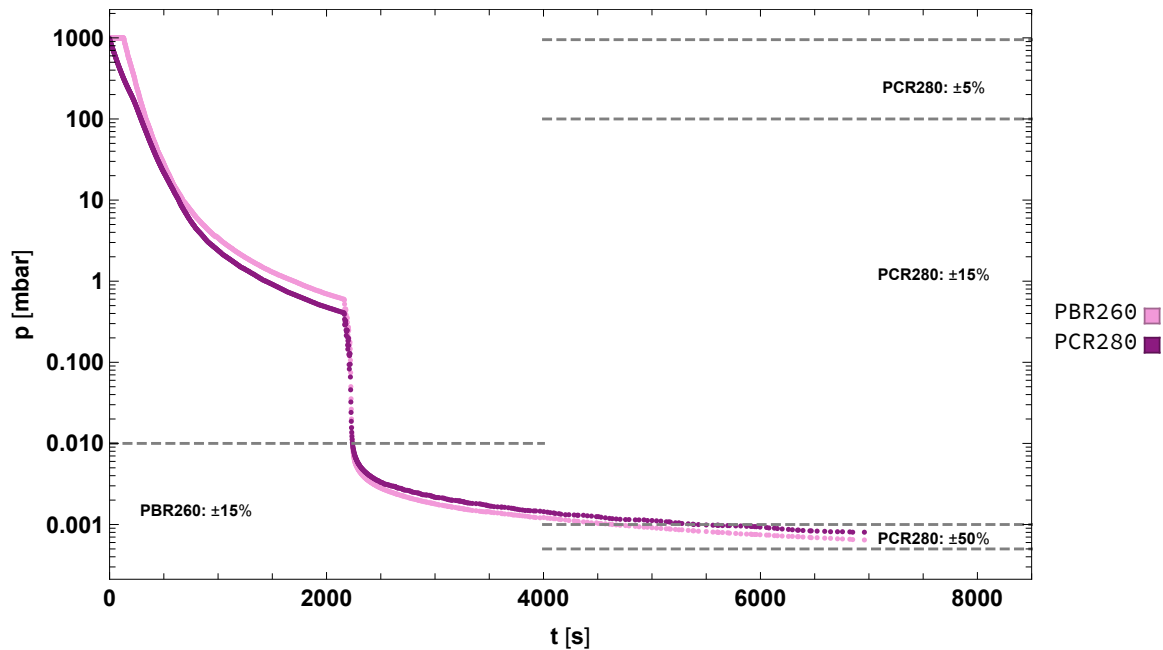
$$(t, p_{\text{PCR280}}, p_{\text{PBR260}}) . \quad (5.7)$$

Depending on the pressure range, the measurement error is calculated with the accuracy taken from table 5.1.

Figure 5.6 shows a comparison of the pressure curves recorded by PCR280 and PBR260. These do not match due to different positioning of the two vacuum sensors (see figure 5.5): they measure the pressure at their point of position and not the pressure in the chamber (which is not totally homogeneous due to the position of the pumps and the valves). Another reason for the mismatching pressure curves are the different sensitivities in different pressure ranges.

Figure 5.6: Comparison of the pressure records of the two vacuum sensors PCR280 and PBR260 and the their accuracies in different pressure ranges. This example was recorded while pumping vacuum.

The fast drop at $t \approx 2200$ s is caused by the turbo pump switching on.



For this measurement, only pressures in the range of [0.01, 1000] mbar are relevant, so only the measurement values from PCR280 will be considered.

5.1.4 Rate over pressure

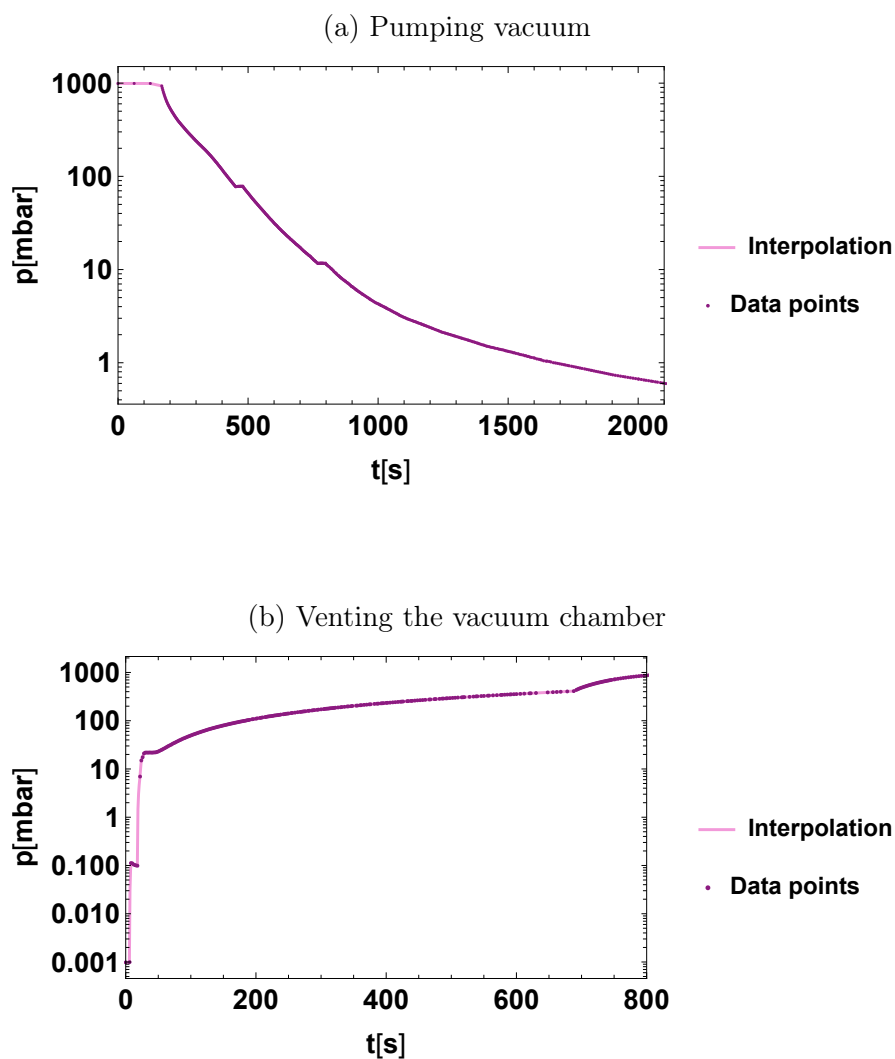
5.1.4.1 Interpolation of pressure curves

The goal is to map the rate to the pressure:

$$(t_R, R, \sigma_R) \ \& \ (t_p, p, \sigma_p) \xrightarrow{t_R=t_p} (p, R, \sigma_p, \sigma_R) . \quad (5.8)$$

First the discrete pressure over time values are interpolated (using the *Interpolation*-function of *Mathematica*, interpolation order 1 was chosen, meaning that the interpolation was linear). Figure 5.7 shows an example for interpolated pressure curves.

Figure 5.7: Interpolation and data points of a measurement row



5.1.4.2 Time offset between detector- and pressure data

InterWinner is running on the measurement server 'Neron'. The time information of the detector data consequently is in 'Neron-time'. The pressure data recording runs on the 'NAS'-server, with the time-information in 'NAS-time'.

The time offset between the 'Neron-time' and the 'NAS-time' of $\Delta t_{\text{NAS-Neron}} = t_{\text{NAS}} - t_{\text{Neron}} \approx$

748 s was taken into account.

In addition to the constant server time offset $\Delta t_{\text{NAS-Neron}}$, the different starting points of the detector and the pressure measurement have to be considered: The vacuum sensors log continuously, whereas the detector is started manually. Therefore the measurement starts are not necessarily simultaneous.

This time difference has to be considered manually for each measurement, by comparing the starting times with $\Delta t_{\text{NAS-Neron}}$ added to the detector-starting time (see appendix C.1).

5.1.4.3 Results and fits

The interpolated pressure curve $p(t)$ and the rate-time-list (t_R, R, σ_R) can be combined to a rate-pressure-list:

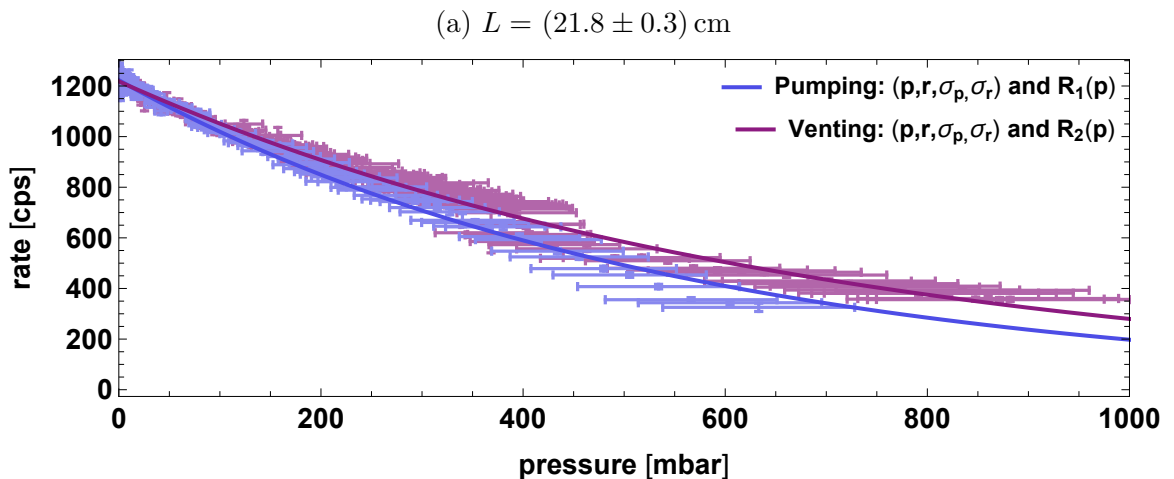
$$(p(t_R), R(t_R), \sigma_p(t_R), \sigma_R(t_R)) . \quad (5.9)$$

The results of mapping the rate to the pressure and the corresponding fits $R_1(p) - R_5(p)$ are shown in figure 5.8.

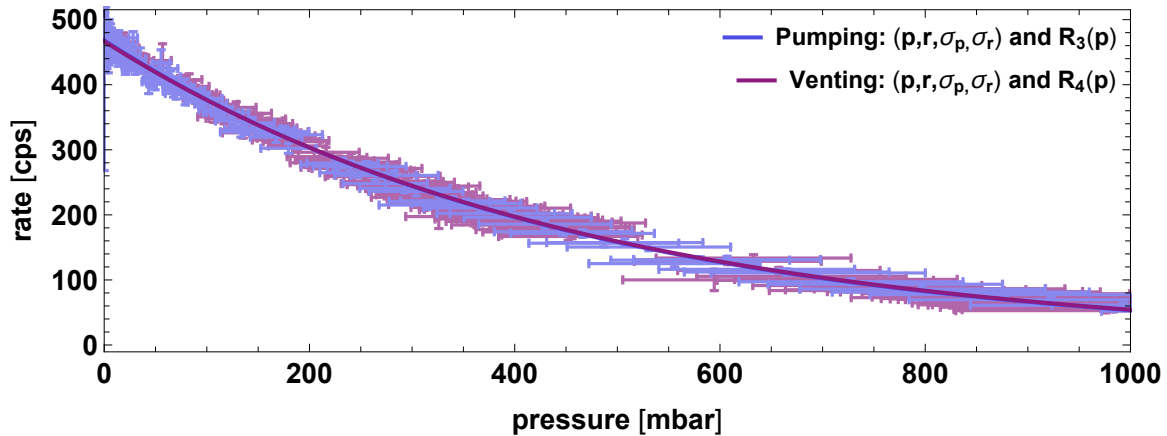
Fitting the data points (see appendix B.3) leads to the following functions:

$$\begin{aligned} R_1(p) &= (1223.09 \pm 0.57) e^{-(0.00182301 \pm 0.000009)p} , \\ R_2(p) &= (1218.25 \pm 2.49) e^{-(0.00147172 \pm 0.000007)p} , \\ R_3(p) &= (468.128 \pm 0.31) e^{-(0.00217035 \pm 0.000001)p} , \\ R_4(p) &= (466.67 \pm 1.35) e^{-(0.00215173 \pm 0.000010)p} , \\ R_5(p) &= (168.805 \pm 0.21) e^{-(0.00427313 \pm 0.000003)p} . \end{aligned} \quad (5.10)$$

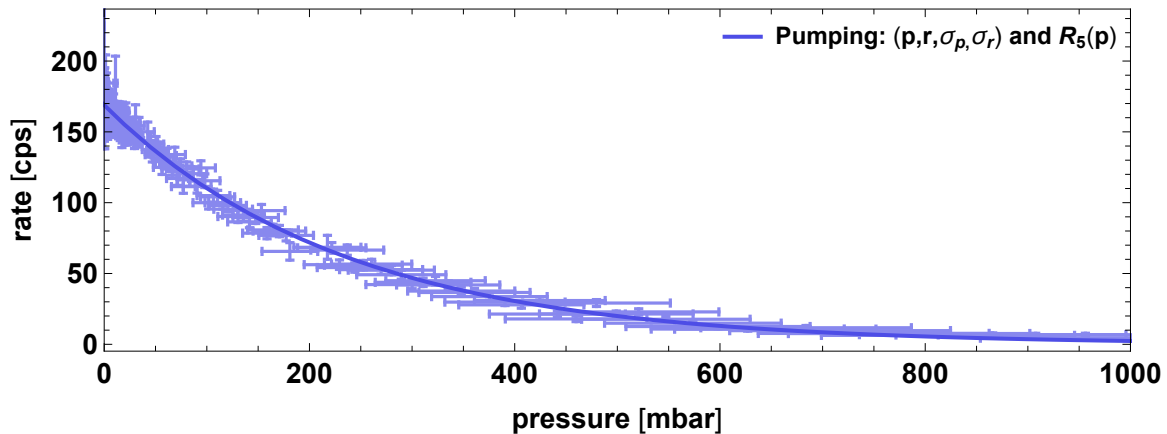
Figure 5.8: Rate vs. pressure: mapped data points $(p, R, \sigma_p, \sigma_r)$ and fits $R_1(p) - R_5(p)$. Pumping and venting for $L = (21.8 \pm 0.3)$ cm (a), $L = (36.8 \pm 0.3)$ cm (b) and $L = (67.9 \pm 0.3)$ cm (c)



(b) $L = (36.8 \pm 0.3)$ cm: Pumping and venting measurement show approximately the same rate-vs.-pressure behavior



(c) $L = (67.9 \pm 0.3)$ cm: As mentioned above, the pumping measurement of this measurement row is not reliable. Only the pumping measurement is taken into account



5.2 Interpretation of the measurements

The transmission law describes the attenuation of the neutron count rate during the passage of an absorbing medium (in our case air):

$$R = R_0 e^{-n\Sigma l} , \quad (5.11)$$

with R_0 being the neutron count rate without absorption, n the particle density of air, Σ the total neutron cross section of air and l the path of the neutron through the medium [50].

The Ideal-gas law connects pressure p and particle density n :

$$n = \frac{p}{k_B T} , \quad (5.12)$$

with $k_B = (1.380\,648\,520\,0 \pm 0.000\,000\,007\,9) \times 10^{-23}$ J K⁻¹ being the Boltzmann constant [13] and $T_1 = (296.85 \pm 1.00)$ K, $T_2 = (296.35 \pm 1.00)$ K and $T_3 = (296.35 \pm 1.00)$ K being the temperature (the temperature is logged next to the chamber, $T_1 - T_3$ are the measured temperatures for the three measurement rows).

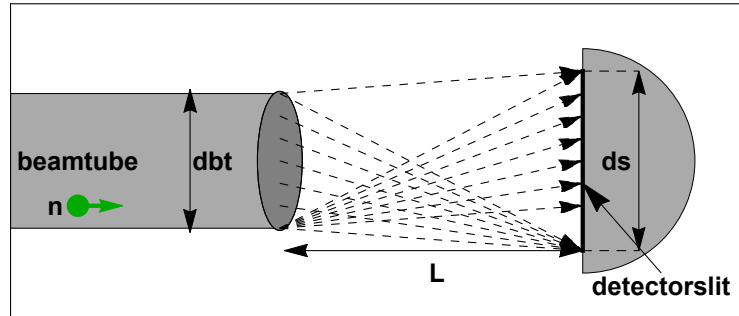
l is the mean free path of the neutron. It is calculated with the distance between detector and beamtube endpiece $L_1 = (0.218 \pm 0.003)$ m, $L_2 = (0.368 \pm 0.003)$ m and $L_3 = (0.679 \pm 0.003)$ m, the width of the detector slit $ds = 0.1$ m and the diameter of the beamtube $dbt = 0.08$ m (see figure 5.9):

$$l = \frac{1}{ds \, dbt} \int_{-\frac{dbt}{2}}^{\frac{dbt}{2}} \int_{-\frac{ds}{2}}^{\frac{ds}{2}} \sqrt{L^2 + (y - x)^2} \, dx \, dy, \quad (5.13)$$

resulting in $l_1 = (0.2209 \pm 0.0296)$ m, $l_2 = (0.3693 \pm 0.0495)$ m and $l_3 = (0.6800 \pm 0.0911)$ m.

It is assumed that all paths are equally probable. This is only approximative, since the neutrons are locally distributed non-constantly. But as the difference between L and l is very small, the error of this approximation is negligible.

Figure 5.9: Illustration of the different neutron paths



R_0 corresponds to the neutron count rate at $p = 0$. It is taken from the fits to the rate-vs.-pressure-fits (see equation 5.10), leading to $R_{0,1} = (1223.09 \pm 0.57)$ cps, $R_{0,2} = (1218.25 \pm 2.49)$ cps, $R_{0,3} = (468.128 \pm 0.310)$ cps, $R_{0,4} = (466.67 \pm 1.35)$ cps and $R_{0,5} = (168.805 \pm 0.210)$ cps.

5.2.1 The mean velocity of UCNS

The first interpretation of the results for $R(p)$ is the calculation of the mean neutron velocity. For this purpose, the neutron cross section is taken as given and the literature values are used.

5.2.1.1 The cross section of air for UCNS and its relation to the UCN velocity

Air is a mixture of several types of molecules. Dry air contains (by volume) 78.084% of N_2 , 20.946% of O_2 , 0.93% of Ar and 0.036% of CO_2 and negligible amounts of other gases [51].

The relative humidity H was recorded before every measurement-row: $H_1 = 52\%$, $H_2 = 55\%$ and $H_3 = 55\%$.

The relative humidity is defined by the ratio of the partial pressure of water vapor in air p_p to the equilibrium vapor pressure of water p_e :

$$H = \frac{p_p}{p_e}. \quad (5.14)$$

The equilibrium vapor pressure of water p_e can be calculated with the Magnus equation [52]

$$p_e = 610.94 e^{\frac{17.62 (T-273.15)}{T-30.03}} , \quad (5.15)$$

leading to $p_{e,1} = 2924.83$ Pa, $p_{e,2} = 2837.93$ Pa and $p_{e,3} = 2837.93$ Pa.

With equation 5.14 and 5.15, the partial pressure of water vapor p_p can be calculated: $p_{p,1} = 1520.91$ Pa, $p_{p,2} = 1560.86$ Pa and $p_{p,3} = 1560.86$ Pa.

Inserting p_p into equation 5.12 leads to the particle density of H₂O in air, dependent on the relative humidity and the temperature:

$$n_{\text{H}_2\text{O}} = \frac{p_p}{k_B T} = 3.71 \times 10^{23} \text{ m}^{-3}, 3.81 \times 10^{23} \text{ m}^{-3}, 3.81 \times 10^{23} \text{ m}^{-3} . \quad (5.16)$$

The particle density of dry air is calculated in accordance with equation 5.16:

$$n_{\text{dry air}} = \frac{(p_{\text{air}} - p_p)}{k_B T} = 2.42 \times 10^{25} \text{ m}^{-3}, 2.41 \times 10^{25} \text{ m}^{-3}, 2.41 \times 10^{25} \text{ m}^{-3} , \quad (5.17)$$

with $p_{\text{air},1} = 100\,760$ Pa, $p_{\text{air},2} = 100\,350$ Pa and $p_{\text{air},3} = 100\,350$ Pa being the air pressure recorded before every measurement-row.

The relative proportion of H₂O in air is

$$n_{\text{rel,H}_2\text{O}} = \frac{n_{\text{H}_2\text{O}}}{n_{\text{dry air}}} = 1.53\%, 1.58\%, 1.58\% . \quad (5.18)$$

Leading to the relative proportions of the other air components:

$$\begin{aligned} n_{\text{rel,N}_2} &= 76.89\%, 76.85\%, 76.85\% , \\ n_{\text{rel,O}_2} &= 20.63\%, 20.62\%, 20.62\% , \\ n_{\text{rel,Ar}} &= 0.92\%, 0.92\%, 0.92\% , \\ n_{\text{rel,CO}_2} &= 0.04\%, 0.04\%, 0.04\% . \end{aligned} \quad (5.19)$$

The cross section of air is calculated via the cross sections of the molecules multiplied by the relative proportion of the molecule. The cross sections of the molecules is calculated as the sum of cross sections of the corresponding elements divided by the number of particles forming the molecule (e.g.: $\Sigma_{\text{H}_2\text{O}} = \frac{1}{3}(\Sigma_{\text{H}} + 2\Sigma_{\text{O}})$).

Cross sections are given in the unit barn: $1 \text{ b} = 10^{-28} \text{ m}^2$. This must be taken into account in further calculations.

The elementary cross sections refer to thermal neutrons with $v_{th} = 2200 \text{ m s}^{-1}$ and are taken from [44]. They are

$$\begin{aligned} \Sigma_{\text{N}} &= 13.41 \text{ b} , \\ \Sigma_{\text{O}} &= 4.23 \text{ b} , \\ \Sigma_{\text{Ar}} &= 1.36 \text{ b} , \\ \Sigma_{\text{C}} &= 5.55 \text{ b} , \\ \Sigma_{\text{H}} &= 82.35 \text{ b} . \end{aligned} \quad (5.20)$$

Leading to the molecular cross sections:

$$\begin{aligned}
 \Sigma_{\text{N}_2} &= 13.41 \text{ b} , \\
 \Sigma_{\text{O}_2} &= 4.23 \text{ b} , \\
 \Sigma_{\text{Ar}} &= 1.36 \text{ b} , \\
 \Sigma_{\text{CO}_2} &= 4.67 \text{ b} , \\
 \Sigma_{\text{H}_2\text{O}} &= 56.31 \text{ b} .
 \end{aligned}
 \tag{5.21}$$

With equation 5.19 and 5.21, the cross section of air for thermal neutrons is

$$\begin{aligned}
 \Sigma_{\text{air}} &= \sum_i p_i \Sigma_i = 12.06 \text{ b}, 12.08 \text{ b}, 12.08 \text{ b} , \\
 i &= \{\text{N}_2, \text{O}_2, \text{Ar}, \text{CO}_2, \text{H}_2\text{O}\} .
 \end{aligned}
 \tag{5.22}$$

The probability of an interaction between neutron and nucleus is proportional to the time the neutron is near the nucleus. Leading to an indirect proportionality of Σ and v :

$$\Sigma(v) = \frac{1}{v} \Sigma .
 \tag{5.23}$$

The cross section value for thermal neutrons can therefore be scaled to any velocity, with

$$\Sigma(v) = \frac{v_{th}}{v} \Sigma(v_{th}) .
 \tag{5.24}$$

This establishes a connection between the value of the neutron cross section at a fixed velocity and the velocity of the neutron.

5.2.1.2 Calculation of the mean UCN velocity

During the measurement a large number of neutrons were observed. Therefore, no statement can be made about the velocity of a single particle.

The velocities of the UCNs follow a certain distribution $\rho(v)$ (see also section 4.1). The mean velocity is the expected value of the velocity distribution and is calculated with:

$$\bar{v} = \langle v \rangle = \int_{-\infty}^{\infty} v \rho(v) dv .
 \tag{5.25}$$

With equations 5.12, 5.13 and 5.24, the rate is a function of the velocity

$$R(v) = R_0 e^{-\frac{pl}{k_B T} \frac{v_{th}}{v} \Sigma(v_{th})} := R_0 e^{\frac{\alpha}{v}} ,
 \tag{5.26}$$

and is therefore distributed accordingly. The mean rate, which is the result of the measurement, is calculated with:

$$\bar{R} = \int_{-\infty}^{\infty} R(v) \rho(v) dv .
 \tag{5.27}$$

Expanding $R(v)$ at $v = \bar{v}$ gives:

$$R(v) = \sum_{n=0}^{\infty} R^{(n)}(\bar{v}) \frac{(v - \bar{v})^n}{n!}, \quad (5.28)$$

with $R^{(n)}(\bar{v}) = \frac{d^n R(v)}{dv^n} \Big|_{v=\bar{v}}$ being the n th derivative of R at $v = \bar{v}$.

With 5.26, $R^{(n)}(\bar{v})$ is

$$R^{(n)}(\bar{v}) = (-1)^n \sum_{j=1}^n \frac{\prod_{i=1}^{n-1} \binom{i}{1} \binom{n}{j}}{(j-1)!} \frac{\alpha^j}{\bar{v}^{j+n}} R(\bar{v}). \quad (5.29)$$

5.27, 5.28 and 5.29 lead to

$$\bar{R} = \sum_{n=0}^{\infty} \frac{(-1)^n}{n!} \sum_{j=1}^n \frac{\prod_{i=1}^{n-1} \binom{i}{1} \binom{n}{j}}{(j-1)!} \frac{\alpha^j}{\bar{v}^{j+n}} R(\bar{v}) \underbrace{\int_{-\infty}^{\infty} (v - \bar{v})^n \rho(v) dv}_{:=\mu_n}. \quad (5.30)$$

μ_n is the n th central moment (see also section 4.1).

$\alpha = -\frac{pl}{k_B T} v_{th} \Sigma(v_{th})$ is in the range of $[-4.4 \times 10^{-5}, -44.4]$ (for $p \in [10^{-1} \text{ Pa}, 100760 \text{ Pa}]$).

To estimate the order of magnitude of the terms in 5.30, $\bar{v} = 10 \text{ m s}^{-1}$ is assumed.

Calculating the first non-zero terms of 5.30 and inserting the maximum absolute value of α , $\alpha_{max} = -44.4$ and \bar{v} gives

$$\bar{R} = R(\bar{v}) \left(1 + \underbrace{\left(\frac{\alpha}{\bar{v}^3} + \frac{\alpha^2}{2\bar{v}^4} \right)}_{\leq 0.445} \mu_2 - \underbrace{\left(\frac{\alpha}{\bar{v}^4} + \frac{\alpha^2}{\bar{v}^5} + \frac{\alpha^3}{6\bar{v}^6} \right)}_{\leq 0.055} \mu_3 + \right. \\ \left. \underbrace{\left(\frac{\alpha}{\bar{v}^5} + \frac{3\alpha^2}{2\bar{v}^6} + \frac{\alpha^3}{2\bar{v}^7} + \frac{\alpha^4}{24\bar{v}^8} \right)}_{\leq 6.6 \times 10^{-4}} \mu_4 - \dots \right). \quad (5.31)$$

The central moments of the velocity distribution of the neutrons in the beamtube and in the vacuum chamber (TOF- and aperture spectrum, respectively) were already estimated in section 4.1. With the central moments of the aperture spectrum $R(\bar{v}) \approx 1.000145$ applies. Therefore

$$R(\bar{v}) \approx \bar{R} \quad (5.32)$$

can be assumed in good approximation.

In order to determine the mean neutron velocity \bar{v} , equation 5.26 is transformed to

$$\bar{v} = -\frac{p l}{\ln\left(\frac{R}{R_0}\right) k_B T} v_{th} \Sigma(v_{th}) . \quad (5.33)$$

$R = R(\bar{v})$ enters into this expression of v . However, the measured quantity is \bar{R} . Equation 5.32 shows that the difference is negligible.

\bar{v} is an indirect measurement quantity. It depends on p , l , R , R_0 and T . The error for \bar{v} is calculated with an error propagation:

$$\sigma_{\bar{v}} = \sqrt{\sum_i \left(\frac{\partial v}{\partial x_i} \sigma_{x_i} \right)^2} , \quad (5.34)$$

$$x_i = \{p, l, R, R_0, T\} ,$$

with σ_{x_i} being the error of the corresponding measurement quantity.

For σ_p and σ_R see table 5.1 and equation 5.5 respectively, $\sigma_l := 3$ mm. σ_{R_0} corresponds to the error of the fit (see equation 5.10 and appendix B.3): $\sigma_{R_0,1} = 0.57$ cps, $\sigma_{R_0,2} = 2.49$ cps, $\sigma_{R_0,3} = 0.31$ cps, $\sigma_{R_0,4} = 1.35$ cps and $\sigma_{R_0,5} = 0.21$ cps and $\sigma_T = 1$ K.

Inserting the data points p and R from equation 5.9 into 5.33 results in a list in the form of

$$(p, \bar{v}(p, R), \sigma_p, \sigma_{\bar{v}}) . \quad (5.35)$$

Fitting the data (see appendix B.4) leads to the following results:

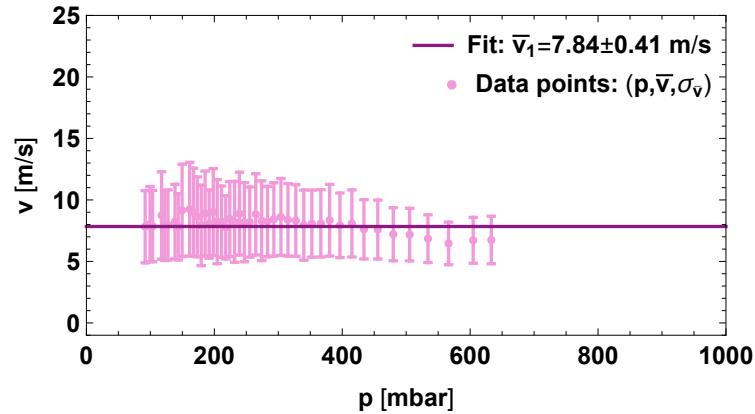
$$\begin{aligned} \bar{v}_1 &= (7.84 \pm 0.41) \text{ m s}^{-1} , \\ \bar{v}_2 &= (9.53 \pm 0.23) \text{ m s}^{-1} , \\ \bar{v}_3 &= (10.61 \pm 0.63) \text{ m s}^{-1} , \\ \bar{v}_4 &= (10.90 \pm 0.27) \text{ m s}^{-1} , \\ \bar{v}_5 &= (10.01 \pm 0.56) \text{ m s}^{-1} . \end{aligned} \quad (5.36)$$

Figure 5.10 shows the transformed lists $(p, R) \rightarrow (p, \bar{v}(R, p))$ and the corresponding fits.

Figure 5.10: Neutron mean velocity vs. pressure. The error bars in p -direction show σ_p , the error bars in Σ direction show σ_Σ .

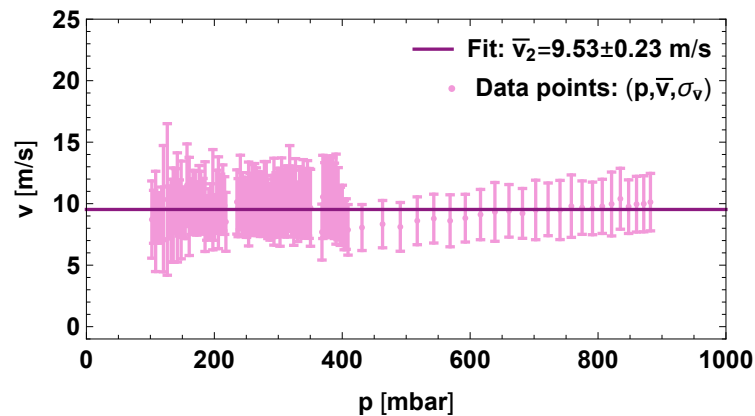
(a) Pumping, $L = (21.8 \pm 0.3)$ cm.

There is a continuous drop in \bar{v} at $p \gtrsim 400$ mbar.



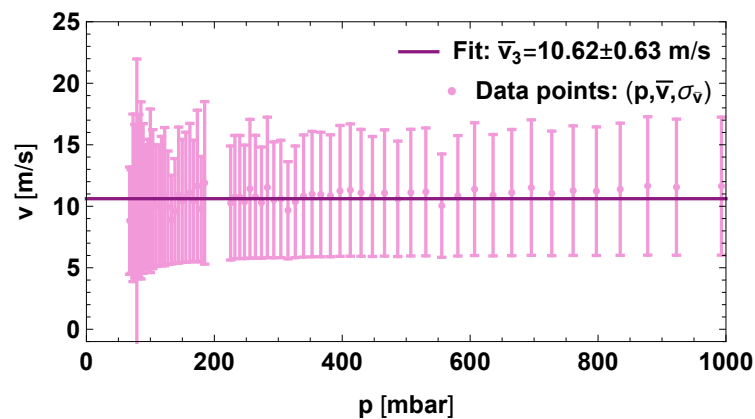
(b) Venting, $L = (21.8 \pm 0.3)$ cm.

There also is a drop in \bar{v} at $p \gtrsim 400$ mbar. This drop is more abruptly than the one in (a).



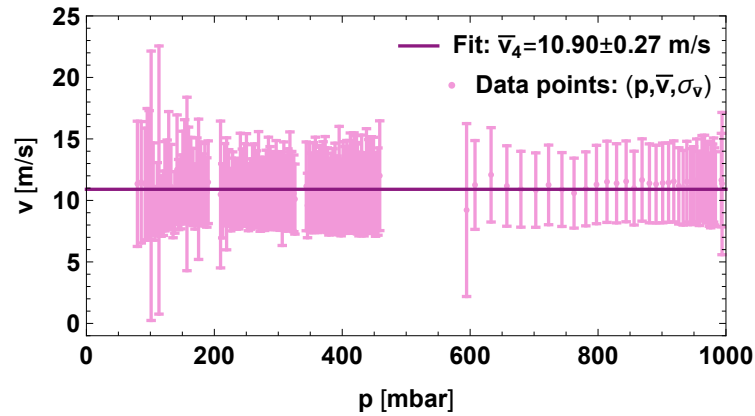
(c) Pumping, $L = (36.8 \pm 0.3)$ cm.

The course of \bar{v} is approximately constant.



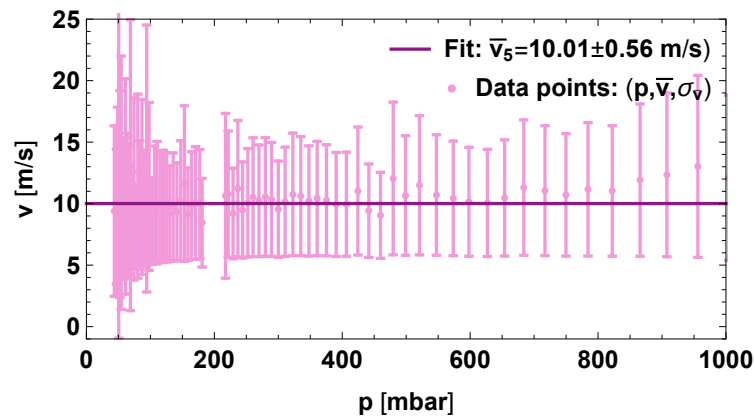
(d) Venting, $L = (36.8 \pm 0.3)$ cm.

The measurement was briefly interrupted. Between 400 mbar and 600 mbar there are no data points.



(e) Pumping, $L = (67.9 \pm 0.3)$ cm.

Above $p \approx 600$ mbar, \bar{v} increases a little.



In order to get a final value for \bar{v} , a fit to the aggregated data points of the measurements is done (see appendix B.4), resulting in:

$$\bar{v}_{1-5} = (9.83 \pm 0.15) \text{ m s}^{-1} . \quad (5.37)$$

In figure 5.14, the data points of measurement 1-5 and the corresponding fit \bar{v}_{1-5} is shown.

Figure 5.11: Neutron mean velocity vs. pressure. Data points from measurement 1-5 and fit.

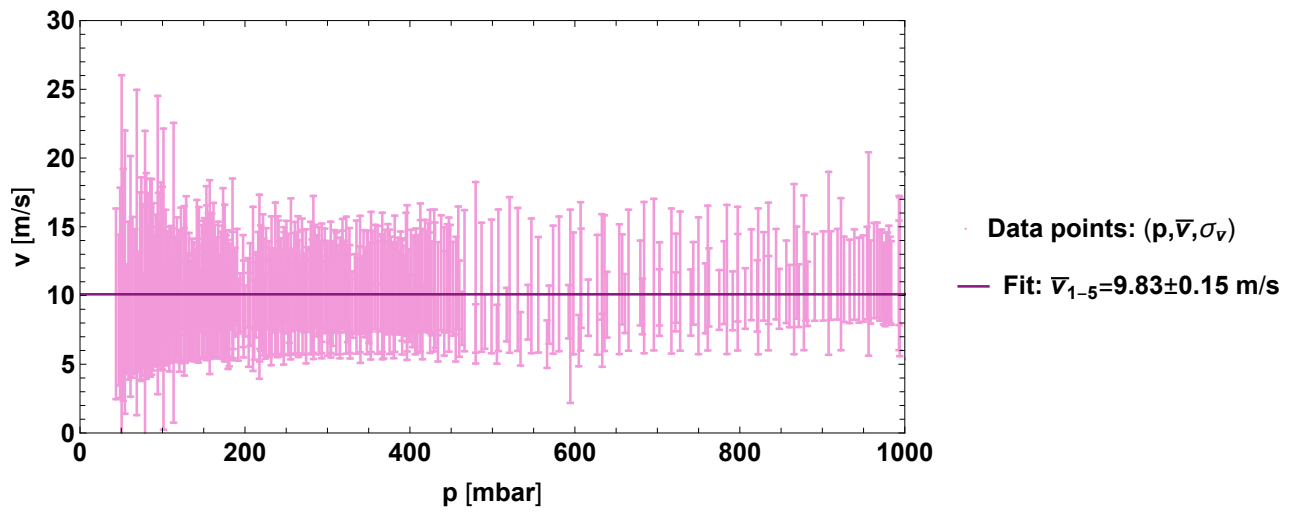
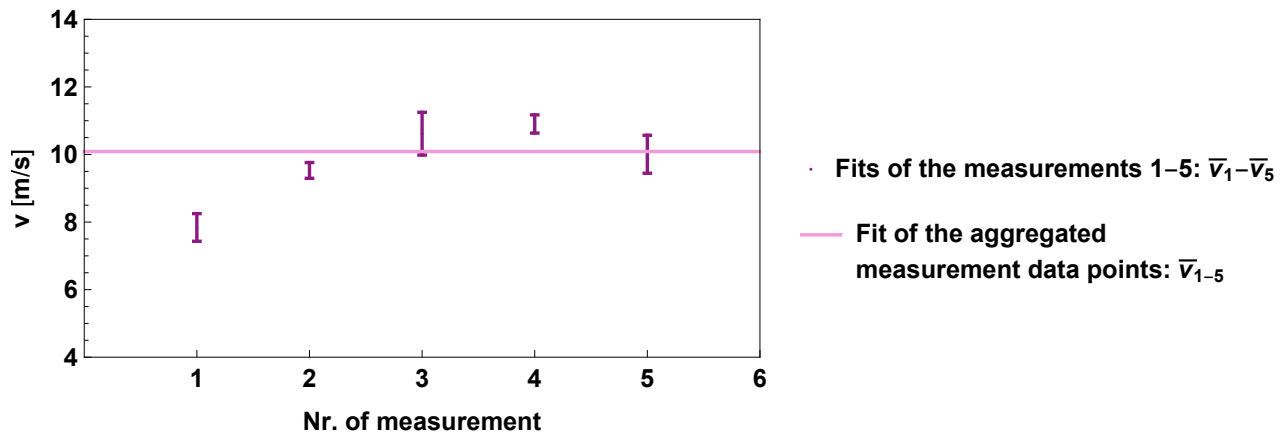


Figure 5.15 shows the fit-results given in 5.41 and the fit of all data points of measurement 1-5 given in 5.37.

Figure 5.12: Comparison of the fit-results for the neutron mean velocity of the different measurements.



5.2.2 The cross section of air for UCNs

The second interpretation of the results for $R(p)$ is the calculation of the UCN cross section of air.

With equation 5.11 and 5.12, Σ can be written as

$$\Sigma = -\frac{p}{lk_B T} \ln \left(\frac{R}{R_0} \right) . \quad (5.38)$$

l , T and R_0 remain unchanged with respect to the previous section.

Inserting the list of rate-vs.-pressure data points given in equation 5.9, leads to a list of the form

$$(p(t_R), \Sigma(t_R), \sigma_p(t_R), \sigma_\Sigma(t_R)) . \quad (5.39)$$

The error of Σ , σ_Σ is obtained via an error propagation:

$$\sigma_\Sigma = \sqrt{\sum_i \left(\frac{\partial \Sigma}{\partial x_i} \sigma_{x_i} \right)^2}, \quad (5.40)$$

$$x_i = \{p, l, R, R_0, T\},$$

with σ_p , σ_l , σ_R , σ_{R_0} , and σ_T given in section 5.2.1.2.

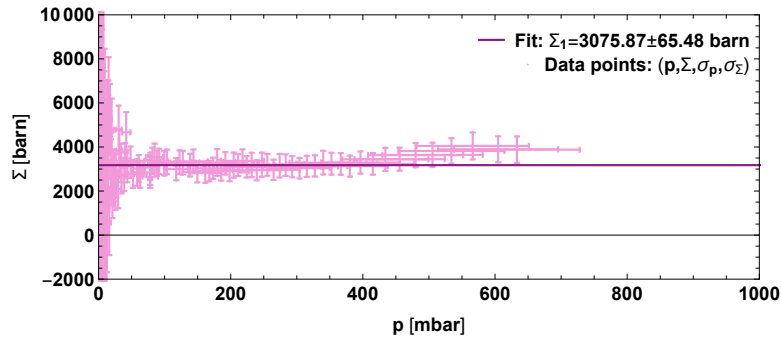
Fitting the data (see appendix B.5) leads to the following results:

$$\begin{aligned} \Sigma_1 &= (3175.50 \pm 65.48) \text{ b}, \\ \Sigma_2 &= (2699.36 \pm 38.50) \text{ b}, \\ \Sigma_3 &= (2429.15 \pm 45.82) \text{ b}, \\ \Sigma_4 &= (2371.06 \pm 30.06) \text{ b}, \\ \Sigma_5 &= (2518.95 \pm 47.79) \text{ b}. \end{aligned} \quad (5.41)$$

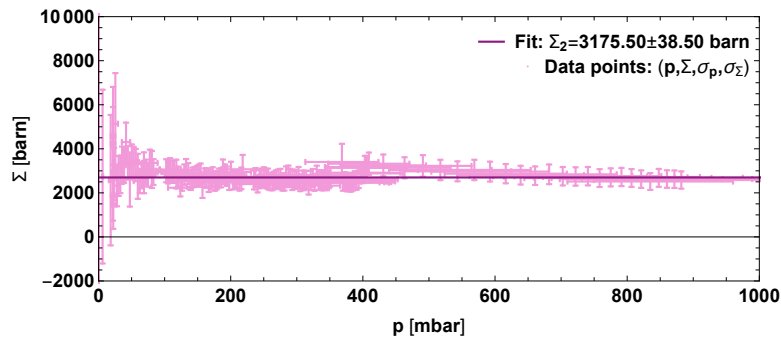
Figure 5.13 shows the transformed lists $(p, R) \rightarrow (p, \Sigma(R, p))$ and the corresponding fits.

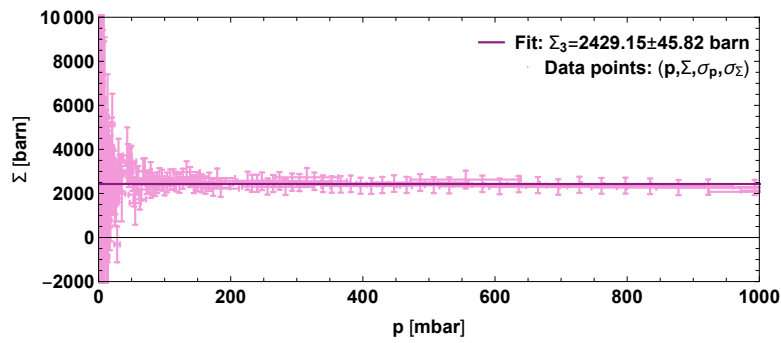
Figure 5.13: Cross section of air for UCNS vs. pressure. The data points for low pressure $p < 30$ mbar are very unsteady. This is due to the values of R_0 resulting from a fit and not being exact. $\ln\left(\frac{R}{R_0}\right)$ is a factor in the expression for Σ . Therefore Σ can get very large in the case of $R_0 > R$.

- (a) Pumping, $L = 21.78$ cm.
 Σ increases noticeably at $p \gtrsim 400$ mbar.

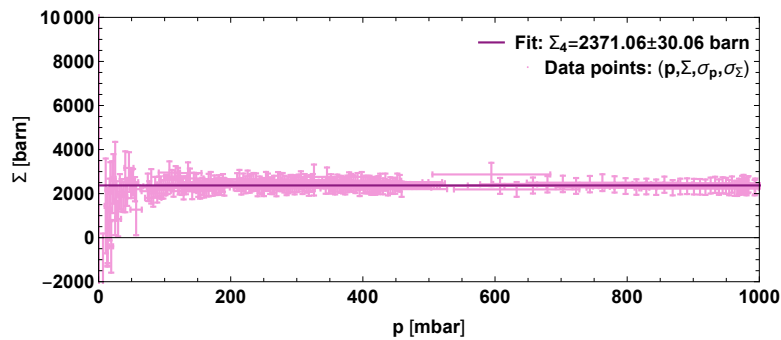
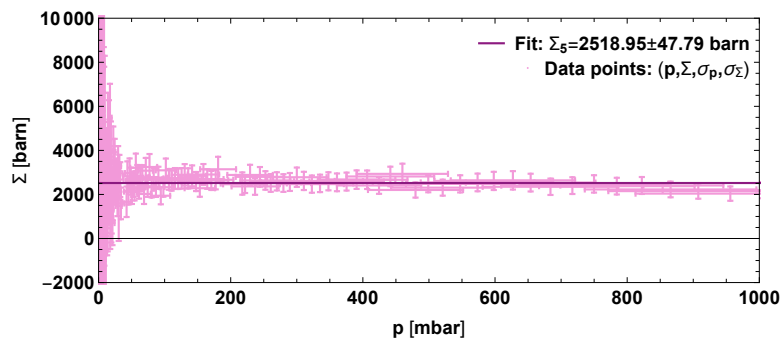


- (b) Venting, $L = 21.78$ cm.
 Σ decreases approximately linear at $p \gtrsim 400$ mbar.



(c) Pumping, $L = 36.75$ cm.(d) Venting, $L = 36.75$ cm.

There was a short interruption of the measurement. Between 500 mbar and 600 mbar no data points were recorded.

(e) Pumping, $L = 67.90$ cm.

To compare the results and to get a final value for Σ , the data points were combined and fitted (see also appendix B.5). The fit results in

$$\Sigma_{1-5} = (2542.27 \pm 18.48) \text{ b} . \quad (5.42)$$

With equation 5.24 and $v = \hat{v}_{\text{TOF}}$ (a), $v = \hat{v}_{\text{AP}}$ (b) and $v = \bar{v}_{1-5}$ (see equation 5.37) (c) the expected value for Σ is:

$$\Sigma(\hat{v}_{\text{TOF}}) = (3286.11 \pm 3.96) \text{ b} \quad (5.43a)$$

$$\Sigma(\hat{v}_{\text{AP}}) = (2722.01 \pm 16.73) \text{ b} \quad (5.43b)$$

$$\Sigma(\bar{v}_{1-5}) = (2703.56 \pm 41.25) \text{ b} \quad (5.43c)$$

The cross section calculated from the fitted mean neutron velocity v_{1-5} matches the fitted cross section Σ_{1-5} most closely. The values lie within the error and therefore represent consistent measurement results.

Figure 5.14: Cross section of air for UCNs vs. pressure. The data points from measurement 1-5 were aggregated and fitted. The fit is compared to the cross sections which calculate from equation 5.24 and $v = \hat{v}_{\text{TOF}}$, $v = \hat{v}_{\text{AP}}$ and $v = \bar{v}_{1-5}$

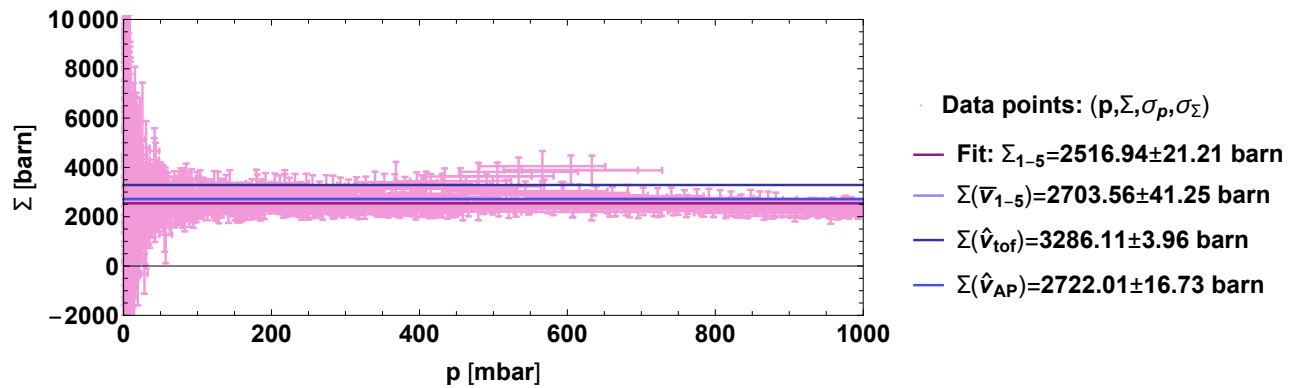
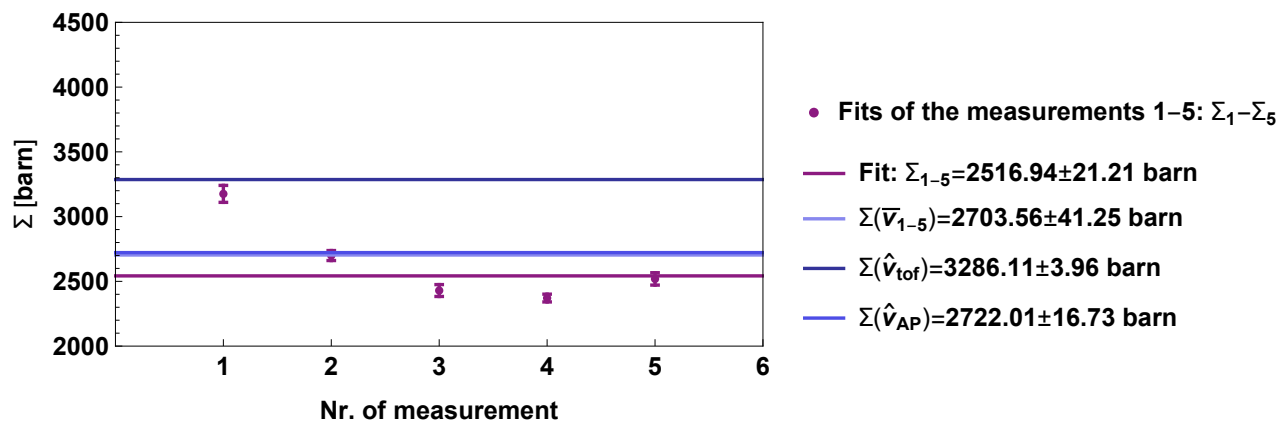


Figure 5.15: Comparison of the fit-results for the cross section of air for UCNs of the different measurements with the fit result of the aggregated measurements and the calculated cross sections.



Chapter 6

Conclusio

The measurement of the eigenenergies of gravitationally bound ultra cold neutrons (UCNs) can contribute to answer fundamental questions on gravity at short distances, various Dark Matter scenarios, Dark Energy, the Weak Equivalence Principle in the quantum regime etcetera.

The investigation of these quantum states with methods of resonance spectroscopy allows a very high measurement accuracy. The current *q*BOUNCE setup, which is a Ramsey-type spectrometer, is a promising approach.

In the frame of this thesis the *q*BOUNCE Ramsey setup, which is situated at the Institut Laue-Langevin (ILL) in Grenoble, was implemented and optimized. Thereby, the determination of the velocity spectrum of the UCNs in the *q*BOUNCE vacuum chamber was an important point. Although a Ramsey measurement is less sensitive to broad velocity spectra than a Rabi measurement, it is of great interest to understand the velocity distribution in order to further optimize the setup.

Three measurements were performed: a time-of-flight (TOF) measurement in the beamtube, an aperture measurement, and a measurement in which the dependence of the rate on pressure was determined and then the average velocity was calculated. The last two measurements took place inside the vacuum chamber. It is expected that the velocity spectrum in the vacuum chamber will differ a little bit from that in the beamtube. The average velocity resulting from the aperture spectrum is within the error of the calculated velocity from the rate-pressure dependence measurement: $\bar{v}_{AP} = (9.76 \pm 0.06) \text{ m s}^{-1}$ and $\bar{v}_{R(p)} = (9.83 \pm 0.15) \text{ m s}^{-1}$. The average velocity resulting from the TOF measurement is slightly lower : $\bar{v}_{\text{TOF}} = (8.09 \pm 0.01) \text{ m s}^{-1}$.

The accuracy of a Ramsey measurement is linear with the time the test particles spend in the spectrometer, i.e. inversely with the velocity. The TOF measurement shows that there is a lower average velocity within the beamtube than in the vacuum chamber. This suggests that either the geometry or the alignment of the beamtube or the beamtube endpiece scatter small velocity components out of the system.

One way to suppress this would be to optimize the height of the beamtube. It is very probable that the average velocity in the vacuum chamber could be matched to the average velocity in the beamtube. Until recently, the beamtube was made of glass. Its positioning was not ideal, due to a base plate that has been added to the platform for earthquake protection. Until now it was not possible to adjust the beamtube because the danger of breaking it was too high.

In the beamtime after the beamtimes spent at the ILL in the course of this thesis, the glass tubes were replaced with stainless steel tubes. It is promising that a corresponding optimization will succeed with these.

Appendices

Appendix A

Calculation steps

A.1

The substitutions $\tilde{z} = z - f(t)$ and $\tilde{t} = t$, with $\frac{d}{dz} = \frac{d\tilde{z}}{dz} \frac{d}{d\tilde{z}} + \frac{d\tilde{t}}{dz} \frac{d}{d\tilde{t}} = \frac{d}{d\tilde{z}}$ and $\frac{d}{dt} = \frac{d\tilde{z}}{dt} \frac{d}{d\tilde{z}} + \frac{d\tilde{t}}{dt} \frac{d}{d\tilde{t}} = -\dot{f}(t) \frac{d}{d\tilde{z}} + \frac{d}{d\tilde{t}}$ lead to

$$i\hbar \frac{d}{d\tilde{t}} \psi(\tilde{z}, \tilde{t}) = \left(-\frac{\hbar^2}{2m} \frac{d^2}{d\tilde{z}^2} + i\hbar \dot{f}(\tilde{t}) \frac{d}{d\tilde{z}} + mg\tilde{z} + mgf(\tilde{t}) + V_0\Theta(-\tilde{z}) \right) \psi(\tilde{z}, \tilde{t}) . \quad (\text{A.1})$$

Inserting equation 3.11 in equation A.1 gives

$$\sum_{n=0}^{\infty} \left(i\hbar \dot{C}_n(\tilde{t}) + C_n(\tilde{t}) E_n \right) e^{-i\frac{E_n \tilde{t}}{\hbar}} \psi_n(\tilde{z}) = \sum_{n=0}^{\infty} \left(-\frac{\hbar^2}{2m} \frac{d^2}{d\tilde{z}^2} + i\hbar \dot{f}(\tilde{t}) \frac{d}{d\tilde{z}} + mg\tilde{z} + mgf(\tilde{t}) + V_0\Theta(-\tilde{z}) \right) C_n(\tilde{t}) e^{-i\frac{E_n \tilde{t}}{\hbar}} \psi_n(\tilde{z}) . \quad (\text{A.2})$$

With equation 3.2 and the boundary condition $\psi(0) \approx 0$, A.2 is

$$i\hbar \sum_{n=0}^{\infty} \dot{C}_n(\tilde{t}) e^{-i\frac{E_n \tilde{t}}{\hbar}} \psi_n(\tilde{z}) = \sum_{n=0}^{\infty} \left(i\hbar \dot{f}(\tilde{t}) \frac{d}{d\tilde{z}} + mgf(\tilde{t}) \right) C_n(\tilde{t}) e^{-i\frac{E_n \tilde{t}}{\hbar}} \psi_n(\tilde{z}) . \quad (\text{A.3})$$

Multiplying A.2 by ψ_m^* and integrating over $\int_0^{\infty} d\tilde{z}$, with $\int_0^{\infty} \psi_m^* \psi_n d\tilde{z} = \delta_{mn}$, leads to

$$\dot{C}_m(\tilde{t}) = \dot{f}(\tilde{t}) \sum_{n=0}^{\infty} e^{i\frac{(E_m - E_n)\tilde{t}}{\hbar}} \underbrace{\int_0^{\infty} \psi_m^* \frac{d}{d\tilde{z}} \psi_n(\tilde{z}) d\tilde{z}}_{:=V_{mn}} C_n(\tilde{t}) - \frac{img}{\hbar} f(\tilde{t}) C_m(\tilde{t}) , \quad (\text{A.4})$$

with

$$V_{mn} = \int_0^\infty \psi_m \frac{d}{d\tilde{z}} \psi_n(\tilde{z}) d\tilde{z} = \underbrace{\psi_n \psi_m \Big|_0^\infty}_{=0} - \int_0^\infty \psi_n \frac{d}{d\tilde{z}} \psi_m(\tilde{z}) d\tilde{z} = -V_{nm}, \quad \psi^* = \psi \quad (\text{A.5})$$

being the interaction potential of state m and n . The values of the first few V_{mn} can be taken from table 3.2.

With the substitution $C(\tilde{t}) = u(\tilde{t})\tilde{C}(\tilde{t})$, the application of the chain rule $\dot{C}(\tilde{t}) = \dot{u}(\tilde{t})\tilde{C}(\tilde{t}) + u(\tilde{t})\dot{\tilde{C}}(\tilde{t})$ and $\frac{(E_m - E_n)}{\hbar} := \omega_{mn}$ equation A.4 is

$$\dot{\tilde{C}}_m(\tilde{t})u(\tilde{t}) = \dot{f}(\tilde{t}) \sum_{n=0}^\infty e^{i\omega_{mn}\tilde{t}} V_{mn} u(\tilde{t}) \tilde{C}_n(\tilde{t}) + \left(-\frac{img}{\hbar} f(\tilde{t})u(\tilde{t}) - \dot{u}(\tilde{t}) \right) \tilde{C}_m(\tilde{t}). \quad (\text{A.6})$$

The requirement $\dot{u}(\tilde{t}) \stackrel{!}{=} -\frac{img}{\hbar} f(\tilde{t})u(\tilde{t})$ with the solution $u(\tilde{t}) = T e^{-i\frac{amg}{\hbar} \int_0^{\tilde{t}} f(\tau) d\tau}$, with T being the time-ordering operator, gives 3.13.

A.2

A system of two linear differential equations $\dot{\vec{C}}' = \hat{O}'\vec{C}'$, with \hat{O}' being constant, can be solved with

$$\vec{C}' = A\vec{v}_1 e^{\lambda_1 t} + B\vec{v}_2 e^{\lambda_2 t}, \quad (\text{A.7})$$

where $\lambda_{1,2}$ and $\vec{v}_{1,2}$ are the corresponding eigenvalues and -vectors of the matrix operator \hat{O}' respectively and A and B are constant coefficients.

In equation (3.18) the matrix operator

$$\hat{O}(t) = \frac{1}{2} \begin{pmatrix} 0 & -a\omega V_{ji} e^{i((\omega - \omega_{ji})t + \phi)} \\ a\omega V_{ji} e^{-i((\omega - \omega_{ji})t + \phi)} & 0 \end{pmatrix} \quad (\text{A.8})$$

is time dependent. In order to solve the differential equation according to (A.7), (3.18) is transformed into the Schrödinger picture, where the operator is time independent and the state vector $\vec{C} = (C_i, C_j)^T$ evolves in time.

With

$$\vec{C} = U\vec{C}' \quad (U^\dagger U \stackrel{!}{=} \mathbb{1}) \quad \Rightarrow (3.18) \quad (\text{A.9})$$

$$-\dot{U}\vec{C}', \quad U^\dagger \left| \dot{U}\vec{C}' + U\dot{\vec{C}}' = \hat{O}U\vec{C}' \right. \quad (\text{A.10})$$

$$\underbrace{U^\dagger U}_{\mathbb{1}} \dot{\vec{C}}' = U^\dagger \hat{O}U\vec{C}' - U^\dagger \dot{U}\vec{C}' \quad (\text{A.11})$$

$$\dot{\vec{C}}' = \underbrace{(U^\dagger \hat{O}U - U^\dagger \dot{U})}_{\hat{O}'} \vec{C}' \quad (\text{A.12})$$

$$\Rightarrow U = \begin{pmatrix} e^{\frac{1}{2}i((\omega - \omega_{ji})t + \phi)} & 0 \\ 0 & e^{-\frac{1}{2}i((\omega - \omega_{ji})t + \phi)} \end{pmatrix} \quad (\text{A.13})$$

$$\Rightarrow \hat{O}' = \begin{pmatrix} -\frac{1}{2}i(\omega - \omega_{ji}) & -\frac{aV_{ji}\omega}{2} \\ \frac{aV_{ji}\omega}{2} & \frac{1}{2}i(\omega - \omega_{ji}) \end{pmatrix} \quad (\text{A.14})$$

equation (3.18) can be written as

$$\begin{pmatrix} \dot{C}'_i \\ \dot{C}'_j \end{pmatrix} = \begin{pmatrix} -\frac{1}{2}i(\omega - \omega_{ji}) & -\frac{aV_{ji}\omega}{2} \\ \frac{aV_{ji}\omega}{2} & \frac{1}{2}i(\omega - \omega_{ji}) \end{pmatrix} \begin{pmatrix} C'_i \\ C'_j \end{pmatrix}. \quad (\text{A.15})$$

The eigenvalues and -vectors of \hat{O}' are

$$\vec{v}_1 = \begin{pmatrix} \frac{i(\omega - \omega_{ji}) + \sqrt{-a^2 V_{ji}^2 \omega^2 - (\omega - \omega_{ji})^2}}{aV_{ji}\omega} \\ 1 \end{pmatrix}, \quad \lambda_1 = -\frac{1}{2}\sqrt{-a^2 V_{ji}^2 \omega^2 - (\omega - \omega_{ji})^2} \quad (\text{A.16})$$

and

$$\vec{v}_2 = \begin{pmatrix} \frac{-i(\omega - \omega_{ji}) + \sqrt{-a^2 V_{ji}^2 \omega^2 - (\omega - \omega_{ji})^2}}{aV_{ji}\omega} \\ 1 \end{pmatrix}, \quad \lambda_2 = \frac{1}{2}\sqrt{-a^2 V_{ji}^2 \omega^2 - (\omega - \omega_{ji})^2}. \quad (\text{A.17})$$

With the substitutions

$$aV_{ji}\omega = 2b, \quad (\text{A.18})$$

$$\sqrt{-4b^2 - (\omega - \omega_{ji})^2} = iR, \quad (\text{A.19})$$

$$\frac{2b}{R} = \sin(\theta), \quad (\text{A.20})$$

$$\frac{\omega - \omega_{ji}}{R} = \cos(\theta), \quad (\text{A.21})$$

and normalizing eigenvectors and corresponding eigenvalues are

$$\vec{v}_1 = \begin{pmatrix} i \cos \frac{\theta}{2} \\ \sin \frac{\theta}{2} \end{pmatrix}, \quad \lambda_1 = -\frac{iR}{2} \quad (\text{A.22})$$

and

$$\vec{v}_2 = \begin{pmatrix} -i \sin \frac{\theta}{2} \\ \cos \frac{\theta}{2} \end{pmatrix}, \quad \lambda_2 = \frac{iR}{2}, \quad (\text{A.23})$$

and hence, with (A.7)

$$\vec{C}' = A \begin{pmatrix} i \cos \frac{\theta}{2} \\ \sin \frac{\theta}{2} \end{pmatrix} e^{-\frac{iR}{2}t} + B \begin{pmatrix} -i \sin \frac{\theta}{2} \\ \cos \frac{\theta}{2} \end{pmatrix} e^{\frac{iR}{2}t}. \quad (\text{A.24})$$

The coefficients A and B can be determined with the boundary condition

$$\vec{C}'(t_0) = A \begin{pmatrix} i \cos \frac{\theta}{2} \\ \sin \frac{\theta}{2} \end{pmatrix} e^{-\frac{iR}{2}t_0} + B \begin{pmatrix} -i \sin \frac{\theta}{2} \\ \cos \frac{\theta}{2} \end{pmatrix} e^{\frac{iR}{2}t_0}, \quad (\text{A.25})$$

leading to

$$\vec{C}'(t + t_0) = \begin{pmatrix} \cos(\frac{1}{2}(t - t_0)R) - i \cos(\theta) \sin(\frac{1}{2}(t - t_0)R) & \sin(\frac{1}{2}(t - t_0)R) \sin(\theta) \\ -\sin(\frac{1}{2}(t - t_0)R) \sin(\theta) & \cos(\frac{1}{2}(t - t_0)R) + i \cos(\theta) \sin(\frac{1}{2}(t - t_0)R) \end{pmatrix} \vec{C}'(t_0). \quad (\text{A.26})$$

With equation (A.9) and (A.13), (A.26) leads to the final solution given in 3.19.

Appendix B

Fits

A least square fit was chosen to fit the data points. χ^2 ('chi squared') gives a measure of how close the fit function $f(x)$ is to the datapoints (x_i, y_i) with error σ_i . It is calculated with:

$$\chi^2 = \sum_{i=1}^N \frac{(y_i - f(x_i))^2}{\sigma_i^2} \quad (\text{B.1})$$

with N being the number of datapoints.

The goal of the least square fit is to minimize χ^2 [41].

The fit routine *NonlinearModelFit* from *Mathematica* was used. To perform a least square fit the options `Weights` $\rightarrow (1/\sigma^2)$ and `VarianceEstimatorFunction` $\rightarrow (1\&)$ are set.

The `Weights` option incorporates normally distributed variability based on the measurement errors into the fitting. Each data point is weighted by $1/\sigma^2$, where σ^2 is the measurement error for that data point.

The `VarianceEstimatorFunction`-option explicitly defines the variance scale estimator that is used. For measurement errors, the standard errors are computed only from the weights and so the variance estimate is set to 1 [53].

Additionally a third option is set: `ConfidenceLevel` $\rightarrow .68$ (the default value is .99). 0.68 is 'one sigma', i.e. once the standard deviation deviation. This means that if the measurement is repeated, in 68% of the cases, the same result is obtained.

B.1 Fit of the near-maximum TOF datapoints to a normaldistribution

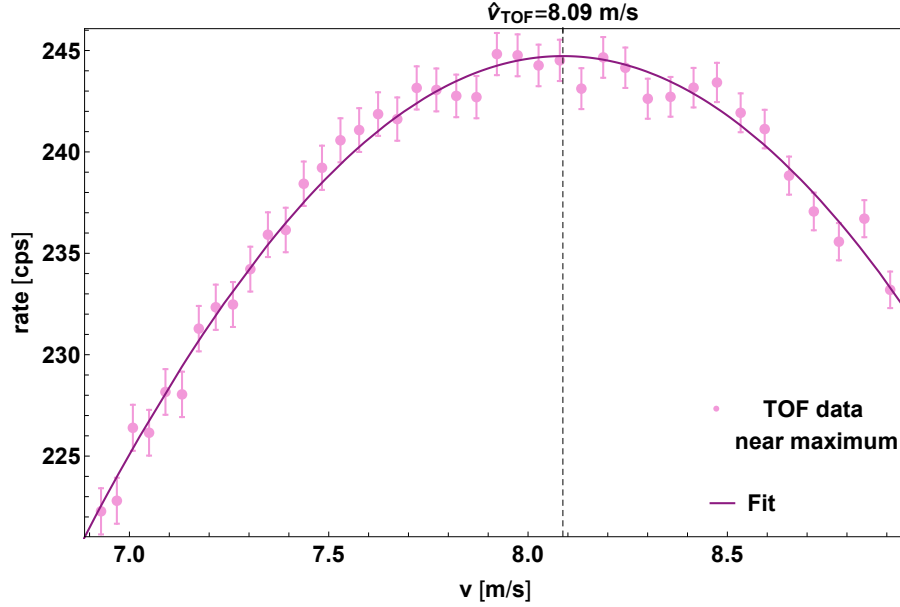
The recorded TOF-data $(t_{\text{TOF}}, R, \sigma_R)$ is, with $v = \frac{d}{t_{\text{TOF}}}$ and $d = 608$ mm, transformed to (v, R, σ_R) . The velocity value of the datapoint with the maximum rate is $v_{Rmax} = 7.92 \text{ m s}^{-1}$. The datapoints in the velocity intervall $[v_{Rmax} - 1, v_{Rmax} + 1]$ were fit to a normaldistribution

$$p(\hat{v}_{\text{TOF}}, \sigma) = \frac{n}{\sqrt{2\pi}\sigma} e^{-\left(\frac{v - \hat{v}_{\text{TOF}}}{2\sigma}\right)^2} \quad (\text{B.2})$$

Table B.1: Fit results for the aperture spectrum fit to a normal distribution

	<i>Estimate</i>	Standard Error	χ^2	N
\hat{v}_{TOF}	8.08	0.01	24.75	40
σ	2.66	0.04		
n	1630.66	24.79		

Figure B.1: TOF-datapoints near maximum and corresponding fit.



B.2 Fit of the aperture-spectrum to a normaldistribution

The normalized aperture data is fit to a normal distribution $p(\hat{v}_{AP}, \sigma)$. The three points of the dip were excluded first. They are caused by geometrical effects and not by the deformity of the velocity distribution.

Table B.2: Fit results for the aperture spectrum fit to a normal distribution

	<i>Estimate</i>	Standard Error	χ^2	N
\hat{v}_{AP}	9.76	0.06	42.84	10
σ	2.75	0.05		

B.3 Fit results $R(p)$

The data points (p, R, σ_R) are fit to a function $R(p) = R_0 e^{-ap}$

 Table B.3: Fit results $R(p)$

Fit	a	Standard Error a	R_0	Standard Error R_0	χ^2	N
R_1	0.00182301	9.21315×10^{-6}	1223.09	0.573408	1163.75	814
R_2	0.00147172	7.11512×10^{-6}	1218.25	2.48798	542.367	156

R_3	0.00217035	1.18619×10^{-5}	468.128	0.3074	1186.15	1149
R_4	0.00215173	9.75784×10^{-6}	466.67	1.35404	231.292	194
R_5	0.00427313	3.30165×10^{-5}	168.805	0.213276	927.781	857

B.4 Fit results \bar{v}

The data points $(p, \bar{v}, \sigma_p, \sigma_{\bar{v}})$ are fit to a function $\bar{v}(p) = \bar{v}$. $\sigma_{\bar{v}}$ is the propagated error given in equation 5.34.

The \bar{v} -entry of the datapoints is calculated with equation 5.33.

The $p/\ln(\frac{R}{R_0})$ -factor inflates the errors in the pressure range < 30 mbar extremely. R_0 results from a fit (see B.3).

In reality $R/R_0 \ll 1$ for $|p| \ll 1$. As the pressure decreases, the factor diverges, but the \bar{v} -expression remains constant because of $p \rightarrow 0$.

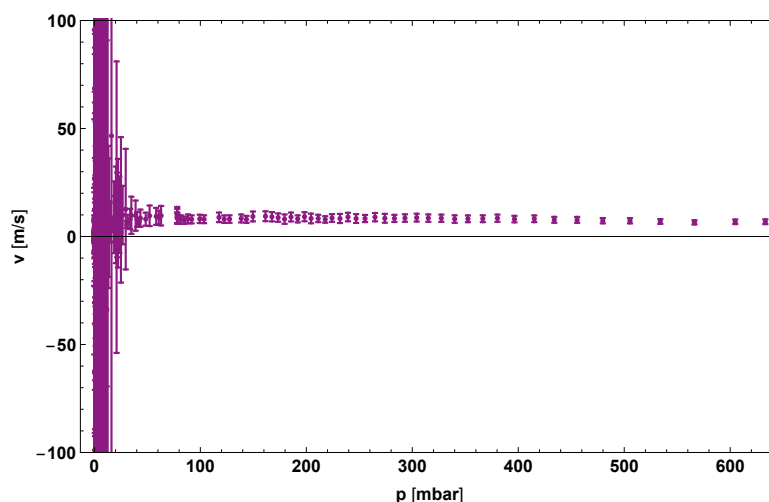
However, the measuring points are not ideal and therefore the \bar{v} -values sometimes explode for small p -values (see figure B.2). Therefore only data points with $R < 0.85R_0$ are used for the final evaluation.

For the evaluation of the final value of \bar{v} all datapoints of measurement 1-5 were aggregated and again fit to a function $\bar{v}(p) = \bar{v}$.

Table B.4: Fit results $\bar{v}(p)$

Fit	\bar{v}	Standard Error \bar{v}	χ^2	N
\bar{v}_1	7.84	0.41	3.07	45
\bar{v}_2	9.53	0.23	9.63	116
\bar{v}_3	10.62	0.63	1.47	66
\bar{v}_4	10.90	0.27	5.95	154
\bar{v}_5	10.01	0.56	2.95	76
\bar{v}_{1-5}	9.83	0.15	65.94	457

Figure B.2: Neutron mean velocity vs. pressure. The datapoints in the low-pressure range are excluded due to very big errors.



B.5 Fit results Σ

The data points $(p, \Sigma, \sigma_p, \sigma_\Sigma)$ are fit to a constant. The Σ -entry of the datapoints is calculated with equation 5.38. For the evaluation of the final value of Σ all datapoints of measurement 1-5 were aggregated and again fit to a constant.

Table B.5: Fit results Σ

Fit	Σ [barn]	Standard Error Σ	χ^2	N
Σ_1	3175.50	65.48	737.76	814
Σ_2	2699.36	38.50	43.02	156
Σ_3	2429.15	45.82	1016.35	1149
Σ_4	2371.06	30.06	58.47	194
Σ_5	2518.95	47.79	777.79	857
Σ_{1-5}	2542.27	18.48	495.14	3170

Appendix C

Further elaborations

C.1 Time offset

The five measurements consist of 7 measurement IDs in total. For the first two pumping measurements ($L=25.88$ cm and $L=40.85$ cm), a new measurement ID was started when the pressure was at 0.54 mbar and 8.04×10^{-4} mbar respectively.

Table C.1 shows the start- and stop-times of the measurements in both time-frames.

Table C.1: Start- and stop-time of the measurements in Neron- and NAS-time

ID	Measurement	Neron-start	Neron-end	NAS-start	NAS-stop
41	L=25.88 cm, Pumping	19:24:47	20:02:02	19:37:08	20:14:30
42	L=25.88 cm, Pumping	20:02:12	10:22:38	20:14:30	10:35:06
45	L=25.88 cm, Vent	11:17:39	11:33:06	11:28:36	12:25:16
47	L=40.85 cm, Pumping	12:17:30	14:13:42	12:29:45	14:26:12
48	L=40.85 cm, Pumping	14:13:50	14:28:41	14:26:12	14:41:11
66	L=40.85 cm, Vent	15:56:00	16:13:58	16:08:19	16:26:28
69	L=72.00 cm, Pumping	16:51:31	18:38:27	17:03:46	12:05:06

In the case of the stop of the first ID of the first measurement, the time of stopping the detector measurement and stopping the pressure measurement was exactly the same: the detector was not turned off, the measurement was stopped by pushing the 'next-subID'-button, i.e. there was no time offset between the detector- and the pressure-measurement stop.

This timestamp is used to determine the offset between 'Neron-time' and 'NAS-time':

$$\Delta t_{\text{NAS-Neron}} = 20:14:30 - 20:02:02 = 12:28 = 748 \text{ s.}$$

This constant time offset is added to the Neron-times, transforming the Neron-times into NAS-times. The comparison between the transformed, former Neron-start-times and the NAS-start times, gives the offset of the measurement start Δ_m (see table C.2).

Table C.2: Neron-time after addition of $\Delta t_{\text{NAS-Neron}}$ and offset of the measurement starts Δ_m

ID	Measurement	Neron-start + $\Delta t_{\text{NAS-Neron}}$	Neron-end + $\Delta t_{\text{NAS-Neron}}$	Δ_m [s]
41	L=25.88 cm, Pumping	19:37:15	20:14:30	-7
42	L=25.88 cm, Pumping	20:14:40	10:35:06	-10
45	L=25.88 cm, Vent	11:30:07	11:45:34	-91
47	L=40.85 cm, Pumping	12:29:58	14:26:11	-13
48	L=40.85 cm, Pumping	14:26:18	14:41:09	-6
66	L=40.85 cm, Vent	16:08:28	16:26:26	-9
69	L=72.00 cm, Pumping	17:03:59	18:50:55	-13
71	L=72.00 cm, Vent	18:54:24	19:00:33	-35

Δ_m is added to the timestamps of the rate measurements, leading to a list of rate-vs.-time points and a list of pressure-vs.-time points which are in the same time frame.

List of Figures

2.1	Scheme of the UCN source. A vertical guide tube conducts slow neutrons from the cold source to the turbine where the neutrons are decelerated to the UCN regime. The figure was taken from [31]	5
2.2	q BOUNCE setup	6
2.3	Beamtube endpiece	7
2.4	Sketch of a Ramsey-type setup. Section 1-5 with dimensions (width \times length) and neutron detector D. The state selectors above section 1 and 5 are indicated in dark. Section 2 and 4 are oscillated (indicated by the waves), in section 3, the longest section, the neutrons propagate freely.	8
3.1	Solutions of the Airy equation $\text{Ai}(x)$ and $\text{Bi}(x)$	11
3.2	First three eigenfunctions for neutrons in a gravitational potential.	12
3.3	Sketch of a state selector system and probability density of the first 5 wave functions: The higher the state, the higher the probability density for larger distances from the mirror. All neutrons that collide with one of the spikes of the roughened neutron mirror on top are scattered of the system. The longer the neutrons are in the state selector system (i.e. the longer the state selector system is) the more likely it is that the higher states are scattered out.	16
3.4	Rabi setup and typical Rabi curve	17
3.5	Rabi spectroscopy: state occupations $ C_0(\tau) ^2$ (solid) and $ C_3(\tau) ^2$ (dashed) after $\tau = 17.83$ ms vs. the oscillation frequency $\omega \in [\omega_{30} - 200, \omega_{30} + 200]$. The narrowness of the peak determines the accuracy of the results.	18
3.6	Width of a Rabi curve	19
3.7	Rabi curve for a velocity-normaldistribution ($\mu = 8.525$ m s $^{-1}$ and $\sigma = 6$ m s $^{-1}$) with $v \in]0, 20]$ m s $^{-1}$. A broad distribution was deliberately chosen in order to make the associated effects as visible as possible.	19
3.8	Ramsey setup and Ramsey fringes	21
3.9	Ramsey curve for a velocity distribution (normaldistribution with $\mu = 8.525$ m s $^{-1}$ and $\sigma = 6$ m s $^{-1}$, $v \in]0, 20]$ m s $^{-1}$). While the side maxima are widened to the point of unrecognizability, the main maximum remains sharp.	22
3.10	Rabi vs. Ramsey	23
3.11	Ramsey spectroscopy: state occupations $ C_0(2\tau + T) ^2$ and $ C_3(2\tau + T) ^2$ vs. the oscillation frequency	24
4.1	TOF setup: The chopper C interrupts the neutron beam. When the chopper window is open, neutrons get through and are, after a certain time t_{TOF} , detected in the detector D.	25

4.2	TOF spectrum: count rate during a TOF-measurement vs. the velocity. It's maximum represents the most probable velocity $\hat{v}_{\text{TOF}} = (8.09 \pm 0.01) \text{ m s}^{-1}$. \hat{v} was determined by fitting the data points near the maximum to a normal distribution (see appendix B.1).	26
4.3	Normalized TOF-spectrum compared to the fit-function.	26
4.4	First 300 central moments μ_n of the TOF spectrum.	27
4.5	Normalized aperture spectrum: measured distribution of neutron velocity in flight direction. The error bars indicate the statistical error of the measurement. The steps in light rose indicate the velocity interval of the respective measurement. An interval-width of $\Delta v = 1 \text{ m s}^{-1}$ was examined. With the exception of the area of the peak at $8.5 - 10 \text{ m s}^{-1}$. Here intervals of $\Delta v = 0.5 \text{ m s}^{-1}$ width and an additional interval $[9.75, 10.25]$ (the overlap of the integrals is dark) were investigated.	28
4.6	Comparison of the TOF- and aperture spectra. While the maximum of the TOF spectrum is as $\hat{v}_{\text{TOF}} = 8.09 \text{ m s}^{-1}$, the maximum of the aperture spectrum is shifted to $\hat{v}_{\text{AP}} = 9.76 \text{ m s}^{-1}$	29
4.7	Monitor rate vs. time. In the first few days of the cycle, the monitor detector was dismantled, i.e. no data could be recorded. It was reinstalled on June 17. The rate was constant at about ≈ 98 cps until a sudden drop to about ≈ 75 cps occurred on June 25. On July 20, another jump to ≈ 68 cps occurred. On August 1 the rate gradually dropped to ≈ 53 cps.	30
4.8	Reactor power over the course of the cycle 185/19-1. It was more or less constant at $\approx 51.8 \text{ MW}$ [43].	30
5.1	Measurement setup: The distance L between beamtube endpiece and detector was varied. The pressure inside the beamtube is approximately constant, with $p_{bt} \approx 10^{-5} \text{ mbar}$. The pressure in the vacuum chamber is varied (pumping and venting). The two vacua are separated by a thin AlMg foil mounted on the beamtube endpiece.	33
5.2	Hist-file: Number of counts during a measurement (dark) / background measurement (light) vs. channel number. The measurements were normalized to a measurement time of 1 s.	34
5.3	Neutron count rates for L_1 , L_2 and L_3 vs. time	36
5.4	Pumping and venting vs. time	37
5.5	Schematic sketch of the vacuum chamber, the valves and the placement of the vacuum sensors.	38
5.6	Comparison of the pressure records of the two vacuum sensors PCR280 and PBR260 and the their accuracies in different pressure ranges. This example was recorded while pumping vacuum. The fast drop at $t \approx 2200 \text{ s}$ is caused by the turbo pump switching on.	39
5.7	Interpolation and data points of a measurement row	40
5.8	Rate vs. pressure: mapped data points (p , R , σ_p , σ_r) and fits $R_1(p) - R_5(p)$. Pumping and venting for $L = (21.8 \pm 0.3) \text{ cm}$ (a), $L = (36.8 \pm 0.3) \text{ cm}$ (b) and $L = (67.9 \pm 0.3) \text{ cm}$ (c)	41
5.9	Illustration of the different neutron paths	43
5.10	Neutron mean velocity vs. pressure. The error bars in p -direction show σ_p , the error bars in Σ direction show σ_Σ	48
5.11	Neutron mean velocity vs. pressure. Data points from measurement 1-5 and fit.	50

5.12	Comparison of the fit-results for the neutron mean velocity of the different measurements.	50
5.13	Cross section of air for UCNs vs. pressure. The data points for low pressure $p < 30$ mbar are very unsteady. This is due to the values of R_0 resulting from a fit and not being exact. $\ln\left(\frac{R}{R_0}\right)$ is a factor in the expression for Σ . Therefore Σ can get very large in the case of $R_0 > R$	51
5.14	Cross section of air for UCNs vs. pressure. The data points from measurement 1-5 were aggregated and fitted. The fit is compared to the cross sections which calculate from equation 5.24 and $v = \hat{v}_{\text{TOF}}$, $v = \hat{v}_{AP}$ and $v = \bar{v}_{1-5}$	53
5.15	Comparison of the fit-results for the cross section of air for UCNs of the different measurements with the fit result of the aggregated measurements and the calculated cross sections.	53
B.1	TOF-datapoints near maximum and corresponding fit.	61
B.2	Neutron mean velocity vs. pressure. The datapoints in the low-pressure range are excluded due to very big errors.	62

List of Tables

1.1	Some examples of V_0 and the according UCN-velocity limit, taken from [18]. . . .	3
3.1	First few transition frequencies ν_{mn} [Hz]	12
3.2	First few interaction potentials V_{mn}	13
4.1	Fit results for the TOF spectrum fit to a Maxwell-Boltzmann-like distribution . .	26
4.2	First 10 central moments of the normalized TOF spectrum.	27
4.3	First 10 central moments of the normalized aperture spectrum.	28
5.1	Accuracies of the vacuum sensors PCR280 and PBR260 for different pressure ranges [48, 49]	39
B.1	Fit results for the aperture spectrum fit to a normal distribution	61
B.2	Fit results for the aperture spectrum fit to a normal distribution	61
B.3	Fit results $R(p)$	61
B.4	Fit results $\bar{v}(p)$	62
B.5	Fit results Σ	63
C.1	Start- and stop-time of the measurements in Neron- and NAS-time	64
C.2	Neron-time after addition of $\Delta t_{\text{NAS-Neron}}$ and offset of the measurement starts Δ_m	65

References

- [1] P. W. Higgs. “Broken Symmetries and the Masses of Gauge Bosons”. In: *Physical Review Letters* 13 (Oct. 1964), pp. 508–509.
- [2] E. G. Adelberger et al. “Searches for new Macroscopic Forces”. In: *Annu. Rev. Nucl. Part. Sci.* 41 (1991), pp. 269–320.
- [3] H. Abele, S. Baeßler, and A. Westphal. “Quantum states of neutrons in the gravitational field and limits for non-Newtonian interaction in the range between 1 micron and 10 microns”. In: *Lecture Notes in Physics* (Jan. 2003), pp. 355–366.
- [4] G. Cronenberg et al. “Acoustic Rabi oscillations between gravitational quantum states and impact on symmetron dark energy”. In: *Nature physics* 14 (2018), pp. 1022–1026.
- [5] J. Khoury and A. Weltman. “Chameleon Fields: Awaiting Surprises for Tests of Gravity in Space”. In: *Physical Review Letters* 93 (Oct. 2004), pp. 171104.1–171104.4.
- [6] T. Jenke et al. “Gravity Resonance Spectroscopy Constrains Dark Energy and Dark Matter Scenarios”. In: *Physical Review Letters* 112 (Apr. 2014), pp. 151105.1–151105.5.
- [7] M. Jaffe et al. “Testing sub-gravitational forces on atoms from a miniature in-vacuum source mass”. In: *Nature Physics* 13 (July 2017), pp. 938–942.
- [8] K. Hinterbichler and J. Khoury. “Screening Long-Range Forces through Local Symmetry Restoration”. In: *Nature Physics* 104 (June 2020), pp. 231301.1–231301.4.
- [9] F. Wilczek. “Axions and Family Symmetry Breaking”. In: *Physical Review Letters* 49 (Sept. 1982), pp. 1549–1552.
- [10] M. Thalhammer. “In progress”. PhD thesis. TU Wien, 2020.
- [11] A. N. Ivanov and M. Pitschmann. “Axions and Family Symmetry Breaking”. In: *Physical Review Letters* (June 2014), pp. 045040.1–045040.8.
- [12] A. N. Ivanov and M. Wellenzohn. “Nonrelativistic approximation of the Dirac equation for slow fermions in static metric spacetimes”. In: *Physical Review D* 90 (Sept. 2016), pp. 829–847.
- [13] *Fundamental Physical Constants — Extensive Listing*. URL: https://physics.nist.gov/cuu/pdf/all_2014.pdf.
- [14] J. Baumann et al. “Experimental limit for the charge of the free neutron”. In: *Physical Review D* 37 (1988), pp. 3107–3112.
- [15] M. Tanabashi et al. (Particle Data Group). In: *Phys. Rev. D* 98 ((2018) and 2019 update).
- [16] A. Serebrov et al. “Measurement of the neutron lifetime using a gravitational trap and a low-temperature Fomblin coating”. In: *Physics Letters B* 605 (Jan. 2005), pp. 72–78.
- [17] A. T. Yue et al. “Improved Determination of the Neutron Lifetime”. In: *Physical Review Letters* 111 (Nov. 2013).

- [18] R. Golub, D. J. Richardson, and S. K. Lamoreaux. *Ultra-Cold Neutrons*. Adam Hilger, 1991.
- [19] E. Fermi and W. H. Zinn. “Reflection of Neutrons on Mirrors”. In: *Physical Review* 70 (Apr. 1946).
- [20] Y. B. Zel’dovic. “Storage of cold neutrons”. In: *Journal of Experimental and Theoretical Physics* 36 (1959).
- [21] V. I. Lushchikov et al. “Observation of ultracold neutrons”. In: *ZhETF Pis. Red.* 9 (1969).
- [22] A. Steyerl. “Measurements of total cross sections for very slow neutrons with velocities from 100 m/sec to 5 m/sec”. In: *Physics Letters B* 29 (1969).
- [23] H. Rauch, W. Treimer, and U. Bonse. “Test of a single crystal neutron interferometer”. In: *Physics Letters A* 47.5 (1974), pp. 369–371.
- [24] R. Colella, A. W. Overhauser, and S. A. Werner. “Observation of Gravitationally Induced Quantum Interference”. In: *Phys. Rev. Lett* 34 (1975), pp. 72–78.
- [25] V. I. Lushchikov and A. Frank. “Quantum effects occurring when ultracold neutrons are stored on a plane”. In: *JETP Lett.* 28 (1978), pp. 559–561.
- [26] V.V. Nesvizhevsky et al. “Quantum states of neutrons in the Earth’s gravitational field”. In: *Nature* 415 (Feb. 2002), pp. 297–9. DOI: 10.1038/415297a.
- [27] T. Jenke et al. “Q-BOUNCE—Experiments with quantum bouncing ultracold neutrons”. In: *Nuclear Instruments and Methods in Physics Research A* 8 (2009), pp. 318–321.
- [28] T. Rechberger. “Ramsey Spectroscopy of Gravitationally Bound Quantum States of Ultracold Neutrons”. PhD thesis. TU Wien, Oct. 2018.
- [29] J. Micko. *qBounce - Gravity Resonance and Ramsey Spectroscopy*. Master thesis. TU Wien, May 2018.
- [30] M. Thalhammer. “Optimierung der Detektorsignalverarbeitung des Gravitationsexperiments qBounce”. Master thesis. TU Wien, 2013.
- [31] A. Steyerl et al. “A new source of cold and ultracold neutrons”. In: *Physics Letters A* 116 (1986), pp. 347–352.
- [32] T. Bittner. “Entwicklung eines Blendensystems zur Geschwindigkeitsselektion für das qBounce Experiment”. Master thesis. TU Wien, 2013.
- [33] H. Abele et al. “Ramsey’s method of separated oscillating fields and its application to gravitationally induced quantum phase shifts”. In: *Physical Review D* 81 (2010), pp. 065019–1–065019–8.
- [34] M. Pitschmann. “Remarks on qBOUNCE”. In: . (2018).
- [35] G. Pignol et al. “GRANIT project: a trap for gravitational quantum states of UCN”. In: (Sept. 2007).
- [36] T. Jenke. “qBounce - vom Quantum Bouncer zur Gravitationsresonanzspektroskopie”. PhD thesis. TU Wien, Sept. 2011.
- [37] I. I. Rabi, S. Millman, and P. Kusch. “The molecular beam resonance method for measuring nuclear magnetic moments”. In: *Physical Review* 55 (1939), pp. 526–535.
- [38] R.P. Feynman et al. *The Feynman Lectures on Physics; Vol. II*. AAPT, 1965.
- [39] J. Micko, J. Bosina, and T. Jenke. “Considerations for the migrations from Rabi- to Ramsey-spectroscopy of the qBOUNCE-experiment”. In: . (2019).

- [40] N. F. Ramsey. “A molecular beam resonance method with separated oscillating fields”. In: *Physical Review* 78 (1950), pp. 695–699.
- [41] R. Kissell and J. Poserina. *Optimal Sports Math, Statistics, and Fantasy*. Academic Press, 2017.
- [42] B. Zeka. *In progress*. Bachelor thesis. TU Wien, 2020.
- [43] *ILL data portal*. URL: <https://data.ill.fr/reactor/>.
- [44] A.-J. Dianoux and G. Lander. *Neutron Data Booklet second edition*. OPC Science, 2003.
- [45] A. Balthasar. *Minimierung des Untergrundes eines Neutronendetektors*. Bachelor Thesis. TU Wien, Sept. 2017.
- [46] N. Huber. *Extending the Software Environment of the qBounce Platform*. Bachelor thesis. TU Wien, June 2017.
- [47] H.-G. Stangl. *Characterisation of the vacuum system of the qBounce experiment*. Bachelor thesis. TU Wien, 2015.
- [48] *PCR 280 Compact Pirani Capacitance Gauge Operating Instructions*. URL: https://www.idealvac.com/files/brochures/Pfeiffer_PCR_280.pdf.
- [49] *Short Instructions Incl. Declaration of Conformity Compact FullRange™ BA Gauge PBR 260*. URL: https://www.idealvac.com/files/ManualsII/Pfeiffer_PBR260_Operating_Instructions.pdf.
- [50] F. Atchison et al. “Measured Total Cross Sections of Slow Neutrons Scattered by Gaseous and Liquid $^2\text{H}_2$ ”. In: *Physical Review Letters* 94 (2005).
- [51] C.W. Allen. *Astrophysical Quantities 3rd.ed.* The Athlone Press, 1973.
- [52] O. A. Alduchov and R. E. Eskridge. “Improved Magnus Form Approximation of Saturation Vapor pressure”. In: *Journal of applied meteorology* 35 (1995), pp. 601–609.
- [53] *How to Fit Models with Measurement Errors*. URL: <https://reference.wolfram.com/language/howto/FitModelsWithMeasurementErrors.html>.

Acknowledgements

To conclude, I would like to thank some people without whom this thesis would not have been possible in this form.

I would like to thank Prof. Hartmut Abele for my supervision as a diploma student and for the opportunity to participate in such an exciting and unique experiment.

My special thanks go to Dr. Tobias Jenke. For making my employment as a Stagiaire at the ILL for the duration of my stay in Grenoble possible. For being my supervisor and for many discussions, advice and suggestions that have contributed greatly to the success of this thesis. Also for the great support during the writing of this thesis and the quick corrections despite stressful times.

A very big thank you goes to Jakob Micko. As my responsible PhD we worked together on the experiment (nearly) every day during my stay in Grenoble. I learned a lot, both in terms of experimental work and theoretical knowledge. Despite sometimes very stressful days and many working hours, I always had fun at work and enjoyed being at the ILL.

I would also like to thank Dr. René Sedmik who, as *qBOUNCE* Postdoc, was always there to support me with words and deeds.

My thanks also go to Dr. Stephanie Roccia and Thomas Brenner for my warm welcome to the 'PF2-Team' and their support.

I would also like to thank my fellow students Blerta, Richard and Niko, who also spent some time at the ILL. For many interesting discussions, for the teamwork and for a fun time.

Last but not least, I would like to thank my family and friends for their support during my entire studies.